博 士 学 位 論 文

氏 名（本 籍）	張　　強
学 位 の 種 類	博　士　(工学)
学 位 記 番 号	博 甲 第 179 号
学位授与年月日	令和 5 年 3 月 31 日
学位授与の要件	学位規則第 4 条第 1 項
学 位 論 文 題 目	Jet flow control using Coanda effect on a circular cylinder
論文審査委員	主査　佐藤　光太郎　教授
	副査　伊藤　慎一郎　教授
	〃　　橋本　成広　　教授
	〃　　鈴木　健司　　教授
	〃　　横田　和彦　　教授

工学院大学大学院

Abstract

In this paper, two methods without altering the geometry are proposed to achieve the control of the jet direction. The first method involves using a secondary flow with a Coanda surface to control a primary jet with high momentum . The study investigates the influence of fluid parameters, including dimensionless frequency f^*, the momentum ratio of primary jet to secondary flow ξ and the ratio of steady flow velocity to velocity oscillation amplitude ζ on the deflection characteristics and unsteady characteristics of the primary jet. The effect of the ratio of the primary slot width to the Coanda cylinder radius h_1/R as a shape parameter on the deflection characteristics and the jet structure is also been investigated. The results demonstrate that introducing the parameter ζ increases the number of control strategy combinations and the deflection characteristics depend on both fluid parameters and the ratio of the primary slot width to the Coanda cylinder radius h_1/R.

The second method presented in this paper is based on the circulating control wing theory. A tangential blowing cylinder is used as a simple circulating control wing system to control the direction of an existing jet in the environment. The study investigates the effects of the momentum coefficient C_μ between the primary jet and the jet sheet from the cylinder slot, the slot angle θ_j, the jet width W and the eccentricity rate ε on the jet deflection angle. The results show that adjusting the momentum coefficient C_μ with a suitable slot angle θ_j and eccentricity rate ε enables a wider range of angular control.

Contents

Abstract 2

List of Figures 5

Introduction 8

1.1 Background 9

1.1.1 Fluidic Thrust Vectoring Method 9

1.1.2 Circulation Control Wing 11

1.2 Research Objectives and Composition 12

Influence of Amplitude of Excited Secondary Flow on the Direction of Jets 16

2.1 Introduction 17

2.2 Nomenclature 18

2.3 Experimental setup and method 20

2.3.1 Experimental equipment 20

2.3.2 Velocity measurement method 23

2.3.3 Experimental evaluation 25

2.4 Results and Discussion 30

2.4.1 Influence of ζ, ξ and f^* on jet flow characteristics 32

2.4.2 Unsteady flow characteristics analysis 44

2.5 Summary 53

Jet Flow Characteristics for Various Slot Widths and Frequency using Coanda Secondary Flows 54

3.1 Introduction 55

3.2 Nomenclature 56

3.3 Experimental setup and method 58

3.4 Results and Discussion 62

3.4.1 Influence of various R/h_1 on jet flow characteristic 62

3.4.2 Effect of various f on jet flow unsteady characteristic 74

3.5 Summary 83

Jet Direction Control Using Circular Cylinder with Tangential Blowing 84
4.1 Introduction 85
4.2 Nomenclature 86
4.3 Experimental setup and method 88
4.3.1 Experimental equipment 88
4.3.2 Velocity measurement method 92
4.3.3 Experimental evaluation 93
4.4 Results and Discussion 97
4.4.1 Influence of momentum coefficient 97
4.4.2 Influence of injection angle 106
4.4.3 Jet widths and eccentricity of cylinder 113
4.5 Summary 120
Comparison between two jet direction control methods 121
Conclusion 125
Acknowledgement 130
Reference 131

List of Figures

2-1 Schematic of the test section used in the experiments.....22

2-2 Schematic of slot and Coanda surface.....22

2-3 Measurement method of linear velocity distribution.....24

2-4 Numerical simulation domain and boundary condition.....29

2-5 Magnified view of the typical grid near the slots.....29

2-6 Symmetry confirmation results.....31

2-7 Phase averaged wave forms for typical secondary flow under the ratio of momentum ξ = 0.08. The number of repetitions of data collection is 50.....33

2-8 Flow visualization for various ratios between the velocity of continuous flow and the amplitude of velocity oscillation ζ.....36

2-9 velocity distribution for various ratios between the velocity of continuous flow and the amplitude of velocity oscillation ζ.....37

2-10 Dimensionless time-averaged velocity distribution for f^*=0.05. 41

2-11 Relation between various ratios between the velocity of continuous flow and the amplitude of velocity oscillation ζ and deflection angle θ_c under different dimensionless frequencies f^*.....42

2-12 Deflection angle comparison for various ratios between the velocity of continuous flow and the amplitude of velocity oscillation ζ = -∞, ζ = -1, ζ = 0 for different ratios of momentum, ξ, and different dimensionless frequencies f^*.....42

2-13 Relation between dimensionless ratio of maximum velocity U_{max} to jet half width $b_{1/2}$ with a similar deflection angle of $\theta_c \approx 30^\circ$ while the ξ=0.08.....43

2-14 Flow visualization of the ratio between the velocity of continuous flow and the amplitude of velocity oscillation ζ =-∞.....47

2-15 Flow visualization of the ratio between the velocity of continuous flow and the amplitude of velocity oscillation ζ = -1.....48

2-16 Flow visualization of the ratio between the velocity of continuous flow and the amplitude of velocity oscillation ζ= 0.....49

2-17 CFD result with the dimensionless frequency f^* set at 0.05.....50

2-18 Velocity distribution and RMS^* for the ratios between the velocity of continuous flow and the amplitude of velocity oscillation ζ= -∞, -1, and 0.....51

2-19 RMS^*_{max} under various ratios between the velocity of continuous flow and the amplitude of velocity oscillation ζ and dimensionless frequencies f^*.....52

3-1 Experiment apparatus.....60

3-2 Schematic of slots and velocity distribution measurement method.....61

3-3 Time-average Flow visualization for different R/h_1 with f^* =0.04, ξ = 0.06.....63

3-4 Flow patterns of jets under condition of secondary synthetic jet with ξ=0.06.....67

3-5 Relation between the Ratio of momentum ξ between primary flow and secondary flow and deflection angle θ_c for various frequency and slot width ratio.....69

3-6 Relation between the slot width ratio R/h_1 and deflection angle θ_c for various ratio of momentum ξ.....71

3-7 Comparison of Spectrum of fluctuations for different R/h_1 when x_c/h_1 = 6, ξ = 0.06 and f^*=0.04.....73

3-8 Visualized observations and spectrum of fluctuations for suction flow as a secondary flow under the conditions of ξ = 0.06 and R/h_1 = 3.....76

3-9 Time-step visualized observations for synthetic jet as secondary flow under the conditions of R/h_1 = 3, f^* = 0.0029, f = 10Hz and ξ = 0.06.....77

3-10 Time-step visualized observations for synthetic jet as secondary flow under the conditions of R/h_1 = 3, f^*=0.029, f = 100Hz and ξ = 0.06.....78

3-11 Comparison of Spectrum of fluctuations for different f^* when x_c/h_1 = 6, ξ = 0.06 and R/h_1 = 3.....79

3-12 Velocity distribution for continuous flow and synthetic jet under R/h_1 of 3 and ξ of 0.06.....81

3-13 Dimensionless half width comparison for different frequency under R/h_1 = 3, ξ = 0.06.....82

4-1 Experimental apparatus.....90

4-2 Schematic of test section for experiments.....90

4-3 Schematic of circular cylinder with tangential blowing.....91

4-4 Diagram to calculate velocity distribution centroid.....96

4-5 Flow visualization obtained using smoke-wire method for $\theta_j = 90^\circ$.....101

4-6 Surface pressure around circular cylinder for $\theta_j = 90^\circ$.....102

4-7 Angle of separation point around circular cylinder for $\theta_j = 90^\circ$.....102

4-8 Relation between momentum coefficient and lift coefficient and drag coefficient for $\theta_j = 90^\circ$.....103

4-9 Dimensionless velocity distribution of circular cylinder for $\theta_j = 90^\circ$.....104

4-10 Spectrum of fluctuations in wake of circular cylinder for $\theta_j = 90^\circ$.....105

4-11 Flow visualization obtained using smoke-wire method for $C_\mu = 0.187$.....109

4-12 Dimensionless velocity distribution of circular cylinder for $\theta_j = 0^\circ, 180^\circ, 270^\circ$.....110

4-13 Relation between momentum coefficient and lift coefficient for slot angles of 0°, 90°, 180°, and 270°.....111

4-14 Relation between momentum coefficient and deflection angle of jets for slot angles of 70°, 90°, 110°, and 130°.....111

4-15 Surface pressure around circular cylinder for $\theta_j = 130^\circ$.....112

4-16 Dimensionless velocity distribution of circular cylinder for $W/D = 2$ and 3.....114

4-17 Relation between momentum coefficient and deflection angle for various dimensionless primary jet widths.....115

4-18 Dimensionless velocity distribution and pressure distribution of circular cylinder for $\varepsilon = 0, \pm 1.3$ and $C_\mu = 0.364$.....117

4-19 Flow visualization obtained using smoke-wire method for $C_\mu = 0.364$.....118

4-20 Relation between eccentricity rate ε and lift coefficient C_L for $C_\mu = 0.364$, $D/W = 0.25$.....119

4-21 Relation between eccentricity rate ε and deflection angle θ_c.....119

5-1 Comparison of deflection angle between two methods for different ζ.....123

5-2 Comparison of deflection angle between two methods under different R/h_1 (R/W).....124

-Chapter 1-

Introduction

1.1 Background

1.1.1 Fluidic Thrust Vectoring Method

The jet is a fluid stream projected into a surrounding medium from a nozzle, aperture or slot. It possessed higher momentum than the surrounding fluid, and the viscosity between the layers of gas enables the jet to entrain the surrounding fluid. Asymmetrical structure or small variations in flow near the exhaust nozzle can result in a large response of the primary jet. For instance, the Coanda effect refers to the phenomenon of the jet being dragged to the arc surface near the exhaust nozzle. One of the most typical applications of jet flow is in jet engine. Although in past 80 years, jet engines for aircraft have been made a good process in performance, it is still need improvement in fuel consumption and noise reduction.[1] Therefore, details concerning jet structure and basic flow characteristics are actively being investigated. For instance, to reduce the magnitude of pressure fluctuation and promote jet mixing[2] for noise reduction, Chevron nozzles with 'saw-tooth' patterns have been developed, and this type of engine nacelles is gaining in popularity. Therefore, It can thus be concluded that the development of jet research is closely linked to the advances in fluid mechanics. Additionally, various aspects of daily life, such as air conditioning, air curtains, drag reduction in cars, rail vehicles, ships, aircraft, and suppression of unsteady flow in fluid machinery, benefit from jet research.

Due to the unique characteristics of jets, research on jet direction control has received considerable attention. However, until now, most fluid machines still use mechanical methods for directional control, such as employing movable or variable parts like a variable jet nozzle or adding louvers at the exhaust nozzle to adjust the jet angle. However, mechanical methods have a limited range of adjustable angles for the jet and a high probability of problems between moving parts. In particular, for large fluid machines used in harsh environments, faults between moving parts can lead to serious accidents. On the other hand, fluidic thrust vectoring technology aims to control the main stream by installing a jet device around the nozzle while maintaining a fixed nozzle geometry. Compared to mechanical methods, fluidic thrust vectoring can not only improve deflection ability and reliability, but also potentially

downsize and lighten airfoils and other components, reduce the occurrence of mechanical failure, and improve fuel efficiency via drag reduction .[3-5] By changing the shape of the nozzle and using different types of secondary jet devices, many thrust vector control methods have been developed. For example, the Shock Vectoring Control(SVC) [6-8] proposes a convergent-divergent nozzle to use the principle that the direction of the fluid will be deflected after flowing though the convergent section of the nozzle to achieve pitch thrust vectoring by injecting the secondary flow. Additionally, there are Coanda high-efficiency nozzles[9] and nozzles using throat shifting methods[10], which also aim to improve vectoring capability and efficiency. In addition, many studies have explored the use of continuous flow including counter flow and co-flow, to control the flow field[11-16]. Mason et al.[11] studied the directional control of a primary jet using co-flow method. They installed two components with Coanda surfaces on either side of the primary nozzle to create a channel for co-directional flow. And jet deflection was achieved by using the secondary flow parallel to the direction of the primary flow, in conjunction with the Coanda effect. Their experimental and numerical results reported that the deflection characteristics of the jet are influenced by several factors, including the velocity of secondary flow, the diameter of Coanda surface, and the ratio of the primary and secondary nozzle heights. Dores et al.[14] investigated the use of counter flow as the secondary flow for thrust vector control, and studied the impact of the ratio of primary and secondary momentum and the gap between the primary slot and Coanda Collar on the vector efficiency. The results show that a vector angle of 25° could be easily achieved with a momentum ratio of only 6% and a proper gap distance. Moreover, the synthetic jet technique has been proposed in recent years to achieve stall or fluid separation control. The technology works by alternately repeating the suction process and the injection process by a synthetic jet in a slot or nozzle to create a jet similar to a continuous jet downstream of the slot or nozzle while maintaining a net flow of zero. This phenomenon is characterized by the vortex pairs created near the slit angle inducing velocity on each other during the injection process and thus initiating a transnational movement. For instance, Smith and Glezer [17] utilized synthetic jets in 1998 to control the direction of jets from a nozzle having 25 times diameter larger than that of the synthetic jets. There are also many

studies[18-25] investigating the flow characteristics of synthetic jets, including the differences of the flow characteristics between continuous jets and synthetic jets[19], the effect of Reynolds number[22] and the effect of the input waveform[23], etc. Kobayashi et al.[24] proposed a jet vectoring method that applies a synthetic jet as the secondary flow. This method involves two dimensionless parameters that do not require any changes to the geometrical shape for jet direction control: the momentum ratio of the jet and the dimensionless frequency. The research results indicate that the combination of the momentum ratio and the dimensionless frequency can produce a controllable deflection angle for the jet. In conclusion, synthetic jets show promise due to their ability to deflect and unique action mode without changing geometry. However, there are still challenges in implementing them in various engineering practices since current research on jet deflection using synthetic jets is limited to small velocity scales and low Reynolds number scenarios. Therefore, there is a significant challenge in achieving control of high-speed wake flow in larger scale engines.

1.1.2 Circulation Control Wing

The circulation control wing(CCW) is a high lift system that employs a similar principle to some thrust vectoring methods. The simplest CCW system, which uses a circular cylinder with tangential blowing, involves placing a cylinder with an injection slot in the flow field. The jet from the injection slot flows over a large area on the curved surface, due to the Coanda effect, entraining the surrounding flow field and ultimately generating a high lift force. Because of the high-lift characteristics of this system, many researchers have focused their research on short take-offs, low fuel consumption and noise reduction[26-27]. For instance, researchers have investigated and applied the tangential blowing cylinder to no-tail-rotor helicopters[28-30], replacing the tail rotor with a tangential blowing cylinder. This structure reduces noise by eliminating the interference between the tail rotor and the main rotor. Additionally, the tangential blowing jet sheet from the cylinder slot can inhibit the separation of the boundary layer and, thus, control the flow deflection, making the circular cylinder with tangential blowing one of the boundary layer control methods. Therefore, many studies have

focus on flow field control, such as adjusting the flow direction through separation position control[31], controlling the wake flow around cylinders, and investigating the unsteady characteristics of wake flow[32-34]. The variable flow direction with a fixed geometrical shape enables the cylinder to be applied to turbomachinery stators, reduce vehicle resistance, and suppress Karman vortex shedding in blunt bodies. However, few studies have applied CCW to thrust vector control. Although the CCW system has a simple construction and is able to deflect the primary jet simply by adjusting the momentum of the jet sheet from the slot, the effects of parameters of the Circulation Control Wing on the flow characteristics still need further investigation. For instance, the relative angle between slot and primary jet or the cylinder radius. Choosing the appropriate parameter conditions may enable an extension of the range of deflection angles or an improvement in the flow pattern.

1.2 Research Objectives and Composition

This research focus on controlling the direction of a jet without using moving parts, meaning there is no change in the geometry of slot. The goal is to study the relationship between physical parameters and jet deflection characteristics.In this study, two major jet direction control methods are proposed. The first method is mainly discussed in Chapter 2 and 3. It attempts to control the direction of a steady primary jet with high momentum by using a secondary flow next to a Coanda surface. This method is suitable for determining the jet direction at the slot outlet, where the jet is generated and has the potential to be applied in adjusting the fluid force of aircraft or adjusting the jet angle of air conditioner blowing ports. The second method, which is discussed in Chapter 4, uses a cylinder with tangential blow(CCW) to attempt to control the direction of an existing jet by adjusting the momentum of jet sheet from the cylinder slot. For example, this method is expected to be applied to ventilation of mist and smoke generated in enclosed spaces of factories, ductless ventilation, air-conditioning, and other applications.

This thesis are consisted of 6 chapters:

Chapter 1 serves as the introduction, explaining the meaning of controlling the direction of the jet without changing the geometry, as well as the latest trends in research on fluidic thrust vectoring and Circulation Control Wing. This chapter also presents unresolved issues in related fields and the purpose of this research.

Chapters 2 and 3 discuss the method of adjusting the direction of the continuous primary jet using a secondary flow next to the Coanda surface. This method is called fluidic thrust vectoring and was originally proposed in aeronautical engineering to control the thrust direction by adjusting the injection angle of combustion gas from aircraft engines. Compared with conventional mechanical thrust vectoring, fluidic thrust vectoring can not only extend the range of deflection angle and improve reliability by eliminating moving parts, but also reduce the size and weight of the airfoil and the associated drag force. In other words, the practical application of this technology is expected to improve aircraft attitude control, kinematic performance, and fuel efficiency. To date, although there are notable results in studies of fluidic thrust vectoring, the secondary flow near the Coanda surface still is mostly steady jet or steady suction. Furthermore, the only parameter for adjusting the jet deflection angle without moving parts is the momentum ratio between the primary jet and secondary flow, which makes it extremely difficult to smoothly change the jet deflection angle when jet hysteresis phenomena appears. Recently, a jet vectoring method using a secondary synthetic jet was proposed. It successful achieves smooth jet direction control by combining two dimensionless parameters: the momentum ratio ξ between primary jet and secondary flow ξ and the dimensionless oscillation frequency of the synthetic jet f^*. However, many unknown factors still remain regarding the suitable conditions, generation mechanism, and jet quality, including the unsteady characteristics.

Chapter 2 propose a new method to achieve direction control of the primary continuous jet using a secondary excited flow next to Coanda surface. Unlike Synthetic jets, which have a net flow of zero, excited flows generate a net flow that is decomposed into steady and

unsteady components. In other word, in addition to the momentum ratio ξ and the dimensionless frequency f^*, the concept of the ratio ζ between the steady-state velocity component and the velocity fluctuation amplitude is generated in the secondary excited flow. This chapter aims to experimentally investigate the effects of ζ and ξ on the deflection characteristics of the primary jet, as well as the quality of the jet, including unsteady characteristics and jet half width. The results of Chapter 2 demonstrate that the deflection angle of the jet depends not only on the momentum ratio ξ and the dimensionless frequency f^*, but also on the ratio ζ between the steady-state velocity component and the velocity fluctuation amplitude component of the secondary excited flow.

Chapter 3 use the steady flow and the synthetic jet as secondary flow, and discusses the effect of the primary slot width h_1 and the frequency of the synthetic jet f on the jet flow characteristics. The main parameters in this chapter are the ratio between the radius of the Coanda surface and the primary jet slot width R/h_1 and the dimensionless frequency f^*, and the results are presented for a constant radius R of the Coanda surface and varying primary slot width h_1.The mainly result shows that the ratio R/h_1 have effect on the deflection ability of both secondary steady flow and secondary synthetic jet.

Chapter 4 propose a method to control the two-dimensional jet direction by placing a tangential blowing cylinder downstream of the primary jet. In this chapter, the time-average pressure distribution on the cylinder surface and the time-average velocity distribution are measured to study the effect of momentum coefficient C_μ , slot angle θ_j, eccentricity rate ε and jet width W on the deflection characteristics and unsteady characteristics of primary jet. The main result shows that the smooth deflection angle control can be achieved by adjusting C_μ with a suitable slot angle θ_j.

Chapter 5 presents a comparison between the two methods discussed in the previous chapters. The study discover that the direction control method of the primary continuous jet using the Coanda surface-induced secondary flow allows for a significant jet deflection angle

at a low momentum ratio. However, the controllable range solely based on the momentum ratio is limited due to the occurrence of discontinuous angle changes. Conversely, the direction control method of the jet using a tangential blowing cylinder exhibits smooth increases in jet deflection with the momentum ratio, making it more easily controllable. Nonetheless, it was demonstrated that a high momentum ratio is necessary to achieve a considerable deflection angle of the jet using this method.

Chapter 6 summarizes the main results and conclusions from the previous chapters.

-Chapter 2-

Influence of Amplitude of Excited Secondary Flow on the Direction of Jets

2.1 Introduction

In the field of thrust vectoring, jet direction control techniques often rely on the use of continuous flow or synthetic jets as control fluids. While the use of continuous flow as a secondary flow can achieve control of jet deflection angle by adjusting the momentum ratio of primary to secondary flow, it is prone to a wider 'dead zone' and requires a very high momentum ratio to achieve a high deflection angle. Synthetic jets, on the other hand, present a challenge of increasing flow rate and momentum since their static flow rate is 0. Although the deflection angle can be adjusted by changing the dimensionless frequency, significant differences in flow patterns between large and small dimensionless frequency conditions can limit practical applications. This chapter proposes a new thrust vector jet theory that involves using excited flow with velocity fluctuations as a secondary control flow near the Coanda surface. Unlike synthetic jets, the time-averaged flow rate of excited flow is not always zero, and vibration characteristics exist even when the momentum ratio of the primary to secondary jets is constant. Therefore, a new control parameter, the ratio of the steady-state velocity component of the secondary flow to the amplitude of the velocity fluctuations of the secondary flow ζ was added in addition to the momentum ratio ξ and the dimensionless frequency f^* in the experiments of this chapter to study the influence of different combinations of parameters on flow deflection characteristics. Furthermore, this chapter discusses the flow pattern of the deflected primary flow and the unsteady characteristics. The main results show that introducing a new parameter ζ increasing the number of combinations of setting conditions for realizing a controllable jet deflection angle. By combining the three parameters ξ, f^*, and ζ, this method achieves obtain good directional ability while controlling the jet half width and unsteady characteristics.

2.2 Nomenclature

f : Frequency of synthetic jet [Hz]

f^* : Dimensionless frequency [-]

h_1 : Primary slot width (1.0×10^{-2}) [m]

h_2 : Secondary slot width (2.0×10^{-3}) [m]

l : Thickness of partition plate (1.0×10^{-3}) [m]

P_a : Atmospheric pressure [Pa]

R : Radius of Coanda surface (1.5×10^{-2}) [m]

Re : Reynolds number [$= \frac{2U_2R}{\nu}$]

r_m : Measurement point radius (1.0×10^{-1}) [m]

RMS^* : Dimensionless root mean square [$= \sqrt{\frac{1}{n}\sum_{i=1}^{n}\left(\frac{v_i-\bar{v}}{U_1}\right)^2}$]

RMS^*_{max} : Maximum dimensionless root mean square of velocity distribution [-]

t : Time [s]

T : Period of velocity oscillation (= $1/f$) [s]

U_1 : Velocity of primary flow [m/s]

U_2 : Velocity of secondary flow [m/s]

U_C : Velocity of continuous flow [m/s]

U_A : Amplitude of velocity oscillation for secondary excited flow [m/s]

U_{max} : Maximum velocity [m/s]

$|\boldsymbol{v}|$: Absolute value of the velocity at an arbitrary point [m/s]

x,y,z : Coordinate axes [m]

z_h : Height of slots (7.0×10^{-2}) [m]

u : Velocity in x direction [m/s]

v : Velocity in y direction [m/s]

Q_1 : Flow rate of primary jet [m^3/s]

Q_2 : Flow rate of secondary flow [m^3/s]

$b_{1/2}$: Jet half width [mm]

Greek symbols

θ : Clockwise Angle from x-axis [°]

θ_c : Deflection angle of jet [°]

θ_1 : Clockwise Angle from x-axis to the first point of intersection between $0.2U_m$ and velocity distribution to [°]

θ_2 : Clockwise Angle from x-axis to the second point of intersection between $0.2U_{max}$ and velocity distribution [°]

ξ : Ratio of momentum between primary flow and secondary flow [-]

ν : Kinematic viscosity (1.506×10^{-5}) [m^2/s]

ζ : Ratio between the velocity of continuous flow and the amplitude of velocity oscillation [-]

ω : Angular velocity [rad/s]

2.3 Experimental setup and method

2.3.1 Experimental equipment

Figure 2-1 shows a schematic of the test section used in the experiments while Figure 2-2 displays an enlarged view of slot outlets and coordinate system. The experimental equipment in this chapter has a constant geometrical parameter with a test platform area of $1m^2$ adjacent to the slot exits of primary and secondary jets. To ensure the two dimensionless characteristics of the experiments and the conducting of visualization experiment, a transparent acrylic plate with the same size as the test platform is placed above it. Except for the upper and lower planes in the z-axis direction, the test section is open to the surrounding atmosphere in all four directions in the *x*-*y* plane including the nearby of the nozzle. The width of the primary slot is $h_1 = 1.0\times10^{-2}$ m and the width of the secondary slot is $h_2 = 2.0\times10^{-3}$ m. The two slots are separated by a baffle with a thickness of 1 mm. And the aspect ratio of the primary and secondary slot are $z_h / h_1 = 7.0$ and $z_h / h_2 = 35.0$, respectively. Although the aspect ratio of the primary slot is $z_h / h_1 = 7.0$ in this chapter, the primary jet is still strictly a three dimensionless fluid. Even the measurement of velocity is taken at the mid-span of the Coanda cylinder, the flow will still affected by the shear layer of the *z* directions. According to previous studies, if the larger the aspect ratio is larger, the flow characteristics are closer to a two-dimensionless fluid. And as the aspect ratio in this study is bigger than some previous study[11,12,13,35], this effect is considered to be negligible. The direction control of the primary jet is not only relied on the secondary flow, but also relied on the Coanda effect created by the cylinder below the secondary slot. And the radius of cylinder is $R = 1.5\times10^{-2}$ m. Above the secondary slot ,there is also a cylinder and a slot similar to those installed in the negative y-axis direction, designed to prevent deflection of the jet due to structural asymmetry. Therefore, in the following experiments, the secondary flow was only be ejected from the secondary slot in the negative direction of the y-axis.

The working fluid used in this study was air, and the primary jet was generated by a blower (Showa DenkiCO., Ltd. U75-2-R313) and was fed into the test section from the primary slot after passing through the plenum tank. The secondary flow was generated by a speaker

(Diecook DD-15L) and a blower (Showa Denki Co., Ltd. U2V-70S). The frequency f and amplitude U_A of the secondary flow were adjusted by a signal generator (Shanghai MCP LG1100 AUDIO GENERATOR) and an amplifier (Shanghai MCP LG1100 audio generator). The steady velocity was adjusted using an inverter (Mitsubishi Electric Corporation FR-D720-0.75K) as a controller for the blower. The switch between injection suction conditions of the secondary flow was achieved by adjusting the valve between the suction port and the injection port of the blower, as shown in Figure 2-1.

To observe the flow pattern of the fluid in the test section, a digital camera (CASIO ex-100pr) was placed on top of the test section to capture pictures. To provide smoke for visualization, a smoke generator (PORTA SMOKE ps-2005) was connected to the inlet of the blower for the primary jet. Finally, two halogen lamps were placed on either side of the test area along the y direction to supply the light for the visualization of the smoke carried by the primary flow.

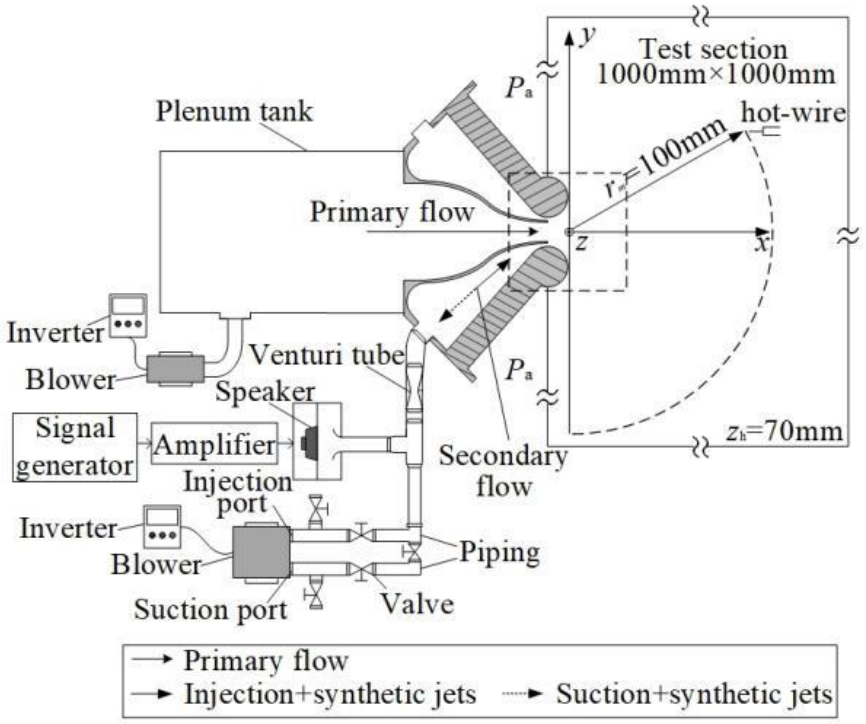

Fig. 2-1. Schematic of the test section used in the experiments.

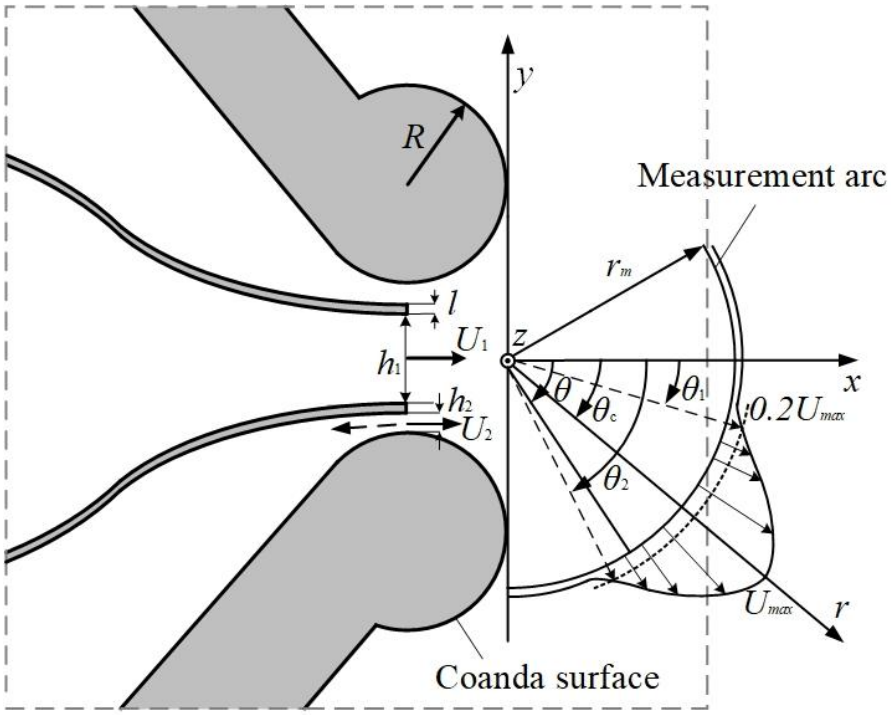

Fig. 2-2. Schematic of slot and Coanda surface.

2.3.2 Velocity measurement method

To investigate the deflection and unsteady characteristics of the primary jet in the test section under various secondary flows, two measurement methods were utilized to measure flow velocity distribution. One method, illustrated in Figure 2-2, established the origin z at the intersection of the centerline of the primary slot and the tangent line of the cylinder. The measurement arc had a radius of r_m = 100 mm and an angle range of θ = -30° to 90°, with 60 measurement points evenly spaced along the arc with an angle interval of 2°. The other method employed three straight lines as the measurement area, as shown in Figure 2-3. The measurement range covered x = 50, 100, 150 mm, and y= -150~50 mm, with 100 measuring points set on each line at a measurement interval of 2 mm.

The study employed a hot-wire anemometer (KANOMAX MODEL 1011, Smart CTA 7250) and two I-type probes (KANOMAX 0251R-T5) to conduct flow velocity measurements. Calibration was accomplished by placing the Pitot tube and I-type probe at the same position of a wind tunnel cross-section and measuring 13 sets of velocity of flow from 0 m/s to approximately 20 m/s, and record the corresponding velocity and voltage measured by Pitot tube and I-type probe respectively. These results were then transferred to a computer and a voltage-velocity fitting curve was generated from the data obtained from two instruments.

During the experiment, an I type probe was installed on an electronic traverser to measure the velocity of the primary jet at the primary slot section and the velocity distribution on the test section. Additionally, another I-probe was installed at the midpoint of the cross-section of Venturi pipe to measure the velocity of the secondary flow in the Venturi pipe. This result was used to calculate the velocity of secondary flow at the cross-section of secondary slot exit cross-section by multiplying the cross-section area of Venturi pipe and then divide the cross-section area of secondary slot exit. The decision to use this method was based on the preliminary experiment of this study, it was found that if the velocity of the secondary flow is measured at the cross-section of the secondary slot while there is a large proportion of suction process within one cycle of the secondary flow, due to the influence from the primary jet, the velocity distribution at the cross-section of secondary slot exit will be uneven, which makes it

impossible to accurately measure the true velocity of the secondary flow. But this problem can be avoided by the measuring the secondary flow at the Venturi pipe.

In addition, by using the first arc measurement method in the experiments, the direction of the hot-wire was always parallel to the x-axis, rather than the normal direction of the measurement arc. Although this measurement method may lead to deviation at some measurement points which are far from the measurement point of $\theta = 0^\circ$, we have confirmed in the preliminary experiments that the measured overall time-averaged velocity over the circular arc is approximately equal to the time-averaged velocity in the normal direction of the arc, i.e. $|\boldsymbol{v}| = \sqrt{u^2 + v^2} \approx v_r (v_r / |v| > 0.9)$. And the sampling time and frequency were 14s and 10000Hz respectively.

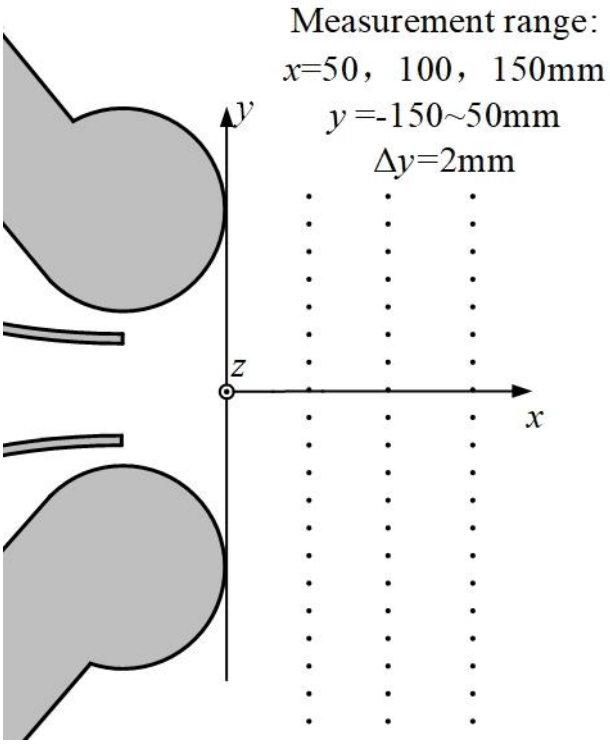

Fig. 2-3. Measurement method of linear velocity distribution.

2.3.3 Experimental evaluation

In the study of this chapter, because of the use of multiple excitation flows and continuous flows, so it is necessary to define the velocity of the secondary flow U_2 :

$$U_2 = \sqrt{\frac{1}{T}\int_0^T (U_C + U_A sin\omega t)^2 dt} \qquad (2\text{-}1)$$

Here, U_C is the velocity of the steady component of the secondary flow [m/s], U_A is the amplitude of velocity oscillation of the secondary flow [m/s], T is the velocity oscillation period, and ω is the angular velocity [rad/s]. The velocity of the primary flow is set as a constant U_1=10 m/s (Reynolds number Re = 6.64×10^3)in this chapter, so that the momentum ratio between the primary and secondary flows ξ can be adjusted by simply changing the velocity of the secondary flow. The definition of the momentum ratio ξ is as followed:

$$\xi = \frac{h_2 U_2^2}{h_1 U_1^2} \qquad (2\text{-}2)$$

For the formula above, h_2 is the width of the secondary slot [mm], U_2 is the velocity of the secondary flow [m/s], h_1 is the width of the primary slot [mm] and U_1 is the velocity of the primary flow [m/s]. Besides the momentum ratio ξ, the dimensionless frequency is one of the main evaluation parameters and it is only applicable to the experiment conditions for the excitation flow as a secondary flow. According to the results of the previous study[36], the flow characteristics of a synthetic jet depend on the dimensionless frequency. Although there is a difference in momentum between an excitation flow and a synthetic jet, both are capable of triggering velocity fluctuations. The dimensionless frequency is defined as:

$$f^* = \frac{f h_1}{U_1} \qquad (2\text{-}3)$$

Here, f is the vibration frequency of secondary flow [Hz], h_1 is the width of the primary slot [mm] and U_1 is the velocity of the primary flow [m/s]. In order to study the effect of the excitation flow on the primary flow at different frequencies, three different frequencies (f = 20Hz, 50Hz and 80 Hz) were used in the experiments for comparison. Finally, in order to distinguish the different secondary flow, the ratio of the steady-state velocity component of the secondary flow to the amplitude of the velocity fluctuations of the secondary flow ζ was used as a new parameter as shown in equation (2-4):

$$\zeta = \frac{U_C}{U_A} \tag{2-4}$$

U_C is the velocity of the steady component of the secondary flow [m/s] and U_A is the amplitude of velocity oscillation of the secondary flow [m/s]. In addition, the purpose of this chapter is to investigate the effect of the secondary flow on the deflection characteristics of the primary jet. However, using different operational steps in the experiment might influence the flow pattern such as the hysteresis effect, so it is necessary to generate the primary jet at the beginning of the experiment and then generate the secondary flow while the primary jet has stabilized.

For the calculation of the deflection angle of the jet, from the measured velocity distribution, the part of $|v| > 0.2|U_{\max}|$ was considered as a jet, and the deflection angle θ_c is obtained by integrating the region from θ_1 to θ_2 as the integration range as shown in (2-5)

$$\theta_c = \frac{1}{\int_{\theta 1}^{\theta 2} |v| d\theta} \int_{\theta 1}^{\theta 2} |v| \theta d\theta \tag{2-5}$$

Here, θ_1 is the angle of the first point of intersection between $0.2U_{\max}$ and velocity distribution [°], θ_2 is the angle of the second point of intersection between $0.2U_{\max}$ and velocity distribution [°], $|\boldsymbol{v}|$ is the absolute value of the velocity at any point [m/s], and θ is the clockwise angle from x-axis[°]. The reason for ignoring the part of $|v| < 0.2|U_{\max}|$ is that the hot-wire anemometer is calibrated by a Pitot tube, and the Pitot tube is very difficult for low

velocity measurement[37,38] (flow velocity below 1 m/s). Therefore the result of integrating the overall velocity distribution might be inaccurate. It is necessary to mention that the relative error was less than 3% when the deflection angle was compared with the values obtained when the threshold was 0.2 U_{max} and 0.3 U_{max}.

2.3.4 Numerical simulation method

In this chapter, Ansys Fluent was utilized to simulate some of the experimental conditions for comparison. The basic equations of the Ansys Fluent simulation are consist of the momentum conservation Navier-Stokes equations and the mass conservation equations. In this study, the working fluid was assumed to be a two-dimensional incompressible viscous fluid and the SST k-ω turbulence model was employed. Figure 2-4 depicts the numerical simulation domain and the boundary conditions used in the simulation. As all four sides of the test section in experiment were open to the atmosphere, the same setting was used in the simulation domain of Ansy Fluent. For the rigid slots and baffle surfaces, the boundary conditions were set as no-slip, while the rest of the boundary surfaces were set to constant static pressure conditions (p=0 (Pa)). The shape of the simulation domain was a combination of a semicircle with a radius of 1500 mm and a rectangle with a length of 1500 mm and a width of 500 mm. The center of the semicircle was located at the intersection of the centerline of the primary slot and the tangent line of the cylinder. The flow velocity can be adjusted at each input port, and the velocity of the primary slot and secondary slot can be calculated through the ratio of the input port width to the width of the primary and secondary slot width.

Figure 2-5 shows an magnified view of the typical grid near the slots. As the shape of the slot has parts of curve, the triangle was chosen as the shape of the mesh.. Since the width of primary and secondary flow are small compared to the entire simulation domain, the mesh size near the slot is set to 0.2 mm .and for the mesh far away form the slot, the maximum size of mesh is 3mm. For the entire simulation domain, the mesh number is 319541 and the node number is 175940.

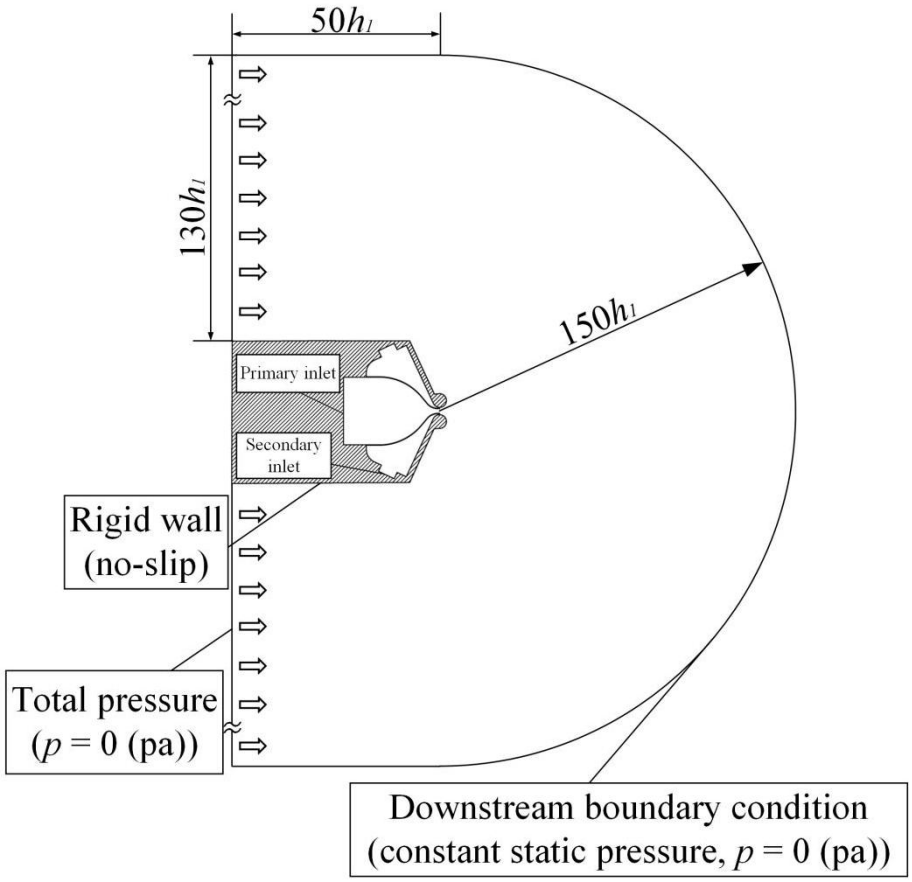

Fig. 2-4. Numerical simulation domain and boundary condition.

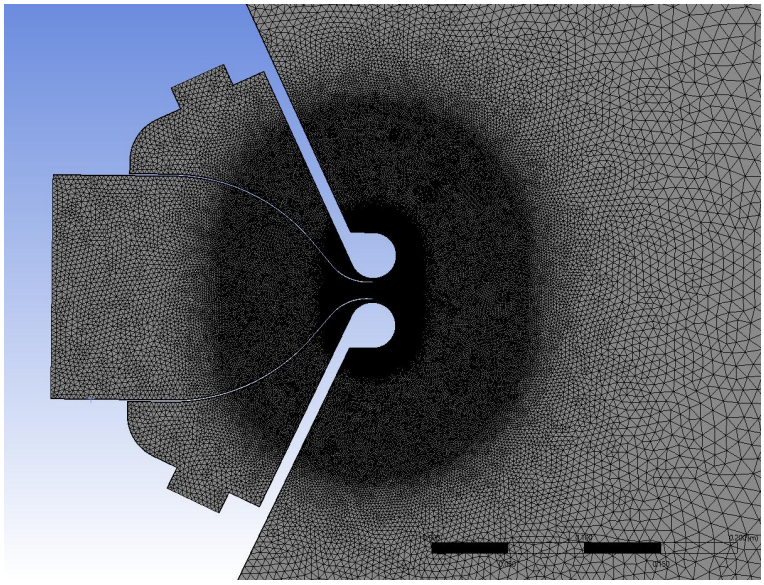

Fig. 2-5. Magnified view of the typical grid near the slots.

2.4 Results and Discussion

To validate the symmetry of the experimental equipment used in this study, a visualization experiment was conducted with a primary flow (U_1=10m/s,U_2=0m/s) as shown in Figure2-6(a). Additionally, Figure2-6(b) presents the CFD simulation outcome for U_1=10m/s and U_2=0m/s for the same purpose. The result of Figure2-6(a) demonstrate that the primary jet moves straight ahead after been ejected from the primary slot. Subsequently, under the effect of the shear layer, the primary flow gradually spreads to the both sides , and as the increases of distance on the *x*-direction , the width of the fluid become wider which is consistent with the general jet characteristics. For the CFD result showed in Figure 2-6(b) is similar to Figure 2-6(a), confirming that the experimental equipment and CFD model possess sufficient symmetry.

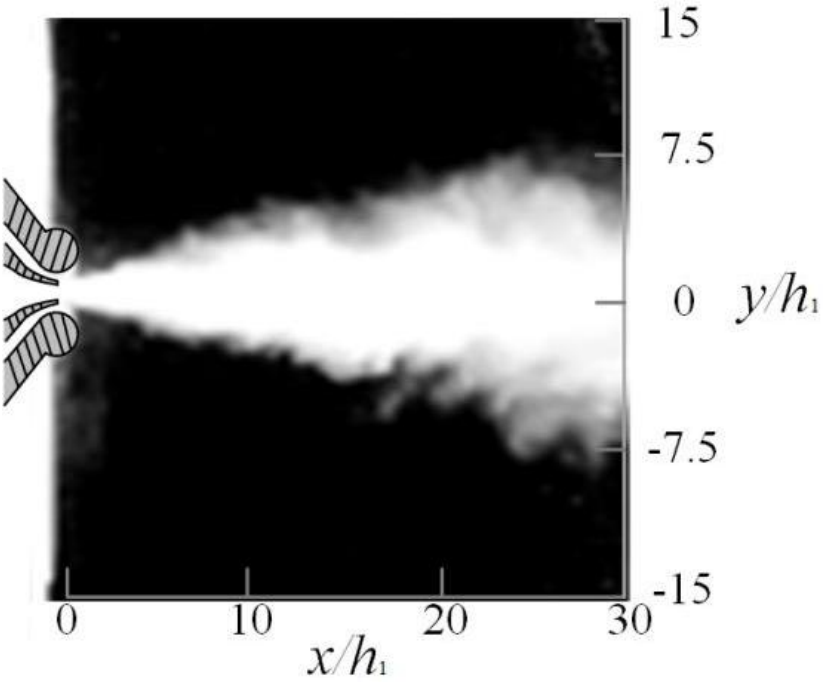

(a) Visualization result for U_1=10m/s, U_2=0m/s

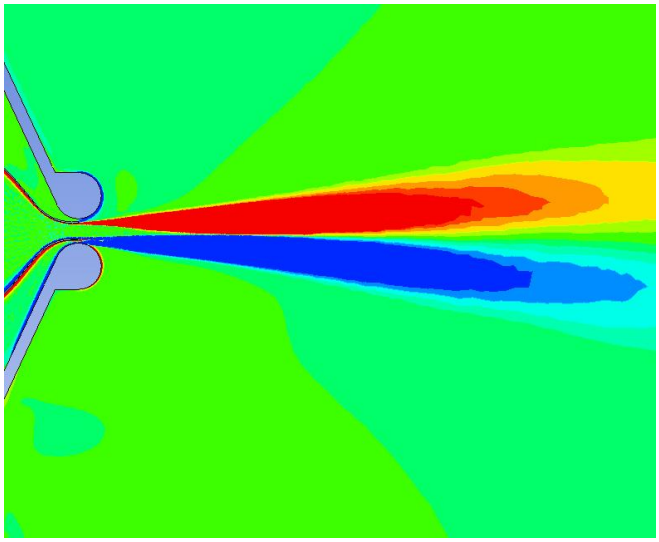

(b) CFD result for U_1=10m/s, U_2=0m/s

Fig. 2-6. Symmetry confirmation results.

2.4.1 Influence of ζ, ξ and f^* on jet flow characteristics

As previously mentioned, this study introduces a new parameter, the ratio of the steady-state velocity component of the secondary flow to the amplitude of the velocity fluctuations of the secondary flow ζ. To investigate the effect of the ζ on the primary flow, 15 different value of ζ were selected for comparison in the range within the range of $-\infty \leq \zeta \leq \infty$, and among these value the secondary flow types can be classified into 6 types. Figure 2-7 depicts the phase-averaged waveforms of typical secondary flows under the ratio of momentum $\xi = 0.08$, with 50 repetition of data collection for the calculation of phase average. The horizontal axis is the dimensionless time t/T, while the vertical axis is the dimensionless secondary velocity u_2/U_1. As the measurement results from the hot-wire anemometer can only show the absolute velocity of flow $|v|$, the suction process in one circle of secondary flow was inverted and presented as a negative value. As shown in Figure 2-7, two of the typical types are the continuous injection jet and the continuous suction flow as the continuous flow; the other four types are the pulsed injection jet, the pulsed suction flow, the synthetic jet and the hybrid synthetic jet as the excitation flows. The momentum is not zero in for other three excited flow except for the synthetic jet and the waveform of the excited flow can be considered as a sine wave based on the measured results.

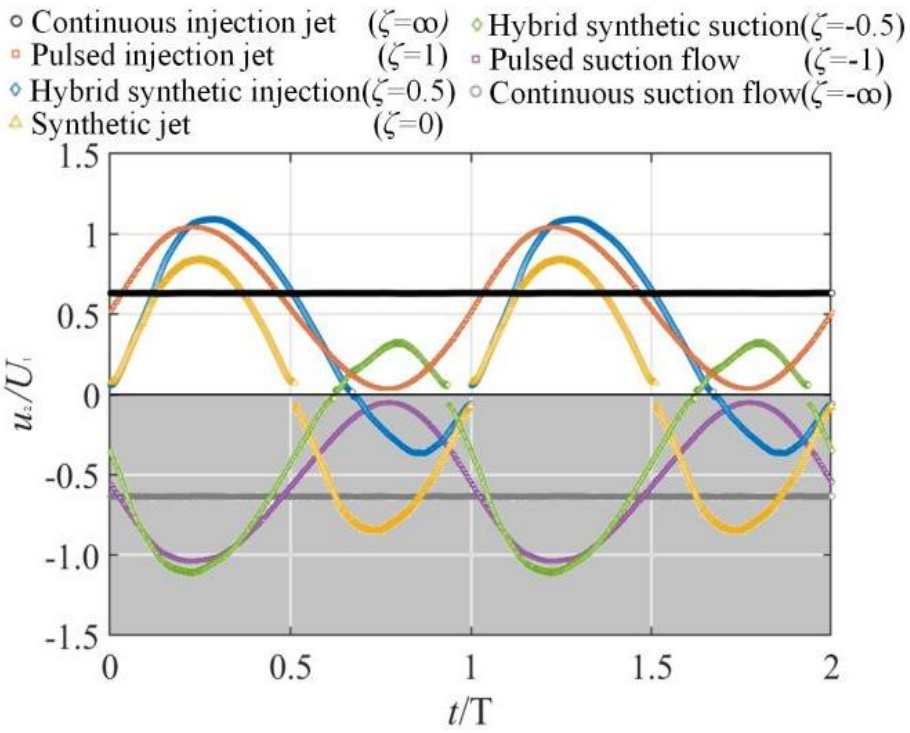

Fig. 2-7. Phase averaged wave forms for typical secondary flow under the ratio of momentum $\xi = 0.08$. The number of repetitions of data collection is 50.

Based on the research of Kobayashi[24], the deflection ability of the primary flow is dependent on the secondary flow when it is a synthetic jet. As the momentum coefficient increase, the deflection angle also increases until it reaches the saturation zone. Since the critical point of momentum coefficient for entering the saturation zone is around $\xi = 0.06 \sim 0.08$, in order to focus on studying the effect of ζ, the momentum coefficient was set to $\xi = 0.08$ for this chapter.

Next, the visualization experiments were conducted based on various typical secondary flow as depicted in Figure 2-7. Figure 2-8 shows visualization observations for various ratios between the velocity of continuous flow and the amplitude of velocity oscillation ζ under the condition of $\xi = 0.08$. As the excited flow with medium frequency is more representative than the high frequency excited flow ($f^* = 0.08$) and the low frequency excited flow ($f^* = 0.02$), the frequency was set to $f^* = 0.05$ in this experiment. Therefore, the exposure time of the camera was set to 1/50s. The secondary flows in Figure 2-8(a),(h) are continuous flows with $\zeta = -\infty$ and ∞ respectively,and the secondary flows in Figures 2-8(b)~(g) are excited flow with ζ = -2.5, -0.5, 0, 0.5, 2.5. For ζ = -2.5, -0.5, 0 and 0.5, the primary flow has a obvious deflection which proves that excitation flow except the synthetic jet also have the deflection ability. For ζ = 1, although the width of the primary flow is wider than that for $\zeta = \infty$, the deflection of angle between two parameters has no big difference. Clearly compared ζ = 1 and ∞ to other conditions, there is no suction process in the former two conditions. In the previous study, although the deflection achieved by a function of momentum coefficients has a problem of narrow controllable region, using continuous suction flow as a secondary flow to conduct the deflection of primary flow has been prove effective. Furthermore, Mason[11] found that the primary flow can be deflected by adjusting the momentum coefficient between the primary flow and secondary flow under a certain shape condition of slot width and radius of Coanda surface. However, the values for the width ratio of primary to secondary slot in this experiment is different from his experiment parameter, the results in Figure2.8(h) has no contradiction with Mason's research.

Figure 2-9 shows the time-averaged velocity distribution for various ratios between the velocity of continuous flow and the amplitude of velocity oscillation ζ under the condition of

$\zeta = 0.08$, f^*=0.05. Figures 2-9(a)~(h) respectively represent the velocity distribution for ζ = -∞ -2.5, -0.5, 0, 0.5, 2.5, ∞ which are corresponding to Figures 2-8(a) ~ (h). And the arrows in the diagram indicate the maximum velocity of velocity distribution. For Figure2-9(g) and (h), the position of the maximum velocity in the y-direction only change slight for different x/h_1 coordinates. For Figures2-9(a)~(f), with the x distance increases, the maximum velocity of velocity distribution all deflect significantly in the y direction. Compared to the continuous flow as a secondary flow (ζ =∞ and -∞), the flow width of the excited flow (ζ = -2.5, -0.5, 0, 0.5 and 2.5) as a secondary flow is wider. And when the proportion of U_A is larger in the velocity of secondary flow U_2, the change of the width of the flow is more pronounced. Combining the results in Figure 2-9 and Figure 2-8, it can be decided that it is feasible to control the jet direction by varying ζ.

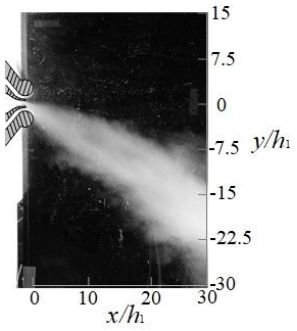

(a) $\zeta = -\infty$ (Continuous suction flow)

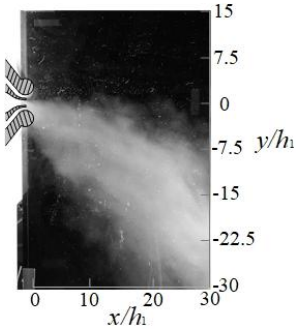

(b) $\zeta = -2.5$ (Pulsed suction flow)

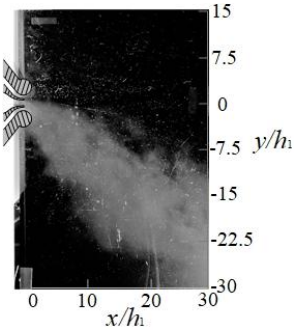

(c) $\zeta = -1$ (Pulsed suction flow)

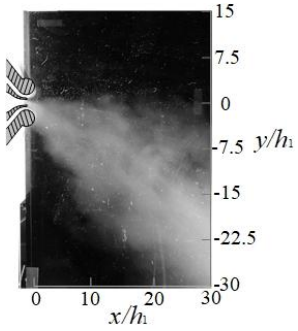

(d) $\zeta = -0.5$ (Hybrid synthetic suction)

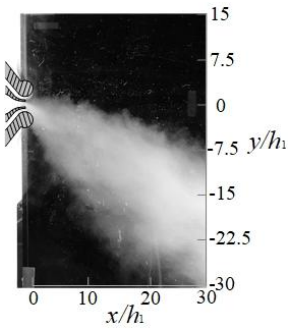

(e) $\zeta = 0$ (Synthetic flow)

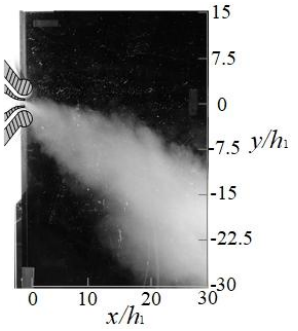

(f) $\zeta = 0.5$ (Hybrid synthetic injection)

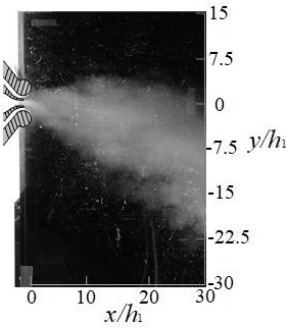

(g) $\zeta = 1$ (Pulsed injection jet)

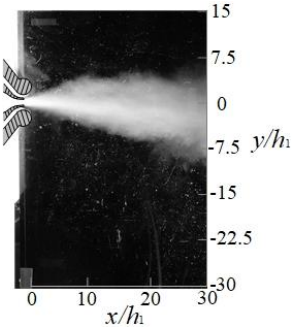

(h) $\zeta = \infty$ (Continuous injection jet)

Fig. 2-8. Flow visualization for various ratios between the velocity of continuous flow and the amplitude of velocity oscillation ζ. The ratio of momentum $\xi = 0.08$, dimensionless frequency $f^* = 0.05$, and frequency of synthetic jet $f = 50$ Hz. The time of exposure is set at 1/50 s.

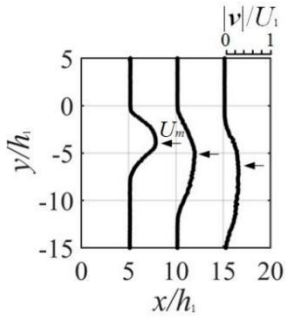

(a) $\zeta = -\infty$ (Continuous suction flow)

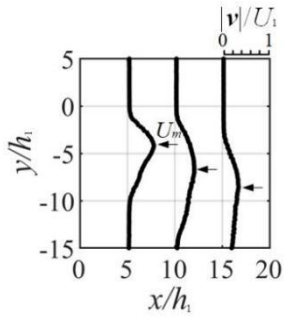

(b) $\zeta = -2.5$ (Pulsed suction flow)

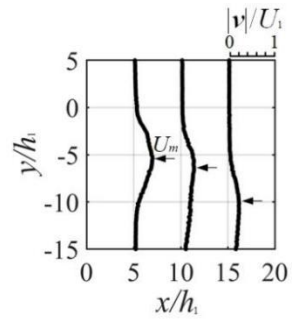

(c) $\zeta = -1$ (Pulsed suction flow)

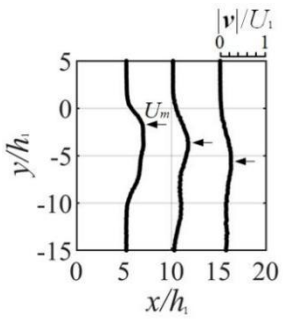

(d) $\zeta = -0.5$ (Hybrid synthetic suction)

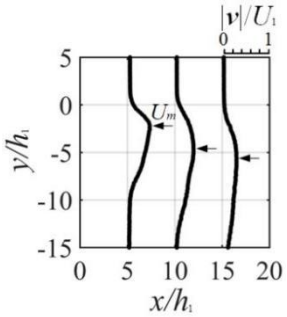

(e) $\zeta = 0$ (Synthetic flow)

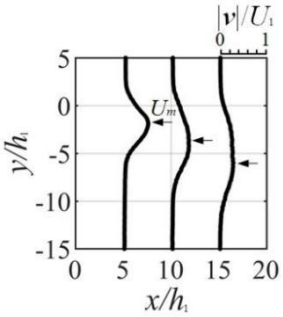

(f) $\zeta = 0.5$ (Hybrid synthetic injection)

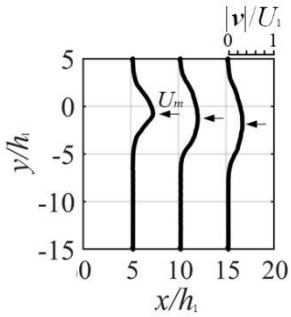

(g) $\zeta = 1$ (Pulsed injection jet)

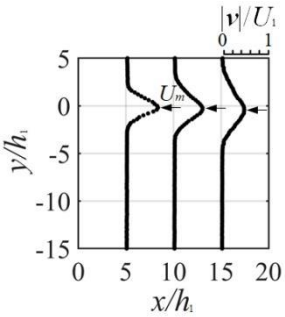

(h) $\zeta = \infty$ (Continuous injection jet)

Fig. 2-9. Velocity distribution for various ratios between the velocity of continuous flow and the amplitude of velocity oscillation ζ. The ratio of momentum $\xi = 0.08$, dimensionless frequency $f^* = 0.05$, and frequency of synthetic jet $f = 50$ Hz.

Figure 2-10 illustrates the velocity distribution of the primary flow on a measurement arc with radius of r_m = 100 mm under the condition of the momentum ratio ξ = 0.08 and the dimensionless frequency f^* = 0.05. The horizontal axis is the clockwise angle θ from x-axis, and the vertical axis is the dimensionless absolute velocity $|v|/U_1$. Figures 2-10(a) and (b) illustrate the results for ratios between the velocity of continuous flow and the amplitude of velocity oscillation $\zeta \geq 0$ and $\zeta \leq 0$, respectively. For the conditions of momentum ratio ξ and dimensionless frequency f^* are constant, it can be observed that the profile of the time-averaged velocity distribution including the center position of the jet, maximum velocity, and jet half width are dependent on the value of ζ. For the continuous flow as a secondary flow, the time-averaged velocity profiles all resemble a Gaussian distribution. And for the excited flow as a secondary flow, the width of the velocity distribution becomes larger while the maximum velocity decreases, and even two peaks present in the velocity distribution for certain parameters with larger proportion of U_A. In addition, The results also show that the deflection angle of the secondary flow with a negative constant velocity is greater for that of the secondary flow with a positive constant velocity. Therefore, It can be inferred that the secondary flow with suction period has better deflection ability under the conditions of this experiment.

Figure 2-11 depicts the relationship between various ratios of the velocity of continuous flow to the amplitude of velocity oscillation ζ and deflection angle θ_c under conditions of dimensionless frequencies f^*=0.05 and the momentum ratio ξ = 0.08. The horizontal axis represents the velocity of continuous flow and the amplitude of velocity oscillation ζ. The vertical axis represents the deflection angle of θ_c. The three curves from bottom to top in Figure2-11 have dimensionless frequencies of f^* = 0.02, 0.05 and 0.08 respectively. The two sides of the curves represent the deflection angles of the continuous secondary flow. From Figure 2-11, there are differences in the deflection angle among the three curves with different f^*, for instance, as the dimensionless f^* increases, the primary flow has a larger range of adjustable deflection angles and a larger maximum deflection angle. On the other hand, while utilizing different dimensionless frequencies f^* for secondary flow has effect on the magnitude of the deflection angle, three curves show a similar trend. For instance, the

deflection angle θ_c varies smoothly from 0° to approximately 40° by adjusting ζ. Within the region of $-1 \leq \zeta \leq 1$, the deflection angle θ_c reduces as the time taken for the secondary flow to exhibit negative velocity diminishes in one cycle of velocity fluctuation. Within the range of $-\infty < \zeta \leq -1$, it is apparent that θ_c for all f^* is greater than that for the continuous suction flow used as a secondary flow $\zeta = -\infty$. Based on the outcomes in Figure 2-10 and Figure 2-11, it can be inferred that the deflection angle can be adjusted in a wide range by combining the ratio between the velocity of continuous flow and the amplitude of velocity oscillation ζ and dimensionless frequency f^*. In addition, it is feasible to smoothly adjust the deflection angle without altering the frequency, which was previously deemed impossible. Furthermore, for the secondary synthetic jet with a middle or high frequency (f^*=0.05, 0.08), it is possible to achieve a deflection angle almost equivalent to steady continuous suction (ζ=-∞) without sucking the primary jet on the surface of cylinder.

Next experiment chose three secondary flows with good deflection ability from Figure 2-11 to analyse the effect of the momentum ratio ξ and dimensionless frequency f^*on the deflection angle θ_c. The ratios between the velocity of continuous flow and the amplitude of velocity oscillation are $\zeta = -\infty$ (secondary suction flow), $\zeta = -1$ (secondary pulsed suction flow) and $\zeta = 0$ (synthetic jet) respectively. Figure 2-12 shows the relation between the momentum ratio ξ and the deflection angle θ_c for f^* = 0.02, 0.05 and 0.08. The horizontal axis is the momentum coefficient ξ and the vertical axis is the deflection angle θ_c. For the condition of $\zeta = -1$, with the increase of momentum ratio ξ, the deflection of flow jumps immediately to the saturation region after a short dead water region ($\xi \leq 0.01$). And for the condition of $\zeta = 0$, the deflection angle θ_c changes more smoothly as the momentum coefficient ξ increases, and then reaching the saturation region after a controllable region of $0 \leq \xi \leq 0.06$. It is inferred that the primary flow has a greater deflection angle using the pulsed suction flows as a secondary flows, but fine adjustment of the deflection angle is unachievable.

Figure 2-13 depicted that the relation between various dimensionless frequency f^* and the jet half width $b_{1/2} / U_{max}$ with approximate value of deflection angle $\theta_c \approx 30°$. The horizontal axis represents dimensionless frequency f^* and the vertical axis represents the dimensionless jet half width $b_{1/2}U_1 / h_1U_{max}$. It is apparent that the dimensionless jet half width of the

primary jet under the influence of the excited secondary flow are significantly larger than those of the secondary continuous suction located at the right side of the diagram. This result is consistent with the visualization results previously present. And comparing conditions of various excited flow, it can be seen that the larger the dimensionless frequency the small the dimensionless jet half width. For instance, when f^* = 0.02, dimensionless jet half width $b_{1/2}U_1$ / h_1U_{max} are bigger than 17. But for f^* = 0.08, the variation of jet half width value is relatively small which might because of the the influence of the different dimensionless frequencies. And besides a good deflection capability, the relatively stable flow pattern such like the curve of f^* = 0.08 in this diagram might also be one of the conditions that determine its suitability for a specific application. Based on the previous study[24], among different magnitude of the dimensionless frequencies, the unsteady characteristics of the flow pattern are also different. For instance, the time variation of the flow field was larger when the dimensionless frequency was smaller because of the repeated attachment and separation of the jet on the surface of the cylinder, whereas the time variation of the flow field was smaller when the dimensionless frequency was larger. Secondly, for arbitrary dimensionless frequency conditions, the magnitude of the half amplitude is significantly increased when the constant velocity is negative and the vibration amplitude U_A is proportionally larger. However with the introduction of the new parameter ζ, the unsteady characteristics of the jet may also be different. It is necessary to investigate the unsteady characteristics under different ζ conditions in next section.

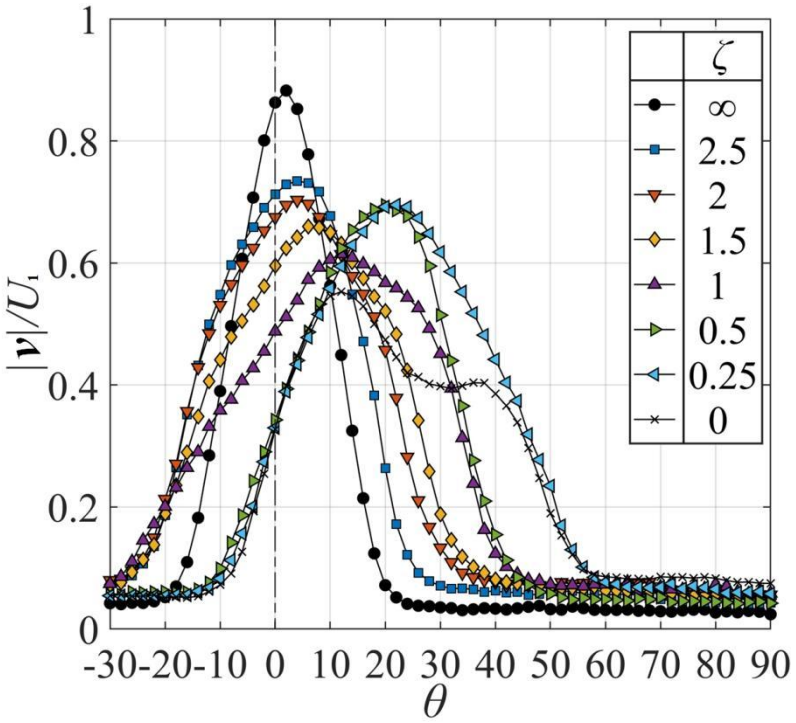

(a) $\zeta \geq 0$

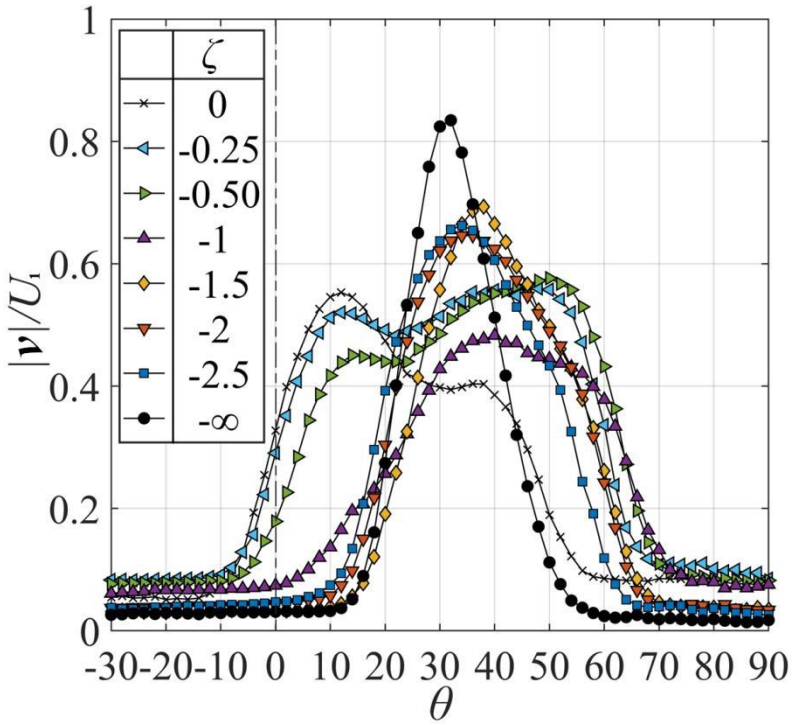

(b) $\zeta \leq 0$

Fig. 2-10. Dimensionless time-averaged velocity distribution. The ratio of momentum ξ settled at 0.08. The dimensionless frequency f^* and the frequency of synthetic jet f settled at 0.05, 50Hz.

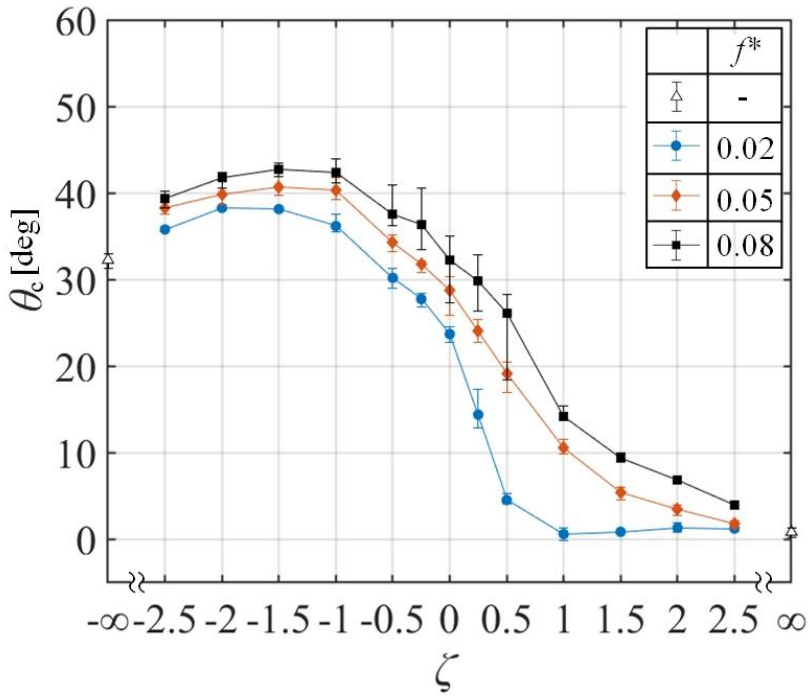

Fig. 2-11. Relation between various ratios between the velocity of continuous flow and the amplitude of velocity oscillation ζ and deflection angle θ_c under different dimensionless frequencies f^*.The ratio of the momentum ξ settled at 0.08.

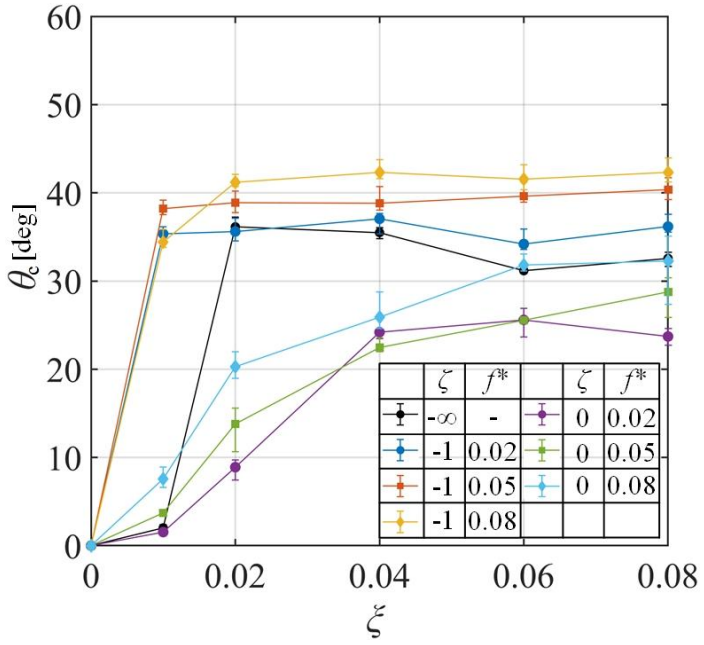

Fig. 2-12. Deflection angle comparison for various ratios between the velocity of continuous flow and the amplitude of velocity oscillation $\zeta = -\infty$, $\zeta = -1$, $\zeta = 0$ for different ratios of momentum, ξ, and different dimensionless frequencies f^*.

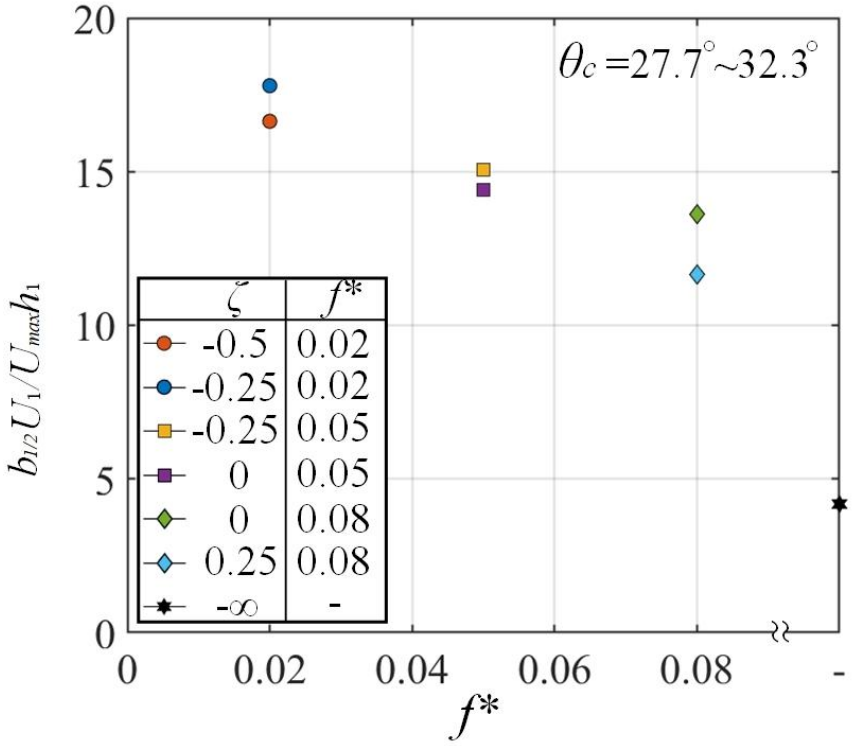

Fig. 2-13. Relation between dimensionless ratio of maximum velocity U_{max} to jet half width $b_{1/2}$ with a similar deflection angle of $\theta_c \approx 30^\circ$ while the $\xi = 0.08$.

2.4.2 Unsteady flow characteristics analysis

In order to investigate the unsteady characteristics of a deflected primary jet with typical secondary flow, three visualization experiments were conducted to observe three different types of secondary flow with ζ value of -∞, -1 and 0. To achieve this objective, the experimental setup involved focusing the camera on the area of slots and the cylinder surface. Furthermore, an oscilloscope was connected to a hot-wire anemometer to correlate the instantaneous flow field with the fluctuating position of the secondary flow.

Figure 2-14(a) and (b) depict a visualization and CFD result, respectively, for a secondary continuous suction flow under a momentum ratio of $\xi = 0.08$. The corresponding visualization results for secondary pulsed suction(ζ = -1) and secondary synthetic jet (ζ = 0) with a momentum ratio of ξ = 0.08 and a dimensionless frequency of f^* = 0.05 are shown in Figure2-15 and 2-16. The photographs of visualization were taken at a frame rate of 960Hz. Panels (a) – (e) in Figure2-15 and 2-16 show the behavior at different times: t/T=0, 0.25, 0.5, 0.75, and 1.0. Furthermore, the video observations facilitated the estimation of the large-scale vortex center (blue for clockwise and red for counter-clockwise), which is provided as a reference for the study. Upon comparing the visualization result in Figure 2-14(a) with the CFD results in Figure 2-14(b), it can be observed that the deflection characteristics of the two are similar. The jet exhibits good deflection capability and does not generate vortices downstream. Comparing Figure 2-14(a) with Figure 2-15, the jet deflection angle appears to be similar. However, there is a notable difference in the flow structures observed between the two cases. Specifically, while no large-scale vortices are observed in Figure 2-14(a), a staggered vortex street is formed in Figure 2-15. This difference can be attributed to the synchronization between the velocity shear layer and the secondary excited flow, which leads to the formation of the vortex street. At t/T = 0, as shown in Figure 2-15(a), the secondary flow is observed to still be increasing in negative velocity and the jet near the secondary slot is already adhering to the Coanda surface. This occurrence signifies the manifestation of the Coanda effect resulting from the influence of the pulsed suction flow. At t/T = 0.25, the secondary suction flow reaches its maximum output time and the jet on the cylinder surface

progresses further towards the cylinder's back edge, thereby producing a counter-clockwise rotating vortex that rolled up at the upper part of the primary jet. Next, form t/T = 0.5 to t/T = 0.75, the absolute velocity of the pulsed suction flow gradually decreases until it reaches 0. At t/T = 0.5, the jet on the cylinder surface reaches its furthest separation point in a cycle of the secondary flow . Due to the viscosity of the cylinder surface, a clockwise rotating vortex is created in the lower part of the jet. At t/T = 0.75, the velocity of secondary flow reaches 0, resulting in the complete separation of the primary flow from the cylinder surface. However, the duration of complete separation is brief, it is notable that the jet is dragged to the cylinder surface at t/T=1. In contrast, the attraction and separation process of the synthetic jet on the cylinder, as depicted in Figure 2-16, is more pronounced. For instance, at t/T=0 immediately after the suction process, the primary jet remains attached to the cylinder surface though the Coanda effect. However, during the injection phases at t/T=0.25 and 0.5, the secondary flow lacks the ability to deflect the primary jet, due to the injection process. As a result, the primary flow completely separates from the cylinder surface. When comparing Figure2-14(a), 2-15 and 2-16, the farthest separation point is notably greater for the pulsed suction flow or the synthetic jet as a secondary flow than for the continuous suction flow. However, based on the results in Figure 2-14(a), the difference in deflection angle between the synthetic jet and continuous suction flow is negligible. For the pulsed suction flow as a secondary flow, although it only consist of suction processes, its velocity fluctuations cause separation and attraction of the primary jet on the cylinder surface might be the reason for better deflection ability of the pulsed suction flow.

Figures 2-17(a) and (b) present the CFD results obtained under the same conditions as Figures 2-15 and 2-16, respectively. While there are quantitative differences in the deflection characteristics of the results, including deflection angle, separation point position, and vortex size compared to the visualization results, the downstream flow patterns are considered consistent. In both cases, the downstream jet emits alternating pairs of vortices over time. Figure 2-18(a) and (b) present the velocity distribution and root mean square values of the overall velocity fluctuations measured on an arc of radius r_m / h_1 = 10 under the momentum ratio ξ = 0.08 and dimensionless frequency f^* = 0.05. The horizontal axis of Figure 2-18(b)

represents the ratio between the velocity of continuous flow and the amplitude of velocity oscillation ζ, and the vertical axis represents the dimensionless root mean square value *RMS** on the velocity distribution. Panels (i), (ii), and (iii) show the results of $\zeta = -\infty$, $\zeta = -1$ and $\zeta = 0$. The results indicate that the maximum value of *RMS** for $\zeta = -\infty$ is significantly smaller than that of $\zeta = -1.0$ and $\zeta = 0$, and the difference in maximum value of *RMS** between $\zeta = -1.0$ and $\zeta = 0$ is approximately 3%. Furthermore, the jet half-widths and range of velocity fluctuations for $\zeta = -1$ and $\zeta = 0$ are larger than these of $\zeta = -\infty$ due to the generated Karmen vortex.

Figure 2-19 presents the relationship between the maximum dimensionless root mean square value RMS^*_{max} measured on the arc and the ratio between the velocity of continuous flow and the amplitude of velocity oscillation ζ under the momentum ratio $\xi = 0.08$. The horizontal axis represents the ratio between the velocity of continuous flow and the amplitude of velocity oscillation ζ, and the vertical axis represent the maximum dimensionless root mean square value RMS^*_{max}. When the secondary flow is steady ($\zeta = -\infty$ or ∞), although the RMS^*_{max} is smaller compared to the other conditions, the difference between the maximum and minimum values is approximately 9% in the experimental range. RMS^*_{max} tends to increase slightly as f* decreases, except for a few cases.

(a) Visualization observation.Photograph was taken at the frame rate of 960 Hz

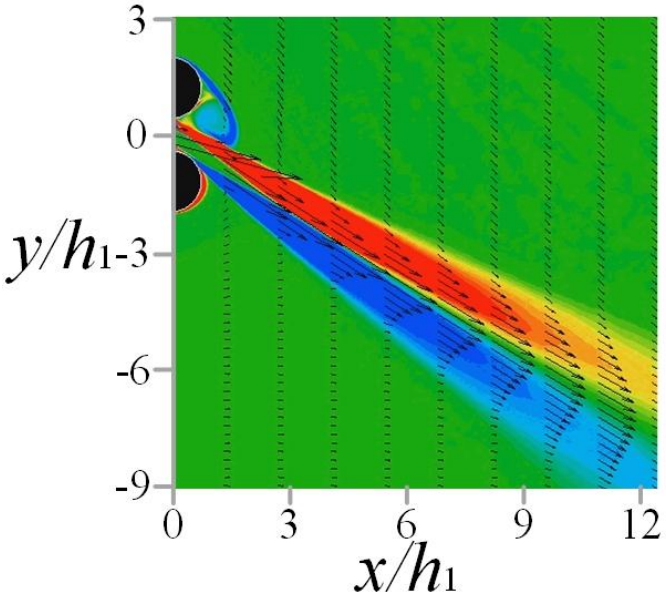

(b) CFD result

Fig. 2-14. Flow visualization and CFD result of $\zeta=-\infty$.

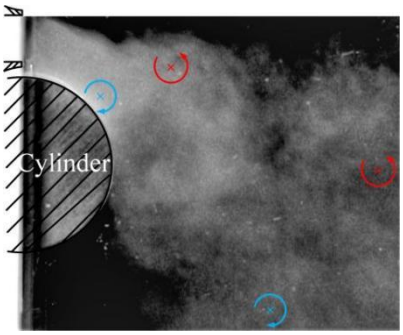

(a) $\zeta = -1$; $t/T = 0$

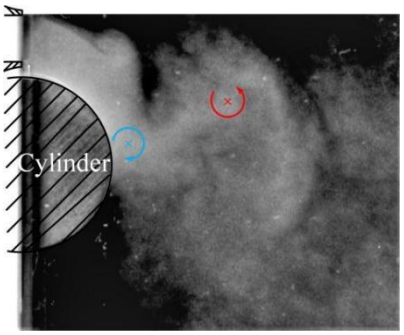

(b) $\zeta = -1$; $t^*U_1/h_1 = 25$; $t/T = 0.25$

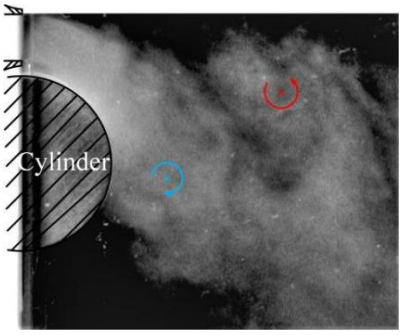

(c) $\zeta = -1$; $t^*U_1/h_1 = 50$; $t/T = 0.5$

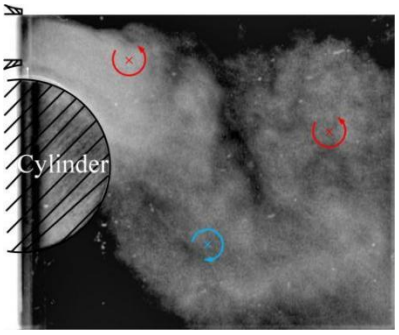

(d) $\zeta = -1$; $t^*U_1/h_1 = 75$; $t/T = 0.75$

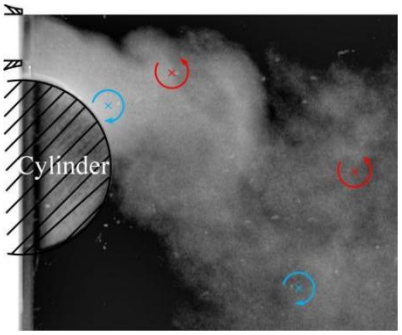

(e) $\zeta = -1$; $t^*U_1/h_1 = 100$; $t/T = 1$

Fig. 2-15. Flow visualization of the ratio between the velocity of continuous flow and the amplitude of velocity oscillation $\zeta = -1$. The dimensionless frequency f^* settled at 0.05. Photographs were taken at the frame rate of 960.

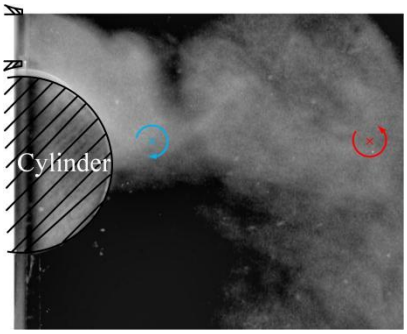

(a) ζ =0; t/T = 0

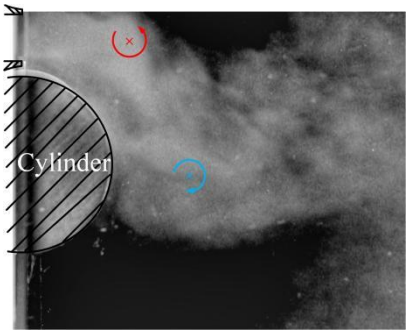

(b) ζ = 0; tU_1/h_1 = 25; t/T = 0.25

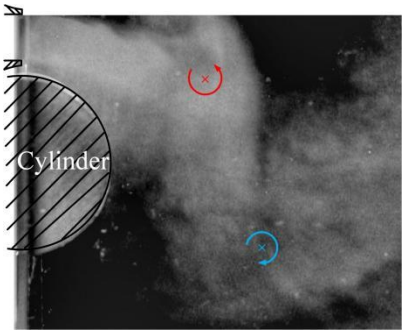

(c) ζ = 0; tU_1/h_1 = 50; t/T = 0.5

(d) ζ = 0; tU_1/h_1 = 75; t/T = 0.75

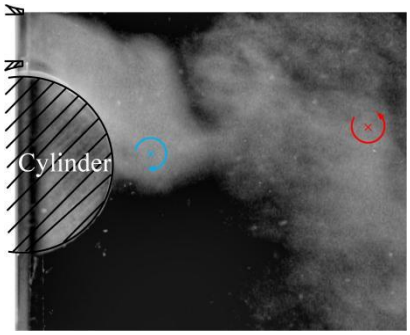

(e) ζ = 0; tU_1/h_1 = 100; t/T = 1

Fig. 2-16. Flow visualization of the ratio between the velocity of continuous flow and the amplitude of velocity oscillation ζ= 0. The dimensionless frequency f* settled at 0.05. Photographs were taken at the frame rate of 960 Hz.

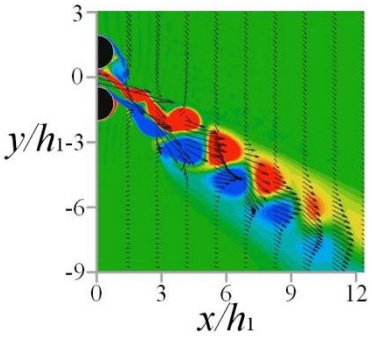

(i) $t/T = 0$

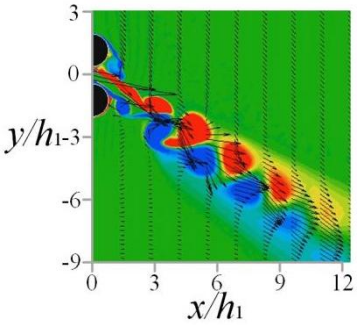

(ii) $t/T = 0.25$

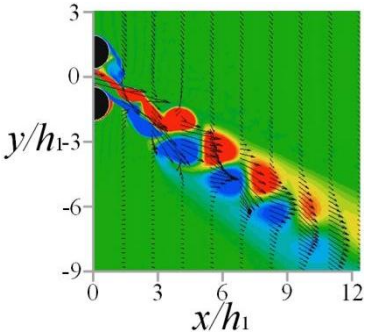

(iii) $t/T = 0.50$

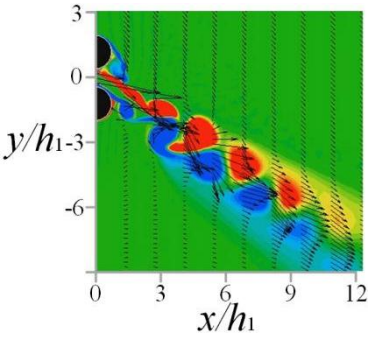

(iiii) $t/T = 0.75$

(a) $\zeta = -1$

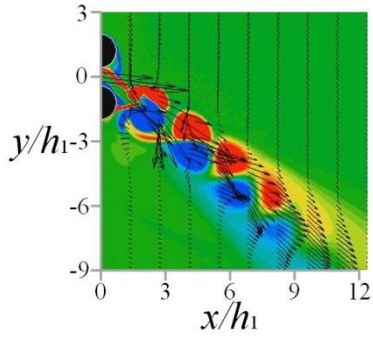

(i) $t/T = 0$

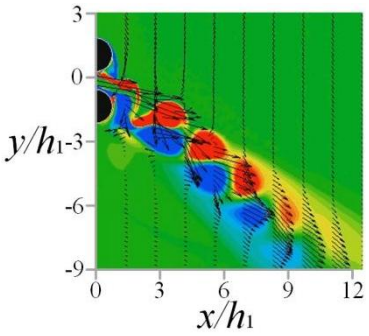

(ii) $t/T = 0.25$

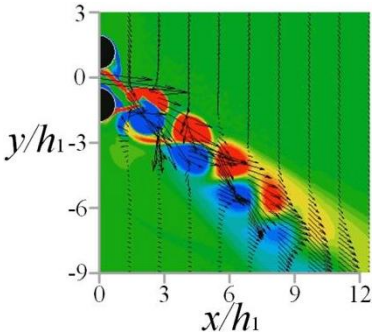

(iii) $t/T = 0.50$

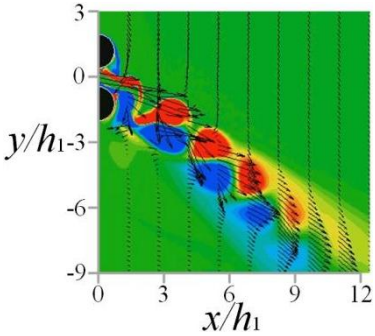

(iiii) $t/T = 0.75$

(b) $\zeta = 0$

Fig. 2-17. CFD result with the dimensionless frequency f^* set at 0.05.

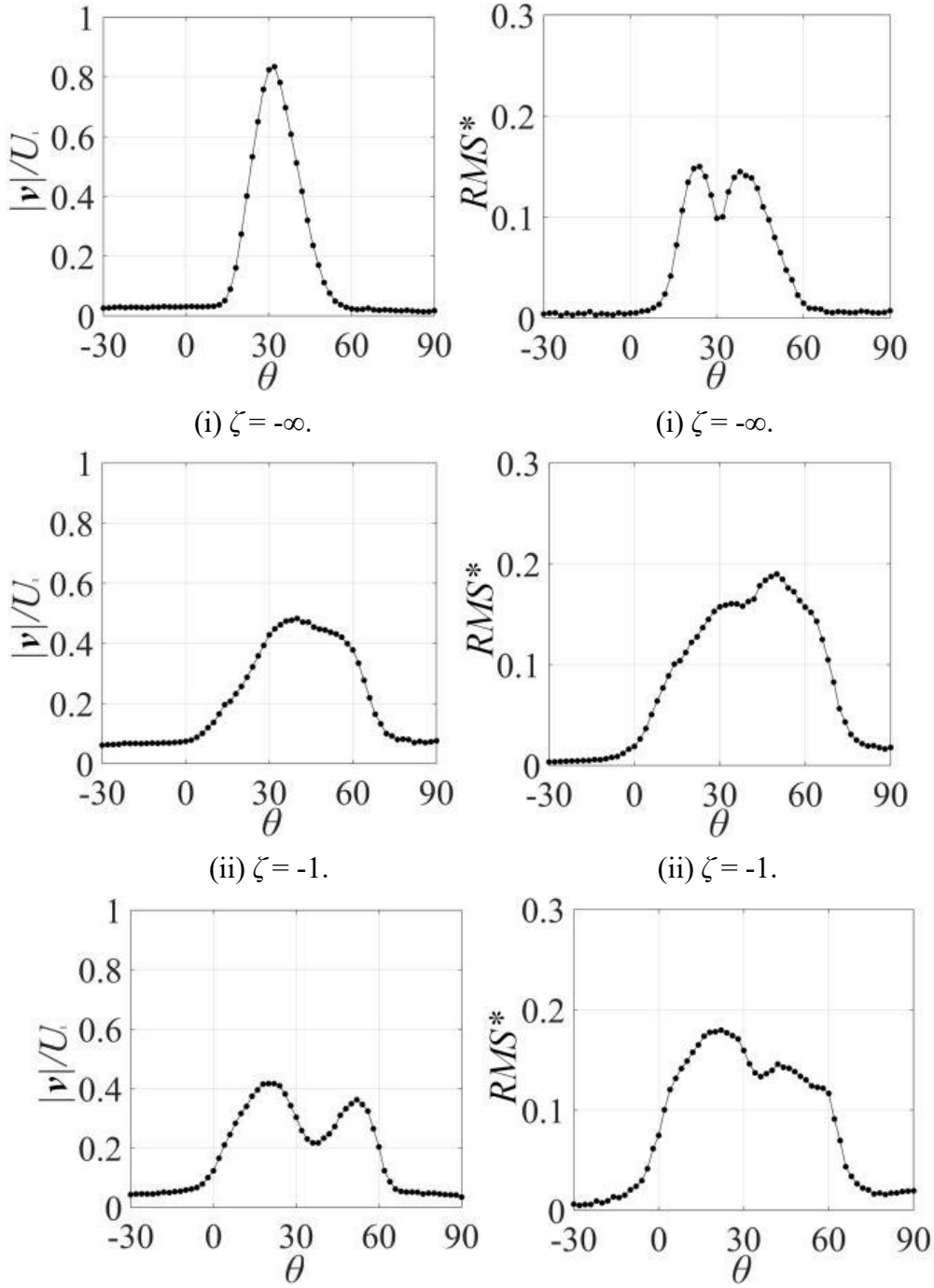

(i) $\zeta = -\infty$.

(i) $\zeta = -\infty$.

(ii) $\zeta = -1$.

(ii) $\zeta = -1$.

(iii) $\zeta = 0$.

(iii) $\zeta = 0$.

(a) Velocity distribution

(b) *RMS**

Fig. 2-18. Velocity distribution and *RMS** for the ratios between the velocity of continuous flow and the amplitude of velocity oscillation ζ= -∞, -1, and 0. The dimensionless frequency f^* settled at 0.05. The ratio of the momentum ξ settled at 0.08.

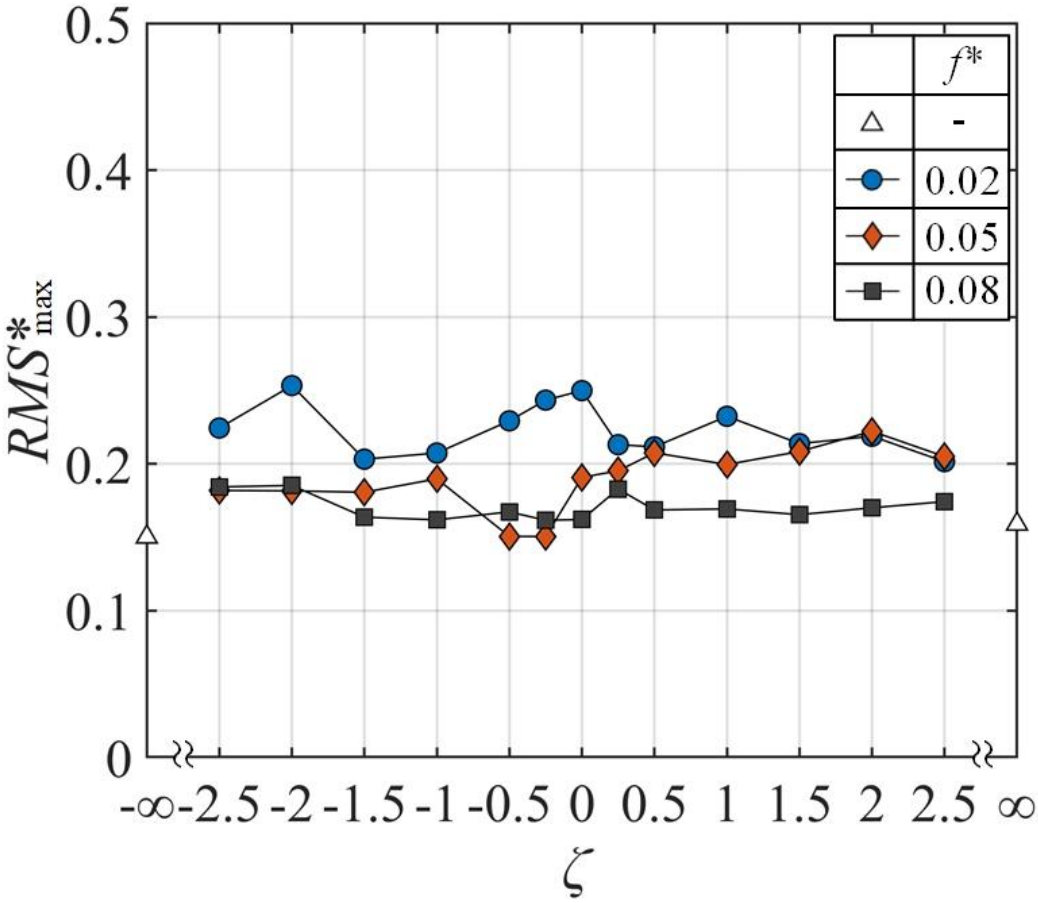

Fig. 2-19. RMS^*_{max} under various ratios between the velocity of continuous flow and the amplitude of velocity oscillation ζ and dimensionless frequencies f^*.

2.5 Summary

In this chapter, in order to control the direction of the primary jet without changing the geometry, we propose a new method of applying the excitation flow as a secondary flow near the surface of the Coanda surface. And the ratio of steady velocity to velocity fluctuation amplitude ζ is set as a new control parameter besides momentum ratio ξ, dimensionless frequency f^* to study the influence of different combinations of parameters on flow deflection characteristics. Based on the experiment results, it was found that it is possible to consider the unsteady characteristics of the flow while expanding the range of controllable deflection angles of flow. The conclusions are as follows.

1) The deflection angle of the jet was found to depend not only on the momentum ratio ξ and the dimensionless frequency f^*, but also on the ratio of the time-averaged velocity of the continuous flow to the time-varying velocity amplitude ζ.

2) By introducing a new parameter called ζ in addition to ξ and f^*, we succeeded in increasing the number of combinations of setting conditions for the realization of a controllable jet deflection angle. For example, it was found that even under constant conditions of ξ and f^*, a controllable deflection angle can be realized in the range of 0 to 40° by simply adjusting ζ. Furthermore, by introducing ζ, we were able to realize a larger jet deflection angle that could not be obtained by adjusting ξ and f^*.

3) It was suggested that this method can control not only the jet direction but also the jet half width and unsteady characteristics by combining the three parameters ξ, f^*, and ζ.

4) When the oscillating flow is applied to the secondary flow, a large-scale vortex similar to the reverse Karman vortex street is regularly emitted under oscillating secondary jet conditions.

5) RMS^*_{max} of the oscillating secondary flow is larger than that of the steady secondary flow; especially, as the dimensionless frequency decreases, the value of RMS^*_{max} slightly increases.

-Chapter 3-

Jet Flow Characteristics for Various Slot Widths and Frequency using Coanda Secondary Flows

3.1 Introduction

Fluidic thrust vector control utilizes flow control methods instead of mechanical deflection to achieve thrust deflection. However, this method is affected by more factors than traditional thrust vectoring, including shape parameters and fluid parameters. In Chapter 2, the excitation flow is used as a secondary flow to control the direction of the jet and a new parameter, the ratio of the time-averaged velocity of the continuous flow to the time-varying velocity amplitude ζ to achieve a larger deflection angle. In this chapter, the synthetic jet and the continuous flow were adopted as the secondary flow to mainly investigate the effect of shape parameter, specifically the ratio of cylinder radius to primary slot width on the deflection and structure characteristics. Besides the R/h_1, the synthetic frequency f,the dimensionless frequency f^* and momentum ratio ξ were also add to the experiments for analysis and comparison. The results demonstrate that the deflection ability of the secondary flow is dependent on the radius of the Coanda surface and the primary slot width ratio R/h_1. Moreover, the magnitude of the synthetic jet frequency has a significant effect on the flow pattern of the jet.

3.2 Nomenclature

f : Frequency of synthetic jet [Hz]

f^* : Dimensionless frequency [-]

h_1 : Primary slot width [m]

h_2 : Secondary slot width (2.0×10^{-3}) [m]

R_m : Measurement point radius ($=1.0\times10^{-1}$) [m]

Re : Reynolds number [-]

R : Radius of Coanda surface (1.5×10^{-3}) [m]

t : Time [s]

T : Period of velocity oscillation ($=1/f$) [s]

$b_{1/2}$: Half width of the jet flow[m]

U_A : Amplitude of velocity oscillation for secondary excited flow [m/s]

U_1 : Velocity of primary flow [m/s]

U_2 : Velocity of secondary flow [m/s]

U_{max} : Maximum velocity [m/s]

$|v|$: Absolute value of the velocity at an arbitrary point [m/s]

x,y,z : Coordinate axes [m]

x_c,y_c,z_c : Coordinate axes based on jet deflection center [m]

u : Velocity in x direction [m/s]

v : Velocity in y direction [m/s]

u_c : Velocity in x_c direction [m/s]

v_c : Velocity in y_c direction [m/s]

Greek symbols

θ : Clockwise Angle from x-axis[°]

θ_c : Deflection angle of jet [°]

θ_1 : Angle of the first point of intersection between $0.2U_{max}$ and velocity distribution [°]

θ_2 : Angle of the second point of intersection between $0.2U_{max}$ and velocity

distribution [°]

ξ : Ratio of momentum between primary flow and secondary flow [-]

v : Kinematic viscosity (1.506×10^{-5}) [m^2/s]

3.3 Experimental setup and method

The experimental setup in this chapter is similar to that in Chapter 2, but in this Chapter ,only the synthetic jet and the continuous flow were used as the secondary flow. So there is a difference in the method to generate the secondary flow. Figure 3-1(a) presents the schematic diagram of the experimental setup for the continuous flow as a secondary flow, and Figure 3-1(b) shows the schematic diagram of the experimental setup for the synthetic jet as a secondary flow. When the secondary flow is a continuous flow, the blower is directly connected to the secondary slot via a pipe.On the other hand, when the secondary flow is a synthetic jet, a speaker is connected to the secondary slot. The width of the primary slot can be adjusted by changing the baffle position on the upside of the primary slot.

In this chapter, the purpose is to investigate the deflection and unsteady characteristics of the primary jet under the influence of different primary slot widths. To accomplish this, we utilized two coordinates for the fluid velocity distribution measurement. In Figure3-2, the coordinates in Figure3-2(a) is the same as that of Chapter 2, including the measurement arc radius, measurement angle range and measurement point angle spacing. Figure 3-2(b) utilizes coordinates based on the jet deflection center. The origin of the coordinates z remains fixed at the intersection between the centreline of the primary slot and the tangent line of the cylinder. The x_c coordinates direction corresponds to the deflection centreline of the primary jet, while the y_c coordinates direction represents the vertical line of the centre of deflection. Due to the various widths of the primary slots used in this chapter, the measurement coordinates were dimensionless. This measurement method is used to analyse the structural characteristics of the fluid after the centre of deflection has been calculated.

The measurement equipment used for this chapter comprises a hot-wire anemometer and an I-type probe. The calibration method used is the same as in Chapter 2. For the equipment, one I-probe was connect to a traverser to measure of the velocity of the primary jet, the velocity of the secondary flow and the velocity distribution on coordinates. at the midpoint of the primary and secondary tank exit sections.And the measurement points for the primary jet and secondary flow are the midpoint of the primary and secondary slot exit respectively. For the

velocity distribution measurement of the first coordinates, the overall time-averaged velocity $|\boldsymbol{v}| = \sqrt{u^2 + v^2}$ over the circular arc which is consistent with the methodology presented in Chapter 2. For the velocity distribution measurement of the second coordinates, the I-probe was used to measure the flow velocity in the x_c direction u_c. Both measurement methods adopted the same sampling time of 14s and frequency of 10000Hz. Moreover, the calculation method of the deflection angle is almost the same as in Chapter 2, the only difference in this chapter is the part of the jet for $|v| > 0.15|U_1|$ is considered as a jet instead of $|v| > 0.2|U_{max}|$.

This chapter focuses on several experimental parameters, including the primary slot width h_1, the momentum ratio of the primary jet and secondary flow ξ, and the dimensionless frequency f^*. The definitions of the momentum ratio ξ and the dimensionless frequency f^* remain consistent with chapter 2. To explore the effect of slot width on the flow field, experiments were conducted using primary slot widths of 5, 10, 20, and 40 mm. And the radius of circular cylinder R were fixed at 2mm and 15mm respectively. Meanwhile, to maintain a constant momentum ratio ξ with various slot width h_1, the velocity of secondary flow was set as a constant for the simplicity of experiment. So in the experiment , the momentum ratio ξ can be adjusted just by changing the velocity of the primary jet. And for the same reasons as the Chapter 2, the range of the momentum ratio is $\xi = 0 \sim 0.08$, and the range of Reynolds number is $Re = 5.62\times10^3 \sim 1.59\times10^4$.

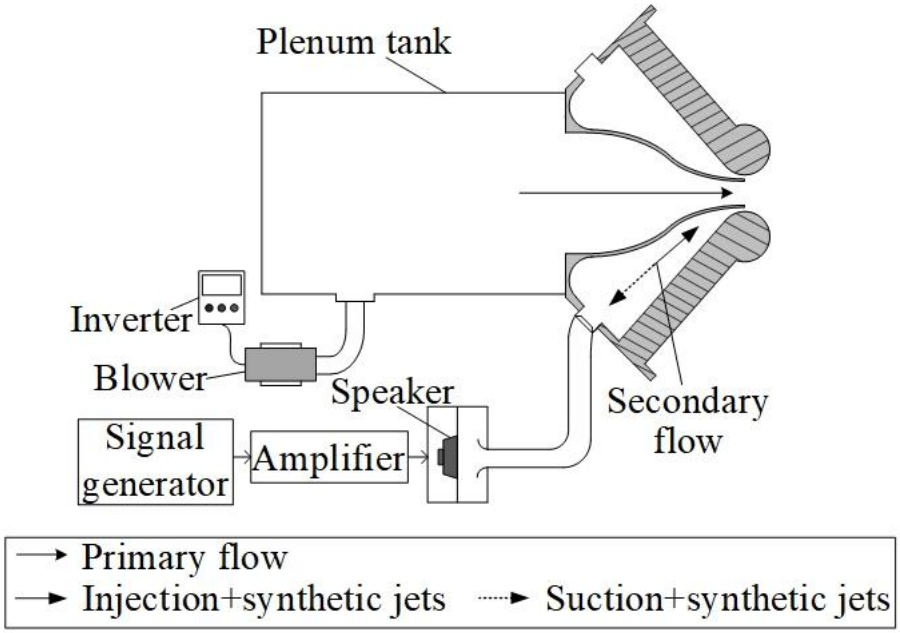

(a) Experiment apparatus for secondary continuous flow

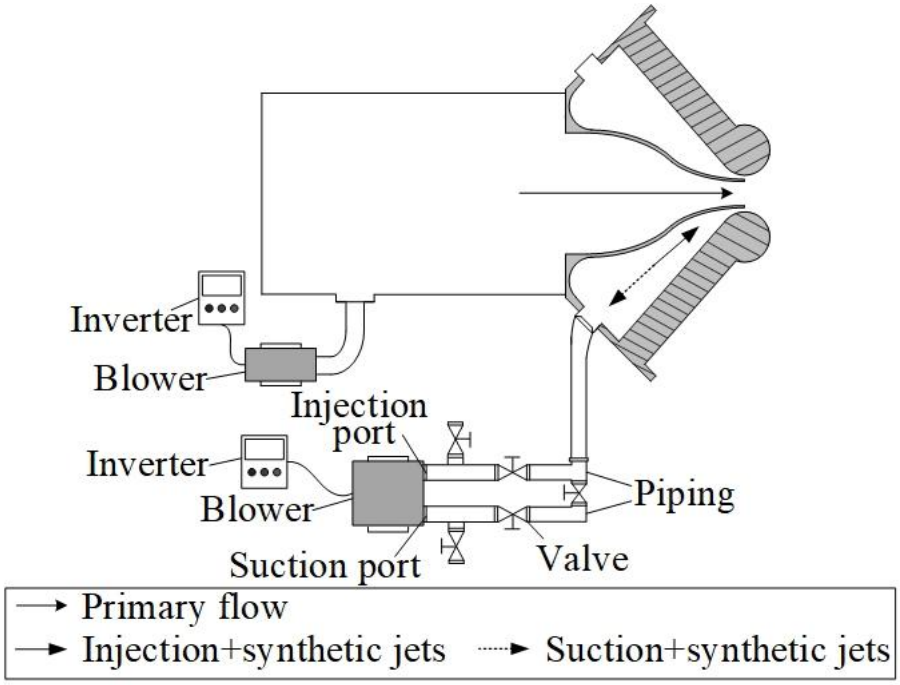

(b) Experiment apparatus for secondary synthetic jet

Fig. 3-1. Experiment apparatus.

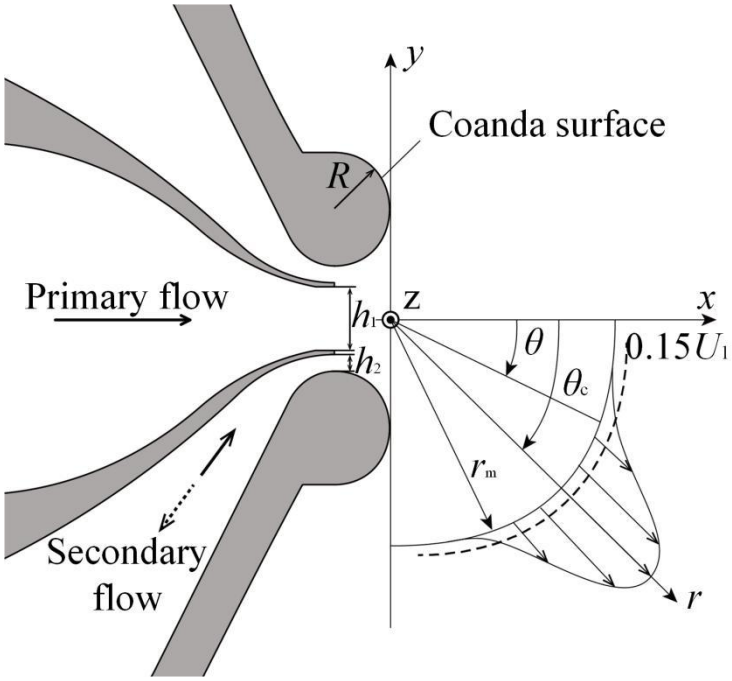

(a) Nominal coordinates based on the arc of r_m=100mm

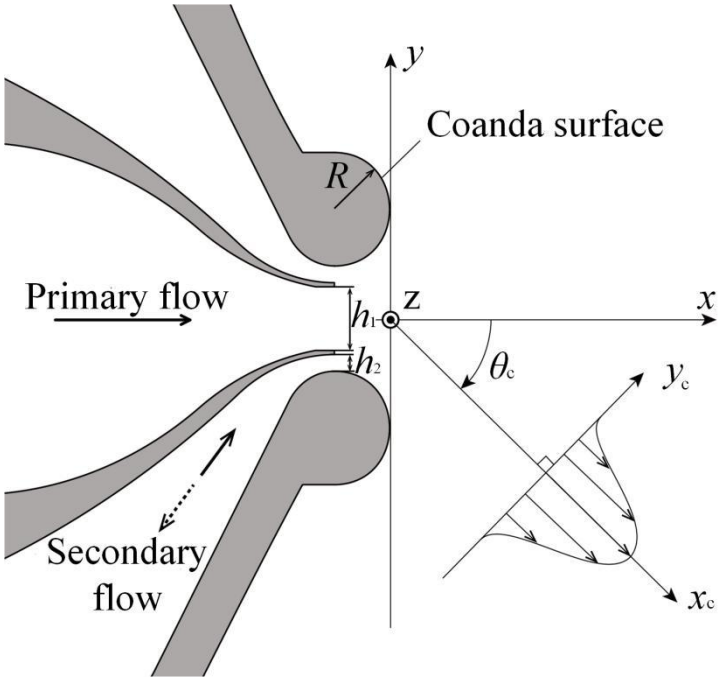

(b) Nominal coordinates based on the jet deflection center

Fig. 3-2. Schematic of slots and velocity distribution measurement method.

3.4 Results and Discussion

3.4.1 Influence of various R/h_1 on jet flow characteristic

Figure 3-3 shows the time average visualization results for various primary slot widths with dimensionless frequency f^* = 0.04 and momentum ratio ξ =0.06. The shape parameters R/h_1 for Figures 3-3(a), (b), (c) and (d) are R/h_1 = 3, 1.5, 0.75 and 0.375 respectively. For different synthetic frequency used in Figure3-3, all exposure times are longer than one cycle of corresponding synthetic jet .Therefore, in Figure 3-3(a), (b), (c) and (d) the frequencies of synthetic jet are f = 136, 48, 17 and 6Hz respectively, with corresponding exposure times of 1/130, 1/45, 1/15 and 1/6s. For R/h_1 = 3, the flow demonstrates the largest deflection angle among the tested conditions. With the decrease of R/h_1, the deflection angle gradually decreases. And for R/h_1 = 0.375, the deflection angle θ_c is almost 0. The deflection ability for the secondary synthetic jet depends on the the dimensionless f^* and momentum ratio ξ was confirmed in chapter two. However, according to the results of Figure3-3, with the same condition of f^* and ξ, the deflection angle is different with the changing of R/h_1. Therefore, It can be determined that the ratio of the cylinder radius to the width of the primary slot R/h_1 can effect the flow deflection characteristics while using the synthetic jet as a secondary flow.

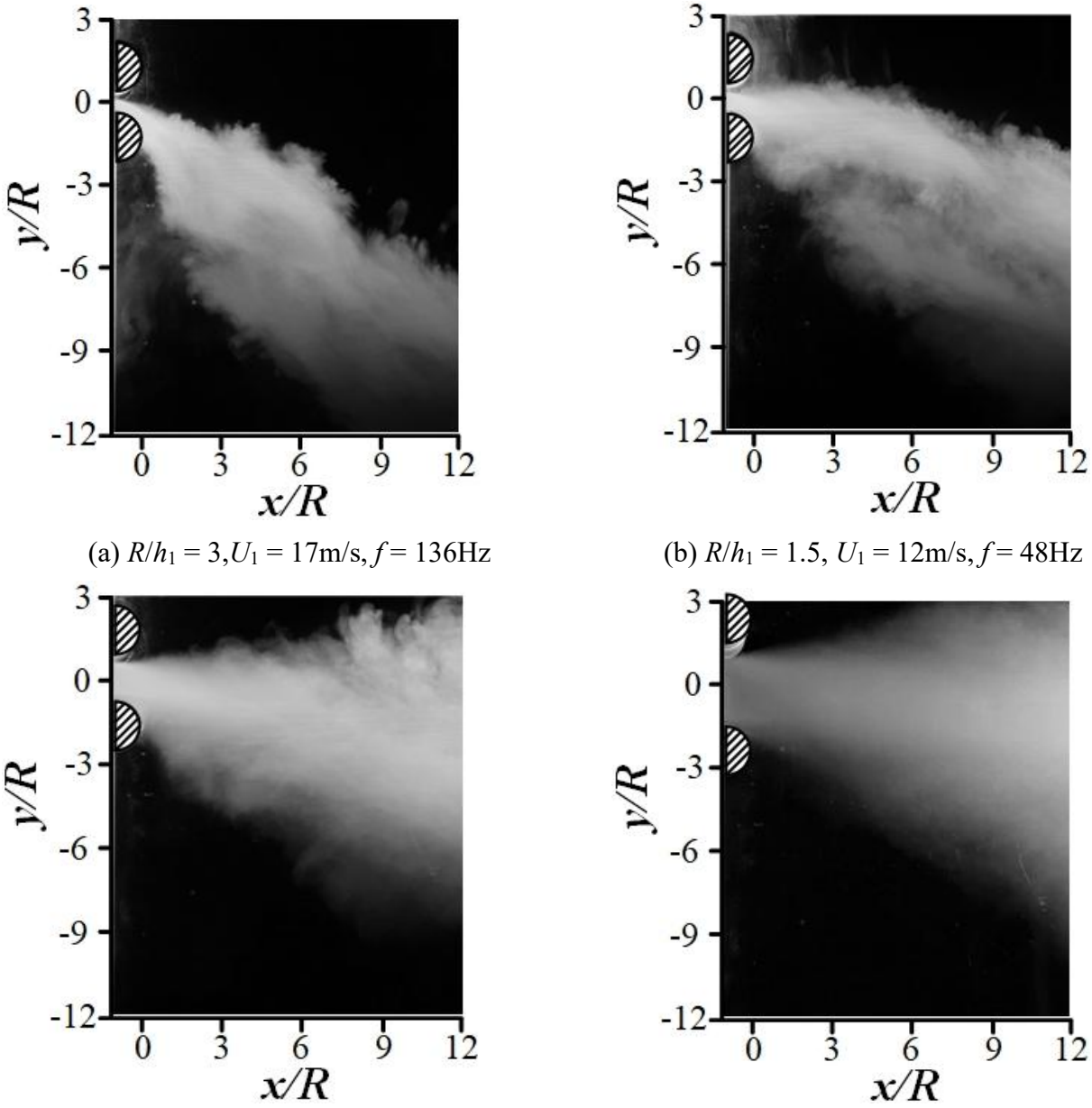

(a) $R/h_1 = 3, U_1 = 17$m/s, $f = 136$Hz

(b) $R/h_1 = 1.5$, $U_1 = 12$m/s, $f = 48$Hz

(c) $R/h_1 = 0.75$, $U_1 = 8.5$m/s, $f = 17$Hz

(d) $R/h_1 = 0.375$, $U_1 = 6$m/s, $f = 6$Hz

Fig. 3-3. Time-average Flow visualization for different R/h_1 with $f^* = 0.04$, $\xi = 0.06$; Shutter speed is set at 1/130s, 1/45s, 1/15s and 1/6s, respectively.

Next, the fluid properties for various synthetic jet frequencies under different primary jet slot widths were investigated . Besides the synthetic jet, the continuous suction flow and continuous injection jet were also used as secondary flow for comparison. Figures 3-4 shows the velocity distribution of the absolute value of the time average velocity on the arc with a radius of R_m=100mm under the momentum ratio ξ of 0.06 and various synthetic jet frequencies *f*. Specifically, Figures 3-4(a), (b), (c) and (d), correspond to the R/h_1 of 3, 1.5, 0.75 and 0.375 respectively. The horizontal axis represents the clockwise angle from *x*-axis θ , and the vertical axis represents the absolute value of the dimensionless time-averaged velocity $|v|/U_1$. For secondary continuous jet, it can be observed the deflection center of the velocity distribution is not influenced by R/h_1. For the secondary suction flow, the deflection center gradually moves to the right of the *x*-axis as R/h_1 increases while the jet width gradually becomes larger. And for the synthetic jet used as a secondary flow, the center of the time-averaged velocity distribution, the maximum velocity and the jet width are depend on the frequency values[24], which is corresponding to the results of Figure 3-4(a). For f = 10Hz, the jet width has the largest value while two peaks appear, for f = 100Hz the shape of the velocity distribution becomes approximately Gaussian and the deflection center and maximum deflection angle increase significantly. However, according to the results in Figure 3-4(d), the change of frequency *f* has a negligible effect on the velocity distribution which means that a larger value of R/h_1 results in a reduced effect of frequency *f* on the deflection ability of the synthetic jet. In addition, comparing R/h_1 = 0.375 to other conditions, the velocity distribution of the continuous suction flow and continuous jet are wider and similar to a shape of trapezoidal, which is because of the core region of the jet becoming wider as the width of the primary slot increase.

Figure 3-5 displays the relationship between the momentum ratio ξ and the deflection angle θ_c under various R/h_1 and frequency *f*. The horizontal axis corresponds to the momentum ratio ξ, and the vertical axis corresponds to the deflection angle θ_c. For R/h_1 = 0.375 and 0.75, the maximum deflection angle is less than 25°. And for the synthetic jet as a secondary flow, as the momentum ratio ξ increases, the deflection angle curve changes smoothly and it reaches the saturation zone at ξ = 0.03. Moreover, although the frequency *f* still has an effect on the

deflection angle, this effect is relatively small. For instance, in Figure3.5(c), the difference in deflection angle between f = 10 Hz and f = 100 Hz is less than 10°. For R/h_1 =3, the deflection angle of the synthetic jet with all frequency conditions are the largest among the four conditions of R/h_1, and the magnitude of the deflection angle depends on the frequency f. Although the deflection angle of the synthetic jet can reach a maximum of about 45° in this condition of R/h_1, the curve of the control field changes very steeply and even jump phenomenon occurs at certain frequency conditions. For instance, for f= 80 Hz, the deflection angle rises rapidly from the dead water zone (ξ = 0.02) to the saturation zone (ξ = 0.03). For R/h_1 =1.5, although the maximum deflection angle under the influence of the synthetic jet is about 36° which is small than that of R/h_1 =1.5, the curves of deflection angle change more smoothly and a wider controllable regions of $0.02 \leq \xi \leq 0.06$ for most frequencies. For the continuous suction flow as a secondary flow , maximum deflection angle at four conditions of R/h_1 are the larger than that of secondary synthetic jet. And the maximum deflection angle of secondary suction flow decreases as R/h_1 decreases. But with the increase of momentum ratio ξ, the jump phenomenon always occur. For the continuous jet as a secondary flow, the primary jet still have no deflection under any condition just like the Chapter 2. The reason is that the secondary continuous jet is more likely to separate from the Coanda surfaces with a small diameter and the use a Coanda surface with a larger diameter can overcome the dead zone. In summary, for the synthetic jet as a secondary flow, the deflection angle not only depends on the momentum ratio ξ, the frequency f and the dimensionless frequency f^*, but also depends on the size of R/h_1 . Although the larger the R/h_1 the larger the maximum deflection angle will be, but there will be a loss of the control area.

Figure 3-6 illustrate the relationship between R/h_1 and the deflection angle θ_c for various momentum ratios under the dimensionless frequency of f^* = 0.04. The horizontal axis represents the ratio of the cylinder radius to the width of the primary slot R/h_1, and the vertical axis represents the deflection angle θ_c. For a momentum ratio ξ of 0.01, no deflection occurs in the primary jet flow for any of the R/h_1, as the momentum ratio ξ is too small to overcome the ‘dead water’ region. As the momentum ratio ξ increase to 0.02, the deflection angles for low value of R/h_1 = 0.375 and 0.75 are already close to their saturation zones. And for high

value of R/h_1 = 2 and 3, the deflection angle curves jump to the saturation zone at ξ of 0.03 immediately after overcoming the dead water zone at ξ of 0.02. Only for R/h_1 of 1.5, the deflection angle curve increases smoothly as the momentum ratio ξ increases in the controllable region of $0.02 \leq \xi \leq 0.06$. In summary, the larger the R/h_1, the larger the maximum deflection angle. For instance, R/h_1 of 1.5 and 3 result in maximum deflection angle of 35° and 55°, indicating a difference of 20°. Therefore, it is important to choose the suitable ratio of cylinder radius to width of primary slot in practice. A small R/h_1 may result in insufficient deflection ability, while a large R/h_1 may sacrifice the advantage of a smooth, controllable curve for a larger deflection angle. It is noteworthy that the maximum deflection angle of the secondary synthetic jet is always lower than that of the secondary suction flow.

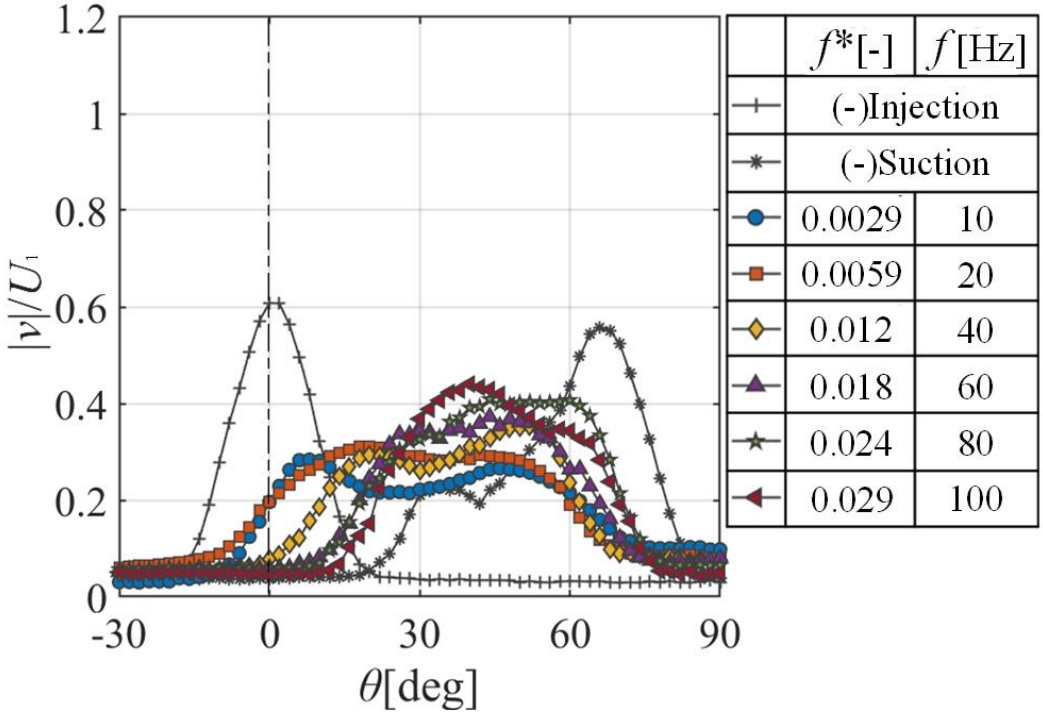

(a) Velocity distribution for $R/h_1 = 3$(h_1 = 5mm,U_1 = 17m/s)

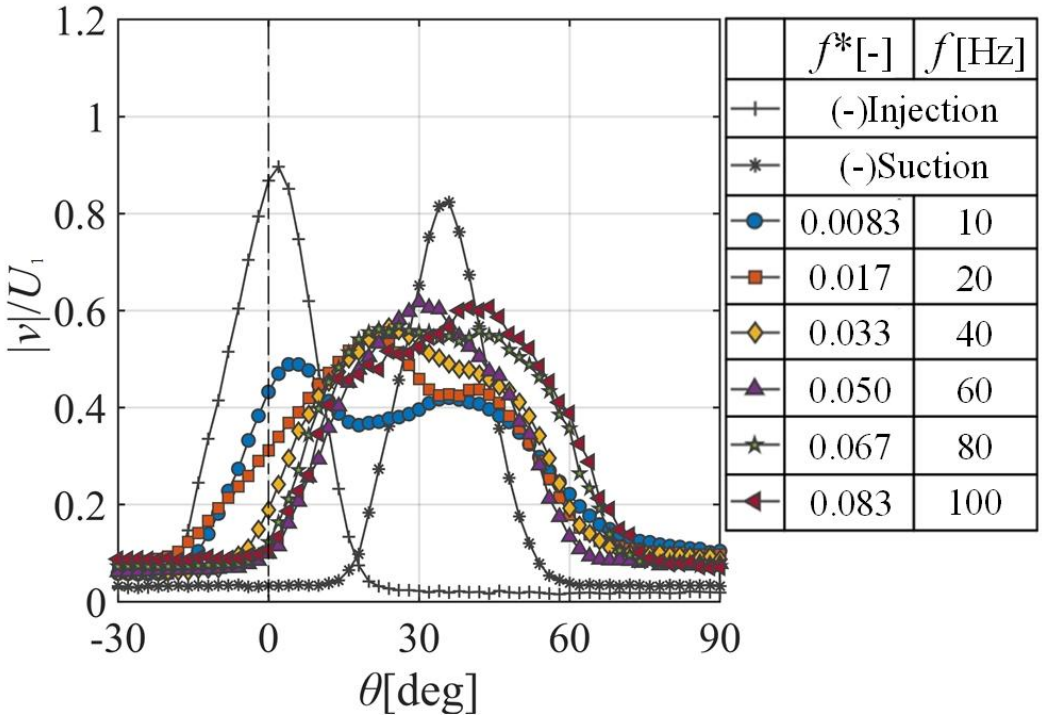

(b) Velocity distribution for $R/h_1 = 1.5$ (h_1 = 10mm,U_1 = 12m/s)

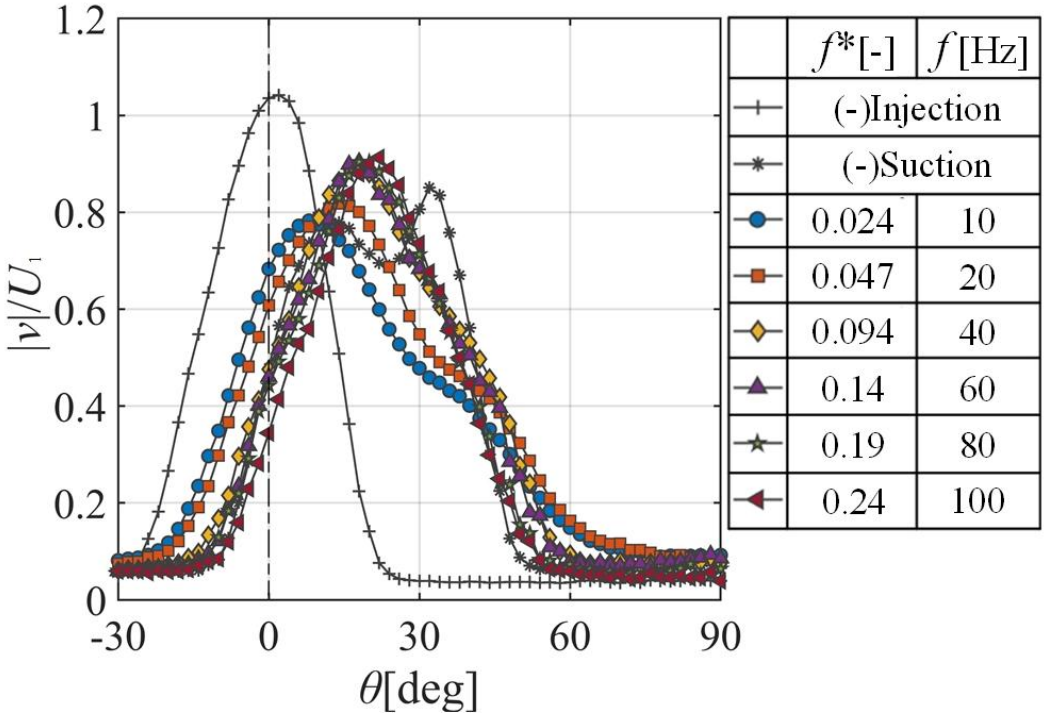

(c) Velocity distribution for $R/h_1 = 0.75$ ($h_1 = 20$mm,$U_1 = 8.5$m/s)

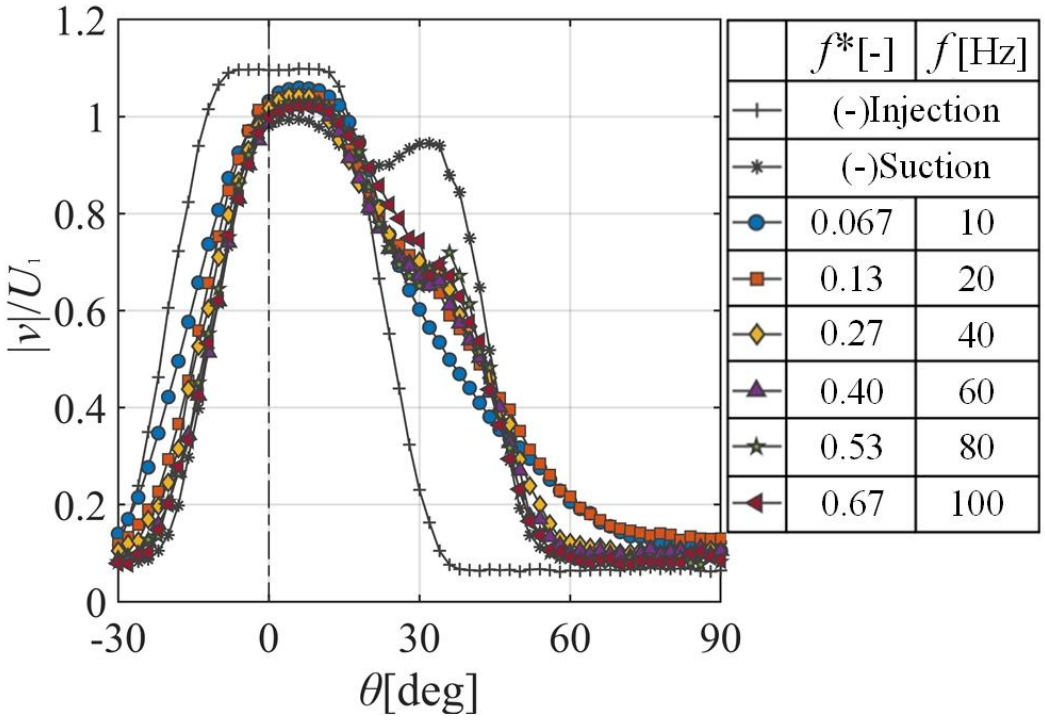

(d) Velocity distribution for $R/h_1 = 0.375$ ($h_1 = 40$mm,$U_1 = 6$m/s)

Fig. 3-4. Flow patterns of jets under condition of secondary synthetic jet with $\xi = 0.06$ ($h_2 = 2$mm,$R = 15$mm,$U_2 = 6.6$m/s,$U_A = 9.3$).

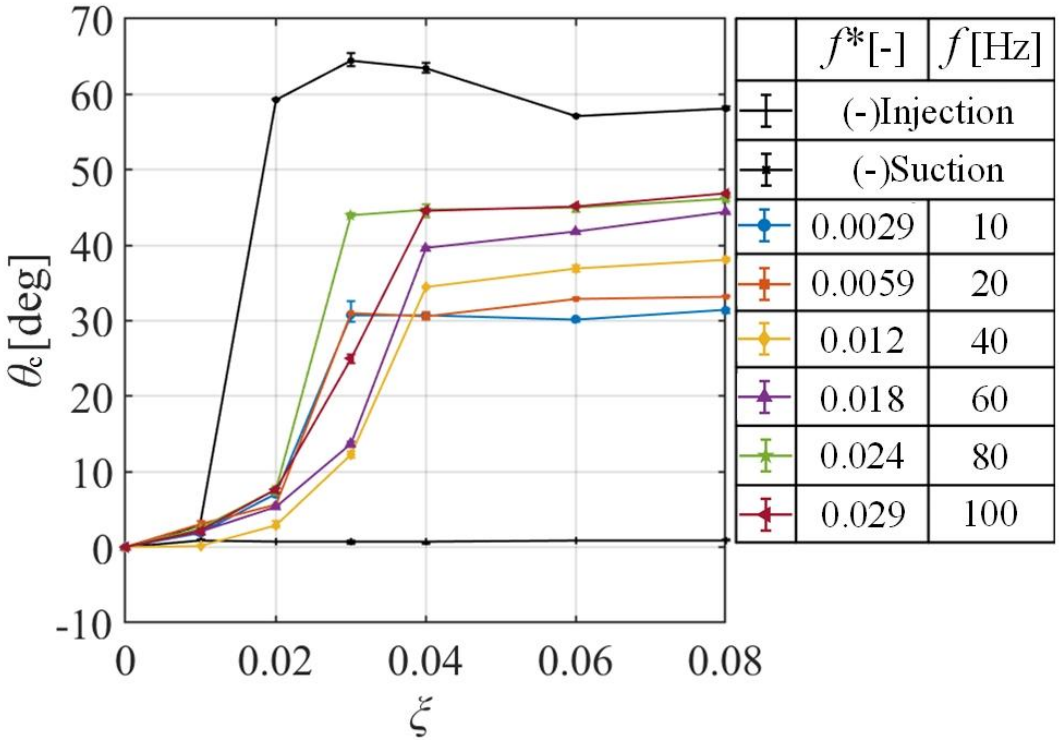

(a) Deflection angle for $R/h_1 = 3$ under different ξ

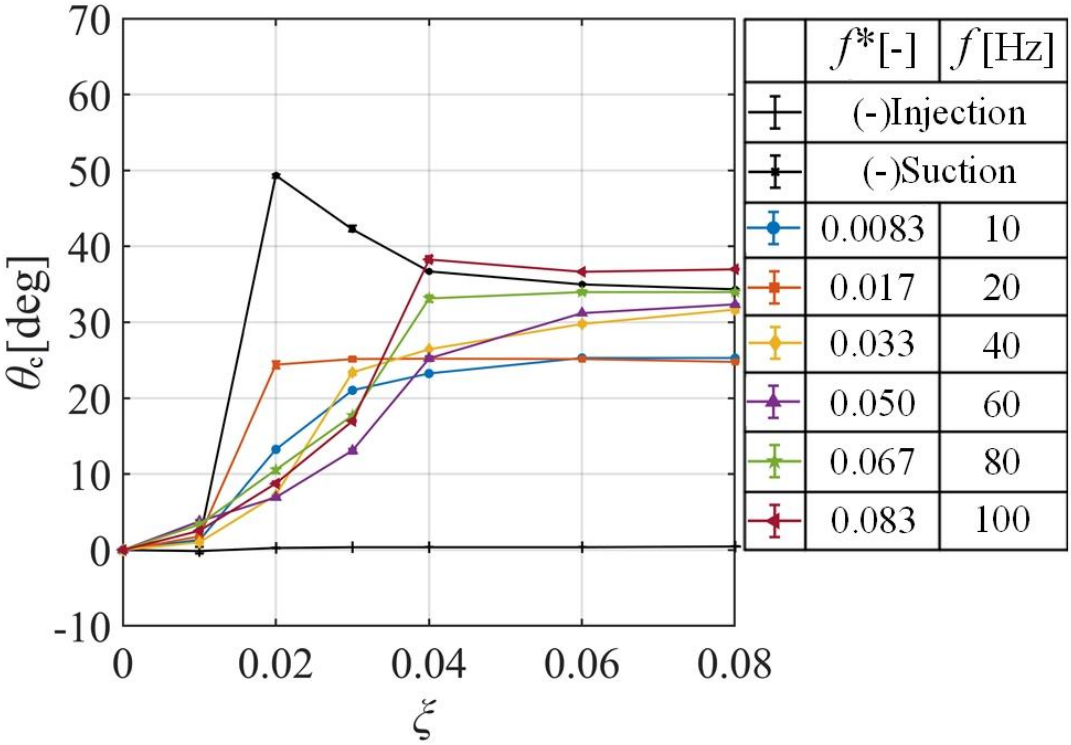

(b) Deflection angle for $R/h_1 = 1.5$ under different ξ

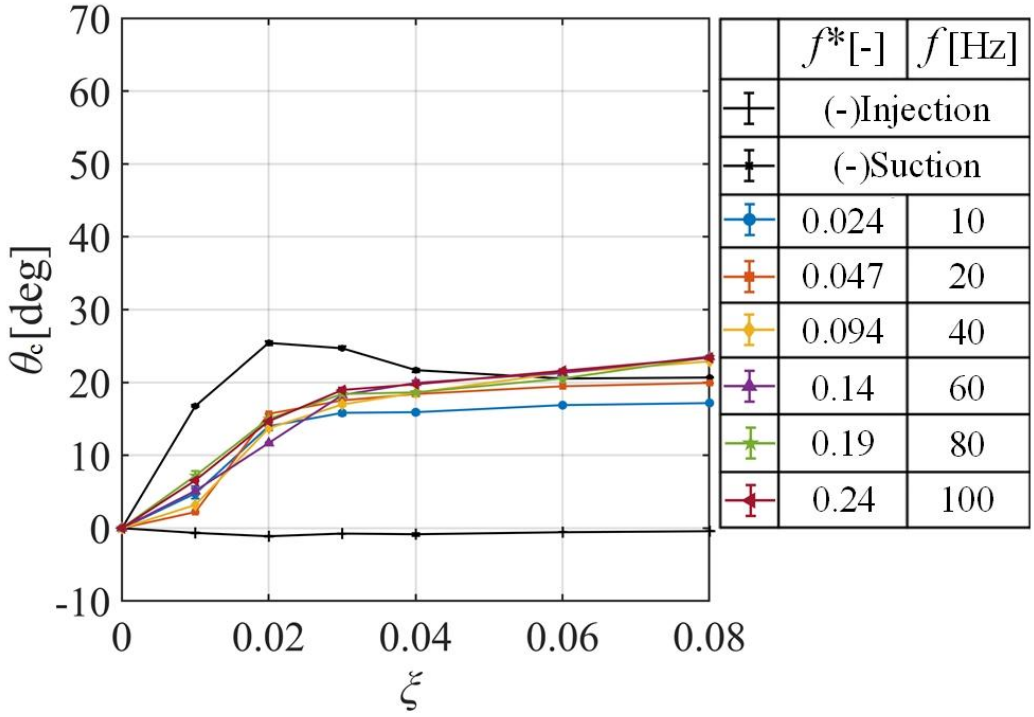

(c) Deflection angle for $R/h_1 = 0.75$ under different ξ

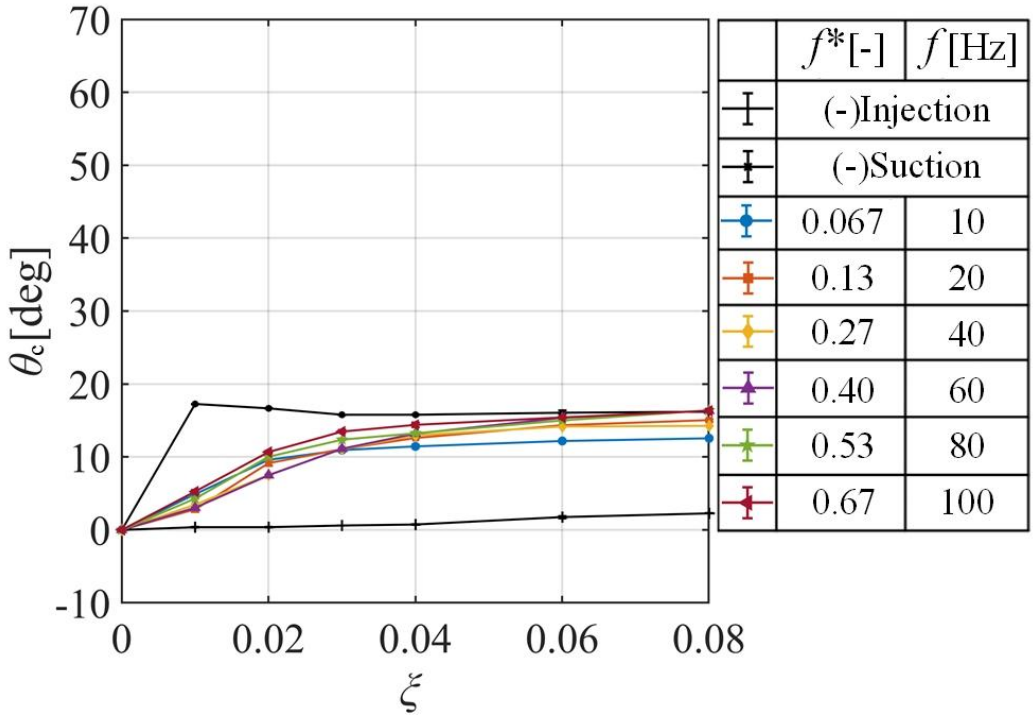

(d) Deflection angle for $R/h_1 = 0.375$ under different ξ

Fig. 3-5. Relation between the ratio of momentum ξ between primary flow and secondary flow and deflection angle θ_c for various frequency and slot width ratio (h_2 = 2mm,R = 15mm).

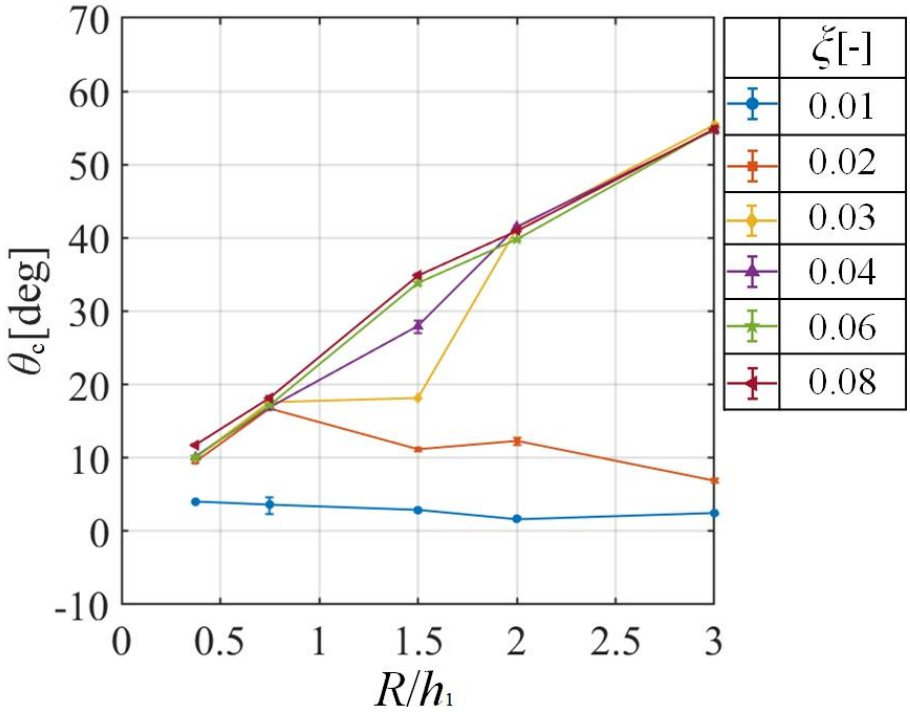

Fig. 3-6. Relation between the slot width ratio R/h_1 and deflection angle θ_c for various ratio of momentum ξ.

Figure 3-7 depicts the spectral analysis for ratio of cylinder radius and width of primary slot $R/h_1 = 3$ and $R/h_1 = 0.75$. The horizontal axis represents the dimensionless frequency f^* and the vertical axis represents the dimensionless spectral density. Figures 3-7(a) and Figures3-7(b) correspond to the visual observation of Figures 3-3(a) and Figures3-3(c), the dimensionless frequency and momentum ratio were set at $f^* = 0.04$ and $\xi = 0.06$. As the deflection angles for the Figure 3-7 have been calculated, the coordinate shown in Figure 3-2(b) was used as a measurement coordinate. The measurement area is defined by $x_c/h_1 = 6$, with $-6 \leq y_c/h_1 \leq 6$mm, and the measurement interval in the y_c direction is $\Delta y_c/h_1 = 0.5$. The obtained results indicate the difference in the maximum dimensionless amplitude between Figures 3-7 (a) and (b) is below 5%. Both figures exhibit two peaks in the y_c direction, attributed to the inverse Karman vortex generated by the secondary synthetic jet. Notably, the interval between the two peaks of $R/h_1 = 3$ is wider compared to that of $R/h_1 = 0.75$. This observation could be attributed to the effect of the synthetic frequency f on the flow pattern, which will be investigated in the subsequent section. With the conditions of Figure3-7(a), it is apparent that the range of velocity oscillation is $-4.5 \leq y_c/h_1 \leq 3$, provided that any dimensionless velocity fluctuation amplitude below 0.05 is ignored. On the other hand, with the conditions of Figure3-7(b), the range of velocity oscillation is $-3.5 \leq y_c/h_1 \leq 3.5$. The dimensionless distances in the y_c direction are 7.5 and 7 which are very close. Therefore, it can be concluded that although the R/h_1 is different, the structure of the flow is similar under the same condition of dimensionless frequency f^* and momentum radio ξ.

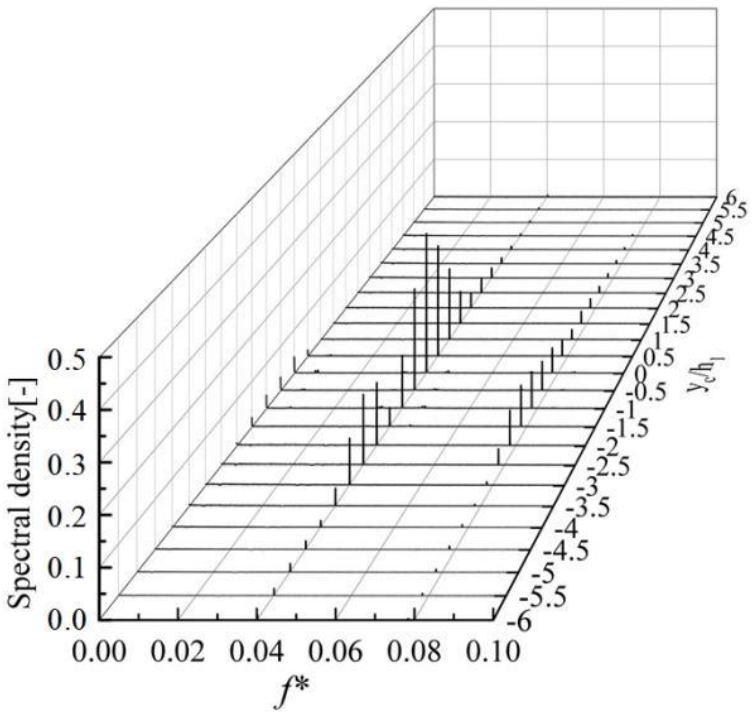

(a) $R/h_1 = 3, U_1 = 17\text{m/s}, f = 136\text{Hz}, \theta_c = 50^\circ$

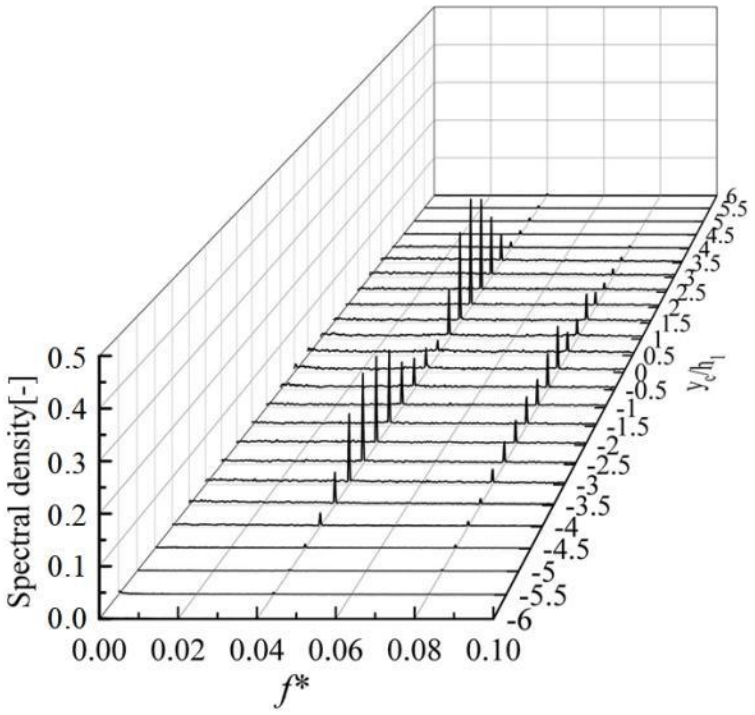

(b) $R/h_1 = 0.75$, $U_1 = 8.5\text{m/s}$, $f = 17\text{Hz}$, $\theta_c = 18^\circ$

Fig. 3-7. Comparison of Spectrum of fluctuations for different R/h_1 when $x_c/h_1 = 6$, $\xi = 0.06$ and f^*=0.04.

3.4.2 Effect of various *f* on jet flow unsteady characteristic

This section aims to investigate the effect of the synthetic jet frequency *f* on the unsteady characteristics of the jet. To exclude the influence of the momentum ratio ξ, the momentum ratio ξ was kept constant at ξ = 0.06 throughout the experiment. This decision was based on the result that the deflection angle generally reaches the saturation zone for the momentum ratio ξ = 0.06. In addition, the ratio of cylinder radius to primary slot width was set to R/h_1=3 which has the best deflection performance.

Next, visualization observations and spectral analysis were conducted for high frequency *f* of 100Hz and low frequency *f* of 10Hz. Besides that the secondary suction flow was also conducted the same experiments for comparison. Figures 3-8(a) and (b) show visualized observations and spectral analysis for the suction flow as a secondary flow under ξ = 0.06. Figure 3-9 and Figure 3-10 show time-step visualized observations for frequency *f* of 10 Hz and 100 Hz with a camera exposure time of 1/960s. And panel(a)~(b) depict the different t/T of a secondary flow. Figure 3-11(a), (b) shows the results of spectral analysis for frequency *f* of 10 Hz and 100 Hz ,and their measurement coordinates are corresponding to Figure 3-7.

In Figures 3-8, it is apparent that the primary flow attaching to the Coanda surface and deflected with a large deflection angle under the secondary suction flow. And no vortices is produced in this visualization observation which is consistent with Figure 3-8(b). For Figure 3-9(a)(t/T = 0), the jet near the exit of the primary slot is slightly deflected downwards. And a vortex is generated at the lower part of the jet due to the fact that that t/T = 0 is following the suction process of the synthetic jet. At t/T =0.25 and 0.5, the primary jet go straight ahead due to being the injection process of the synthetic jet. And at t/T =0.75, the secondary synthetic jet exhibits the maximum suction in one cycle. The flow pattern indicates that the jet near the primary slot flows along the Coanda surface until it reaches the separation point. Additionally, the upper part of the jet generate another vortex opposite to the previous one due to the shear layer. From Figures 3-10, it is evident that the primary jet remains attached to the cylinder surface due to the Coanda effect at all times. However, the position of the separation point of the primary jet on the cylinder surface depend on the velocity position in one circle of the

synthetic jet. For example, at t/T=0.5, the synthetic jet is at the end of the injection process, so the separation point is the closest. And at t/T=0(t/T=1), the synthetic jet is at the end of the suction process, so the the separation point is the furthest. Meanwhile, the downstream of the primary jet generate an inverse Karmen vortex street which has a closer distances between vortices pairs and smaller sizes of vortices compared to Figure 3-9. Comparing Figure 3-9 with Figure 3-10, the primary jet under low frequency(10Hz) has a clear 'switching phenomenon' that the primary jet be attracted to the cylindrical surface from the situation of moves forward. For the synthetic jet with a high frequency, the 'switching phenomenon' completely disappears and the primary jet remains attaching to the cylinder surface due to inertia. So even though there is no significant difference in the maximum separation points between the two situation , there is a difference of deflection angle about 12°.

Comparing Figure 3-11(a) with (b), it is apparent that the maximum amplitude of the dimensionless velocity fluctuation is about 0.4 under f = 10Hz. The boundary of velocity fluctuation in the positive direction of y_c/h_1 is 4.5 and the boundary in the negative direction is less than -6. On the other hand, the maximum amplitude of the dimensionless velocity fluctuation is approximately 0.25 under f = 100Hz which is 60% of that under f = 10Hz. The boundary of velocity fluctuation in the positive direction of y_c/h_1 is 2.5 and the boundary in the negative direction is -3.5 which is narrower. Furthermore, for f=10Hz, two peaks appear in the y_c/h_1 direction, which is similar to Figure 3-7. The outcomes presented in Figure 3-9 indicate that this occurrence is due to the extended spacing between the vortices, which arises as a consequence of the 'switching phenomenon' associated with low-frequency synthetic jets. For f=100Hz, The maximum value of the dimensionless velocity fluctuation amplitude is at y_c/h_1=0. It is because the primary jet remains attaching to the Coanda surface leads to a closer distance between the vortices. In summary, the structure of the primary jet is influenced by both dimensionless frequency f^* and frequency f. The difference between high and low frequency will result in a significant difference in flow pattern. Although the maximum separation point is similarly located between these two conditions, a significant difference in the deflection angle. The primary flow under frequency of f = 100Hz has a higher quality and a greater deflection angle.

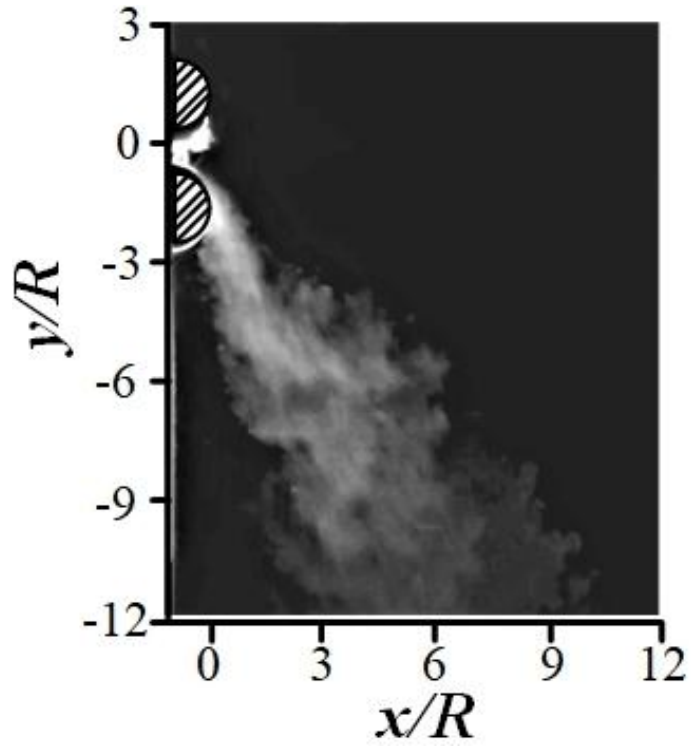

(a) Visualized observations for frame per second of 960Hz

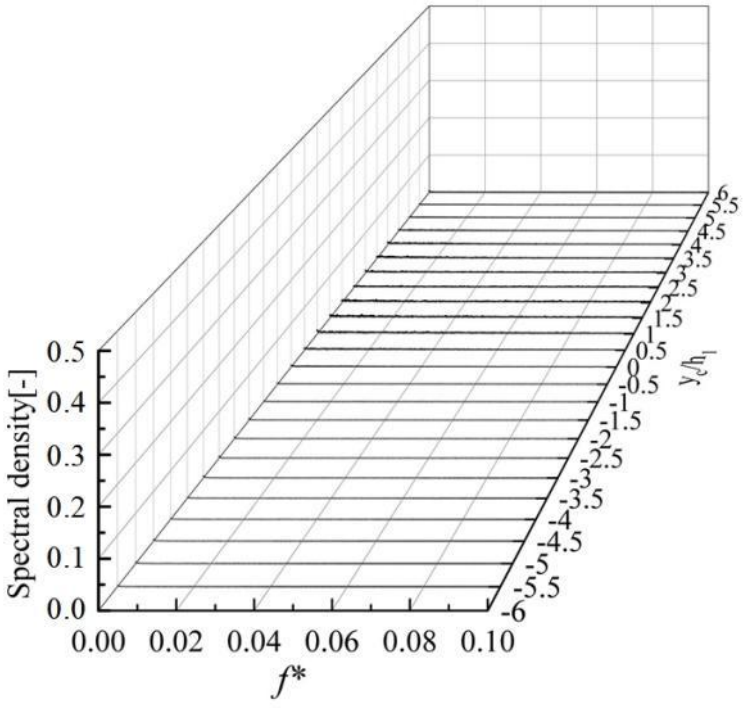

(b) Spectrum of fluctuations for $x_c/h_1 = 6$

Fig. 3-8. Visualized observations and spectrum of fluctuations for suction flow as a secondary flow under the conditions of ξ=0.06 and $R/h_1 = 3$.

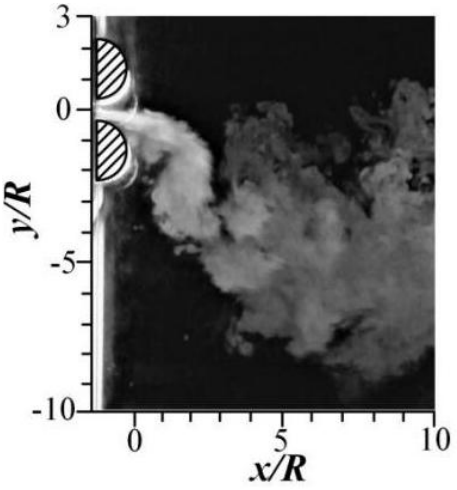

(a) $t/T = 0$

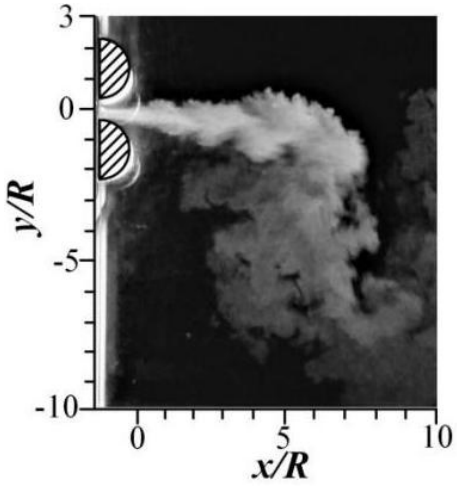

(b) $t/T = 0.25$

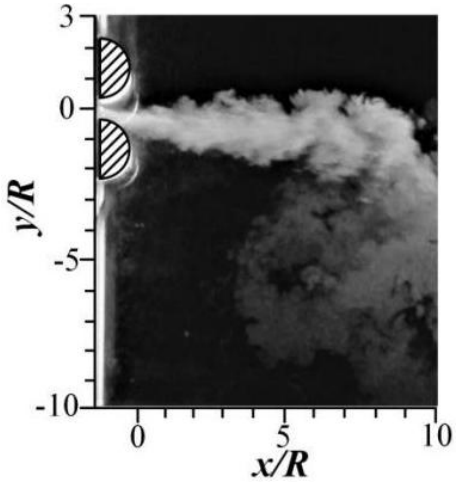

(c) $t/T = 0.5$

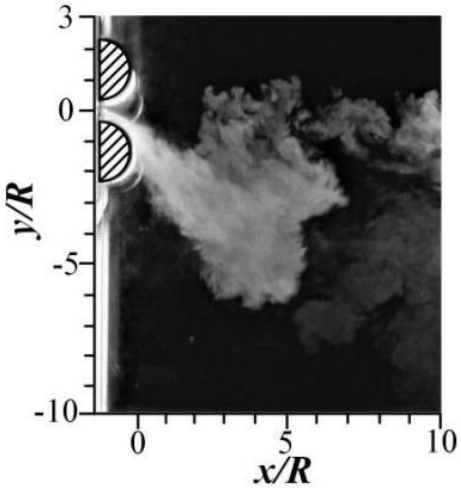

(d) $t/T = 0.75$

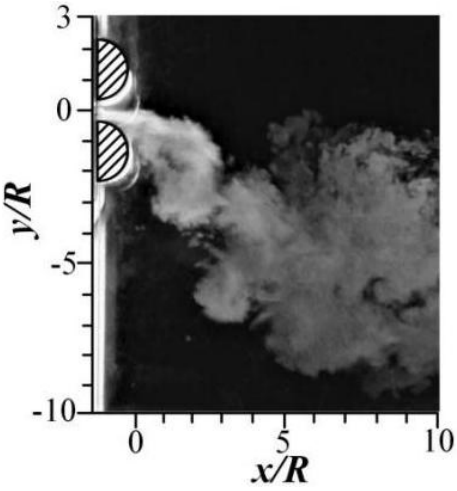

(e) $t/T = 1$

Fig. 3-9. Time-step visualized observations for synthetic jet as secondary flow under the conditions of $R/h_1 = 3$, $f^* = 0.0029$, $f = 10$Hz and $\xi = 0.06$; Frame per second is set at 960Hz.

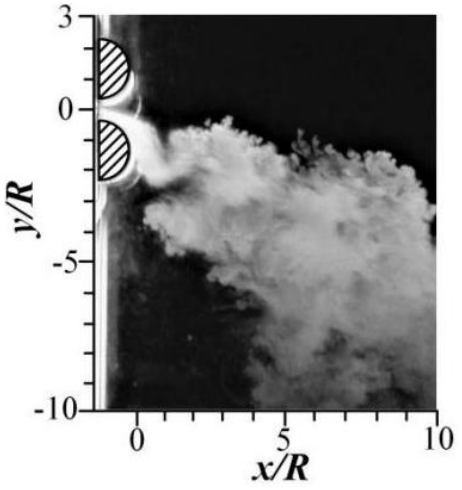

(a) $t/T = 0$

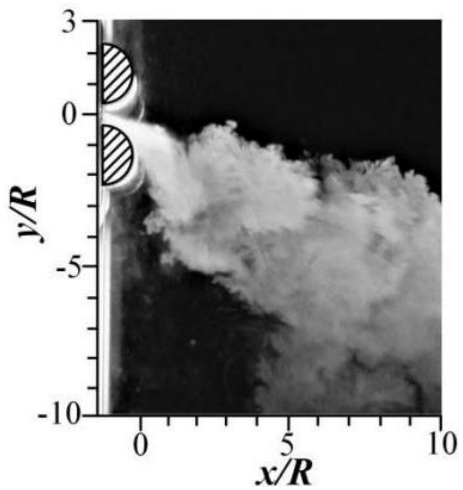

(b) $t/T = 0.25$

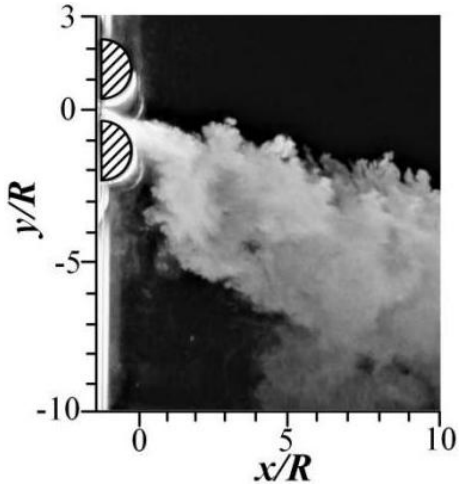

(c) $t/T = 0.5$

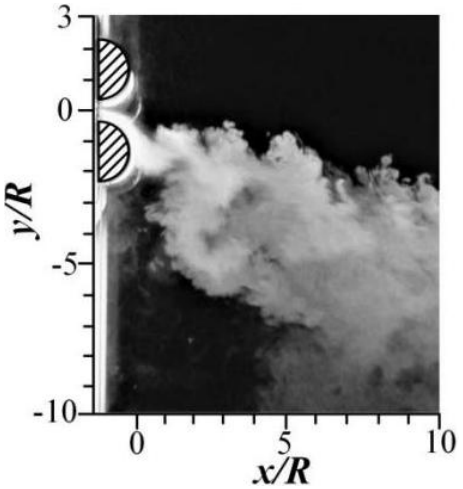

(d) $t/T = 0.75$

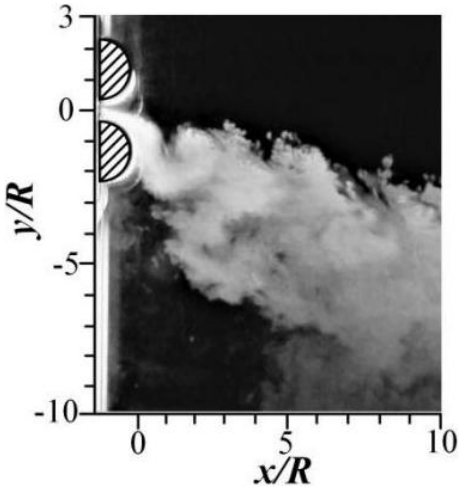

(e) $t/T = 1$

Fig. 3-10. Time-step visualized observations for synthetic jet as secondary flow under the conditions of R/h_1=3, f^*=0.029, f=100Hz and ξ=0.06; Frame per second is set at 960Hz.

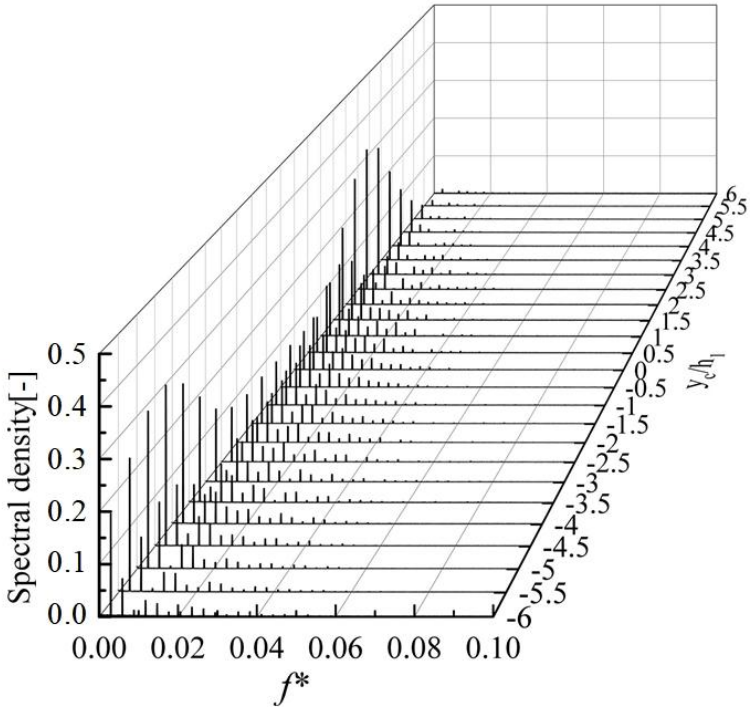

(a) f = 10Hz; f^* = 0.0029; θ_c = 30°

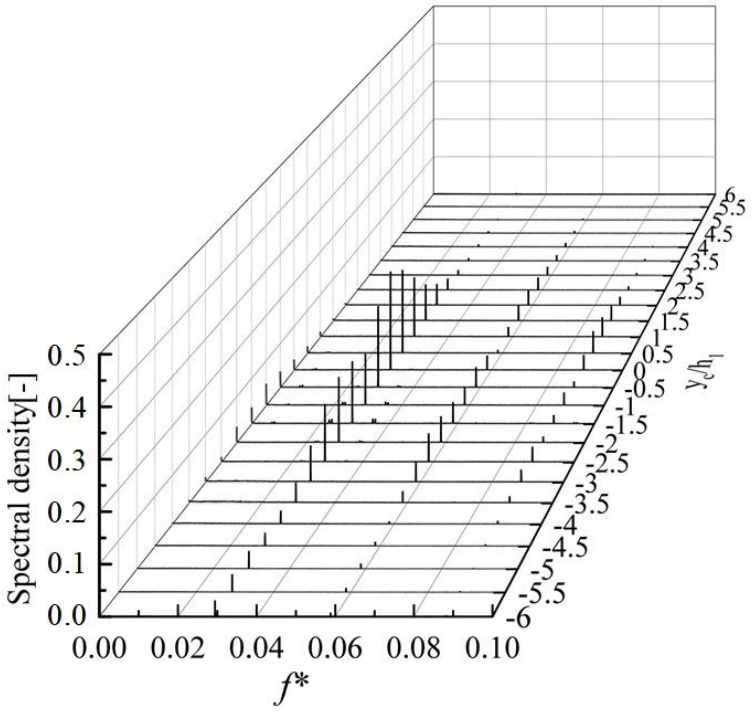

(b) f = 100Hz; f^* = 0.029; θ_c = 44°

Fig. 3-11. Comparison of Spectrum of fluctuations for different f^* when x_c/h_1 = 6, ξ = 0.06 and R/h_1 =3.

Figure 3-12 shows the velocity distribution of the primary jet under the influence of the secondary continuous flow and the secondary synthetic jet for ξ = 0.06 and R/h_1 = 3. This experiment used the measurement coordinate system based on the deflection center and the hot wire was used to measure the velocity in the x_c direction u_c. The measurement area is x_c/h_1 = 6, 9 and 12, $-6 \le y_c/h_1 \le 6$mm, and the measurement interval in the y_c direction is $\Delta y_c/h_1$ =0.2. Figure 3-12(a) and Figure 3-12(b) present the flow structure for the secondary injection flow and the continuous suction flow respectively. Both velocity distribution shapes are similar to a Gaussian distribution and the maximum velocity is around y_c/h_1 = 0. As the x_c/h_1 increases, the value of the maximum velocity decreases and the half width of jet increases. But the velocity attenuation and increase of half width is more pronounced for the secondary suction flow. Figure 3-12(c) and Figure 3-12(d) depict the flow structure for the secondary synthetic jet with frequency of 10Hz and 100Hz respectively. For f=10Hz, the velocity attenuation is pronounce that the maximum dimensionless velocity is about 0.4 at x_c/h_1 = 6. And velocity hollow exist due to the 'switching phenomenon'. For f=100Hz, no velocity hollow exist in the velocity distribution and the velocity attenuation is weaker than that of f=10Hz. And the half width of jet is narrower than f=10Hz, but wider than that of continuous flow.

Figure 3-13 demonstrates a comparison of the half width values $b_{1/2}$ of the primary jet under the condition of R/h_1 = 3, ξ = 0.06. The horizontal axis represents the dimensionless coordinate x_c/h_1 and the vertical axis shows the dimensionless half-width $b_{1/2}/h_1$. The dimensionless half width of the continuous flow is always lower than that of the synthetic jet at any frequency condition. For instance, the dimensionless half width of the continuous suction flow at any x_c/h_1 coordinate is lower than 50% of the the dimensionless half width of the synthetic jet for f = 100 Hz. Comparing the the dimensionless half width $b_{1/2}/h_1$ between secondary synthetic jets with different frequencies, it can be determined that the dimensionless half width depends on the frequency of the synthetic jet and the dimensionless half width becomes larger as the frequency decreases at any x_c/h_1 except few cases. For example, comparing the high frequency of f=100Hz with the low frequency of f=10Hz, the difference of the dimensionless half-width is approximately 25mm for x_c/h_1 = 6, and approximately 36mm for x_c/h_1 = 12.

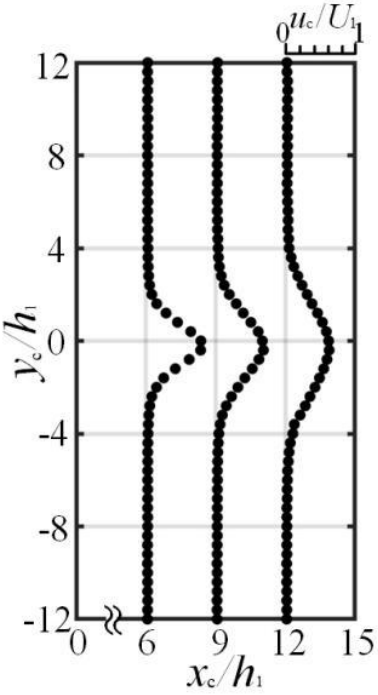

(a) Injection jet; θ_c = 0.82˚

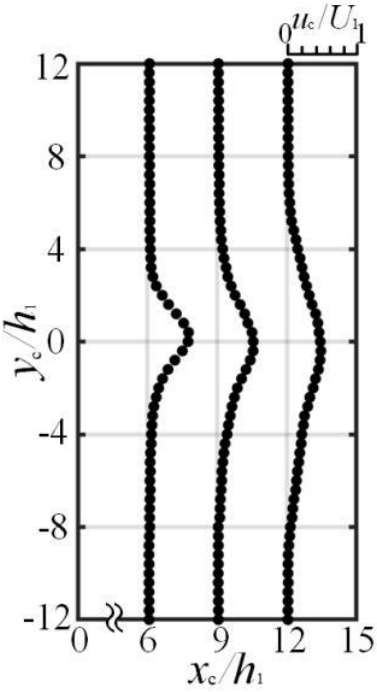

(b) Suction flow; θ_c = 57.2˚

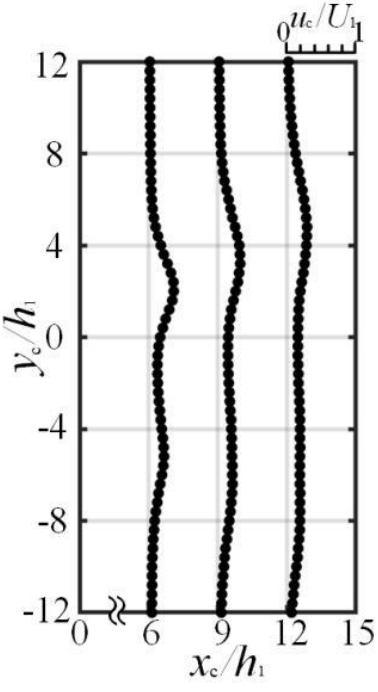

(c) Synthetic jet; f = 10Hz; θ_c = 28˚

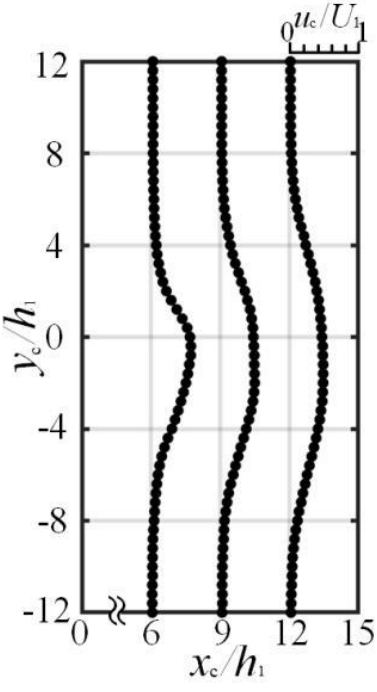

(d) Synthetic jet; f = 100Hz; θ_c = 44˚

Fig. 3-12 Velocity distribution for continuous flow and synthetic jet under R/h_1 of 3 and ξ of 0.06.

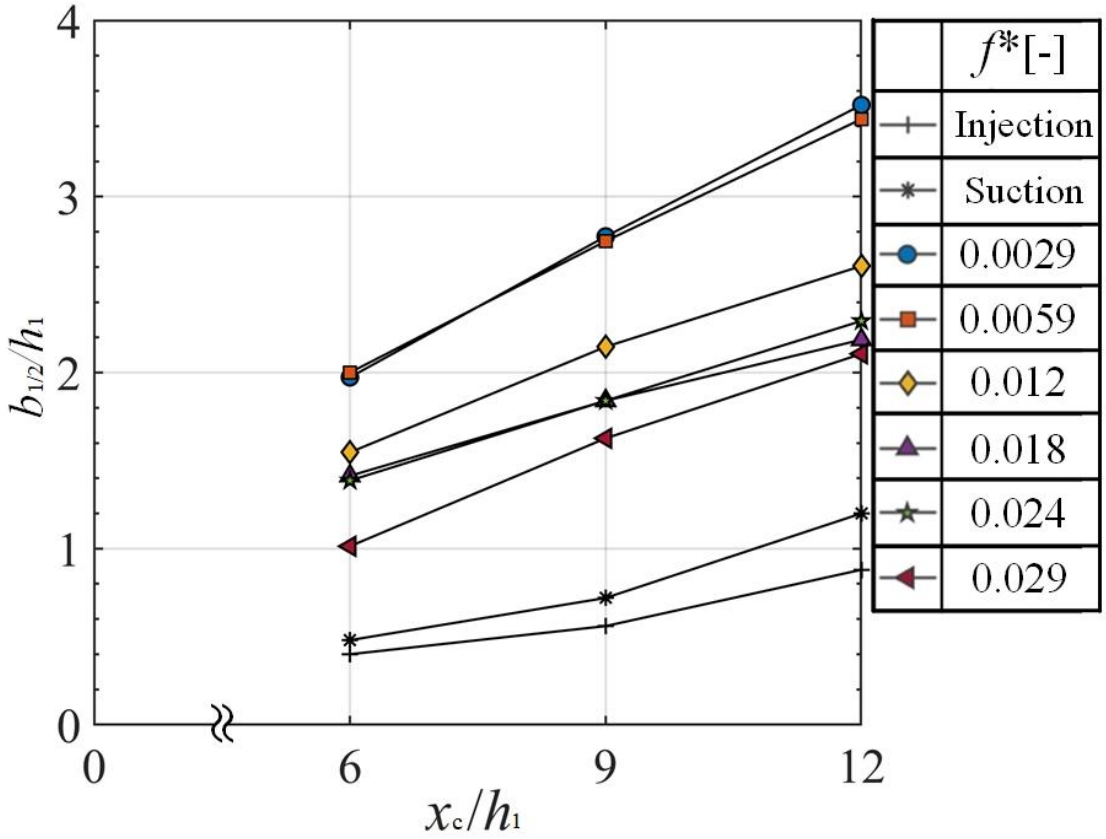

Fig. 3-13 Dimensionless half width comparison for different frequency under R/h_1 = 3, ξ = 0.06.

3.5 Summary

In this chapter, the effect of the ratio of cylinder radius and the width of primary slot R/h_1 on the deflection characteristics of the primary jet is investigated. On the basis of setting four different R/h_1, the dimensionless frequency of the synthetic jet f^*, the frequency f and the momentum ratio of primary flow to secondary flow ξ are used as parameters in the experiments for comparison and analysis. In addition, the effect of dimensionless frequency and frequency of the synthetic jets on the unsteady characteristics of the primary are discussed. The conclusions as followed:

1) Besides the momentum ratio between primary jet and secondary flow ξ, and the dimensionless frequency f^*, the deflection angle of jet also depends on the ratio of cylinder radius to the width of the primary slot R/h_1.

2) For the secondary synthetic jet, choosing a suitable R/h_1 is able to ensure a good deflection capability while achieving fine adjust of the deflection angle. A large R/h_1 can hardly control the deflection angle by adjusting the momentum ratio ξ, while a small R/h_1 has a poor deflection capability. And for secondary suction flow, a larger R/h_1 means a larger deflection angle.

3) Although the deflection angle is different for different R/h_1 under the condition of the same dimensionless frequency f^*, the structure of the jet is similar.

4) The synthetic jet frequency has a effect on the flow pattern of the jet including the distance interval of the inverse Karman vortice pair and the size of the vortice pair.

5) The half width of the jet and the value of maximum velocity depend on the frequency of the secondary synthetic jet f. The lower the frequency f, the faster the velocity attenuation and the wider the half width.

-Chapter 4-

Jet Direction Control Using Circular Cylinder with Tangential Blowing

4.1 Introduction

To date, the research into CCW has been directed towards reducing drag and simplifying the CCW systems while maintaining lift enhancement. However, the CCW system including tangential blowing cylinder also have a problem that the flow characteristics influenced by various factors which has not been study clearly. Therefore, in this chapter, in order to study the effect of the parameters of the CCW system including fluid and shape parameters on the characteristics of the primary jet, a tangential blowing cylinder is set up as a simple CCW system to control the direction of the primary jet. The effects of the momentum coefficient C_μ, the slot angle θ_j, the jet width W and the eccentricity rate of cylinder ε on the deflection angle of primary jet θ_c are investigated in various experiments. In addition, the unsteady characteristics of the primary jet is discussed using velocity fluctuations at downstream of the tangential blowing cylinder. Generally, the traditional method of using a single blade will stall with the attack angle exceeding 20°, but the experiment results show that the primary jet can be bent to approximately 90° by using the tangential blowing cylinder, much more than by the conventional method of changing the blade angle, and the optimal jet angle for controlling the jet direction is also discussed in this chapter.

4.2 Nomenclature

b : Width of slot [mm]

C_D : Drag coefficient [-]

C_L : Lift coefficient [-]

C_P : Pressure coefficient [-]

C_μ : Momentum coefficient of blowing jet [-]

l : Span length of cylinder [mm]

D : Diameter of cylinder [mm]

d : Distance from nozzle center line [mm]

f : Frequency of vortex shedding [Hz]

H : Height between two plane plates [m]

P : Pressure of cylinder surface [Pa]

P_a : Atmospheric pressure [Pa]

R : Radius of cylinder [mm]

Re : Reynolds number [-]

R_m : Measurement point radius [mm]

S : Arc length of measurement point radius [mm]

S_c : Arc length of centroid position [mm]

S_1 : Arc length from front edge to first point of intersection between $0.3U_{max}$ and velocity distribution [mm]

S_2 : Arc length from front edge to second point of intersection between $0.3U_{max}$ and velocity distribution [mm]

St : Strouhal number [-]

$|U|$: Local velocity [m/s]

U_p : Time average velocity of primary jet [m/s]

V_j : Time average of blowing jet [m/s]

U_{max} : Maximum velocity [m/s]

u : Velocity along x axis [m/s]

V : Kinematic viscosity [$m^{2/}s$]

v : Velocity along y axis [m/s]

W : Nozzle width [mm]

Greek symbols

ε : Eccentricity rate[-]

θ : Angle from front edge [$^{\circ}$]

θ_s : Angle of separation point [$^{\circ}$]

θ_1 : Angle of first point of intersection between $0.3U_m$ and velocity distribution [$^{\circ}$]

θ_2 : Angle of second point of intersection between $0.3U_m$ and velocity distribution [$^{\circ}$]

θ_j : Slot angle from front edge [$^{\circ}$]

θ_c : Deflection angle from back edge [$^{\circ}$]

4.3 Experimental setup and method

4.3.1 Experimental equipment

The experimental apparatus is shown in Figure 4-1. And Figure 4-2 depicts a top view of the test section. In this study, the tangential blowing cylinder was utilized as a simplest CCW model[39,40]. The size of test platform for the experiment is $1m^2$ and it was set at the downstream of the wind tunnel. To study the effect of the ratio of jet width(nozzle width) to cylinder diameter on the primary jet, the nozzle as the wind tunnel can be replaced in the experiment, and three different types of nozzles with width of W=100mm, 150mm and 200mm were prepared. To ensure the two dimensional characteristics of flow in the experiment, two solid aluminum plates with the same height as the exit of the wind tunnel were installed at both sides of the wind tunnel, and a acrylic plate with the same size as the test platform is installed above the experimental circular cylinder.And because the flow development region where the potential core exists is $x < 6W$ in the two-dimensional jet[41], the tangential blowing cylinder installation position is $1W$ distance from the wind tunnel which is on the coordinate axis of $x = 0$, $y = 0$ as shown in Figure 4-2. The bottom of the tangential blowing cylinder was connected with the plenum tank through a pipe, and the jet sheet ejected from the slot of cylinder is generated by the air from the blower (Showa Denki Co.,Ltd U2V-70S). The velocity of the jet sheet was observed by a differential pressure gauge and controlled by a inverter and a valve. The primary jet velocity from the wind tunnel was generated and adjusted by a blower (Showa Denki M2D2E-6R311) and a inverter (Mitsubishi Electric FR-A720-3.7K) respectively, and the velocity was observed by setting a Pitot tube connected to differential pressure gauge at the center of the wind tunnel section.

The specific parameters of the cylinder are shown in Figure 4-3. In order to minimize the blockage effects[42-44], this chapter choose to use a hollow cylinder with a small diameter which has a outer diameter of 50mm and a inner diameter of 30mm. And the span length l and aspect ratio of the cylinder l/D are 200mm and 4 respectively.The test cylinder has a slot with a fixed width of b=1mm on the span direction. From the perspective of top view, the lower part of the cylinder slot is a semicircle with a radius of 4.25 mm, and the upper part is

composed of a quarter of an ellipse with a major axis of 49 mm and a minor axis of 30 mm. In order to make the jet sheet direction consistent with the outer circumference of the cylinder, the outer surface of the cylinder in the range of θ = 90~110° was designed as a plane. In addition, there are 37 static pressure holes (with a diameter of 0.5mm) on the cylinder surface which are helically distributed on the span direction of the cylinder from z=100 to 137 mm, and the spacing of the static pressure holes near the slot is 5° while the spacing of other static pressure holes is 10°. Five digital differential pressure gauges (Okano Works DMP202n12, measurement accuracy ±0.2% FS±1dig, time resolution 1 Hz) were connected to the pressure holes by pipes to measure the pressure distribution.

To observe the flow pattern of the test fluid around the cylinder, a digital camera (casio ex-100pro) was placed on the top of the test platform to take pictures with a shutter time of 1/480s. The visualization of fluid is achieved by using the smoke wire method. The wire adopts nickel chromium wire with a diameter of 0.35mm and the smoke material adopts liquid paraffin. In addition, the wire is set at the position of $x \approx$ - 200 mm near the exit section of the wind tunnel as close as possible and the height of the wire is set at the middle of the static pressure holes on the span direction of the cylinder. Two halogen lamps were placed on the upper and lower sides of the measuring plane as light sources.

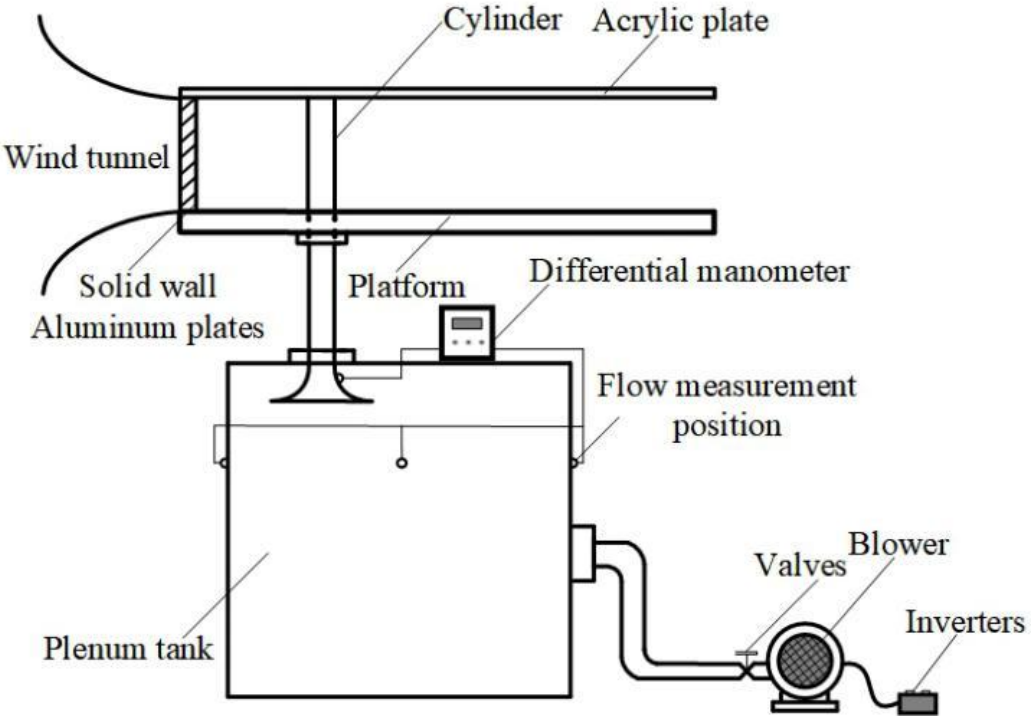

Fig. 4-1 Experimental apparatus.

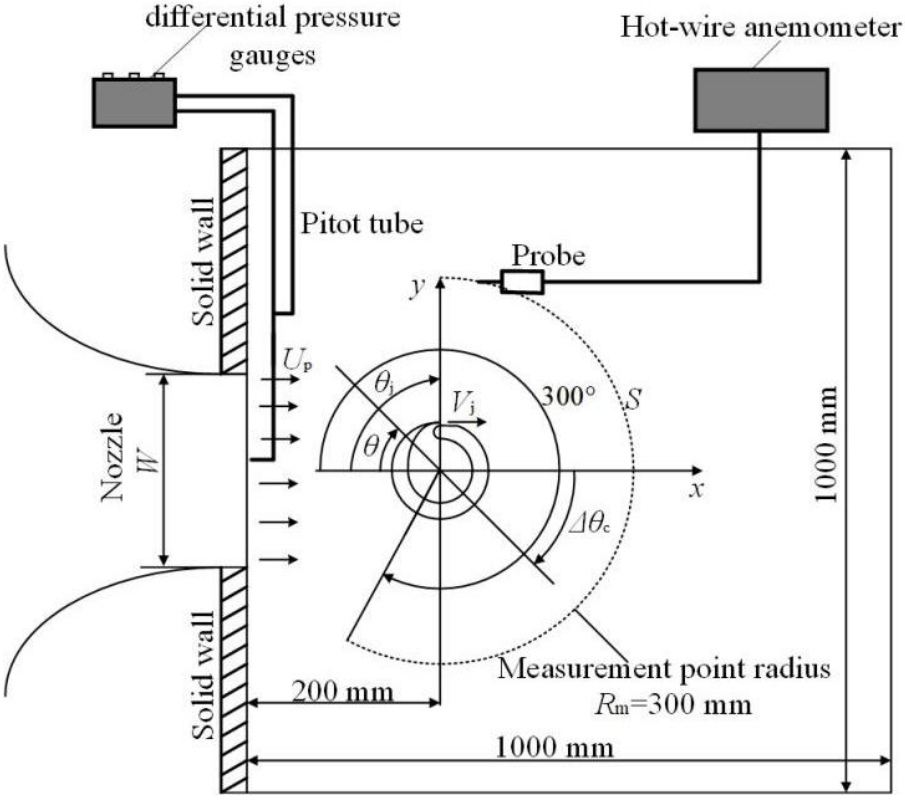

Fig. 4-2 Schematic of test section for experiments.

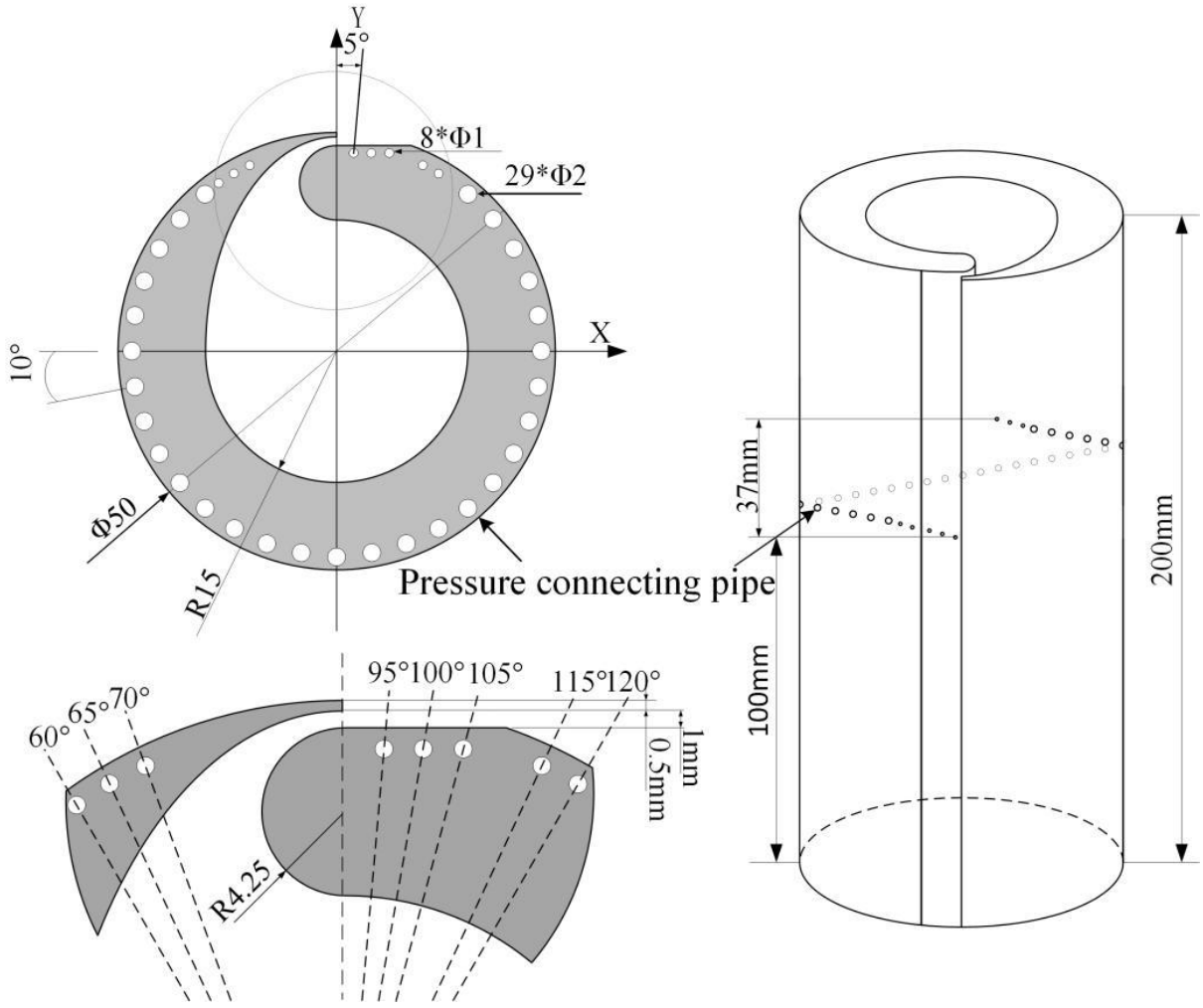

Fig. 4-3 Schematic of circular cylinder with tangential blowing.

4.3.2 Velocity measurement method

In order to study the unsteady characteristics of the test fluid around the cylinder, 42 measuring points were set on the coordinate axis as shown in Figure 4-2. The measuring arc has a radius R_m of 300mm and a measurement angle range from 90° to 300°, and the angle interval of the measuring points is 5°. The flow velocity measurement equipment use hot wire anemometer (KANOMAX MODEL 1011, Smart CTA 7250) and I-type probe (KANOMAX 0251R-T5). The calibration method is to place the Pitot tube and I-type probe at the same position at the middle of the wind tunnel exit section, then measuring 13 groups of flow velocity from 0 to 20m/s with the Pitot tube and I-type probe to record the flow velocity and the corresponding output voltage value. Finally the two groups of corresponding results are transmitted to the computer through the conversion interface, and the correction curve is obtained by calculation.

In the experiment, the height of I-type probe is set at the midpoint of 37 static pressure holes in the cylinder span direction. Although this chapter focus on the characteristics of two dimensionless flow, the flow around the cylinder is strictly three dimensionless flow, especially at both sides of the circular cylinder near the baffle surface area[45,46]. The I-type probe is set near the center of the cylinder span, however, the influence from the baffles can not be completely ignored. But, the research in this chapter mainly focuses on the deflection characteristics of the flow on the x-y plane, so this influence in the experiment is considered to be ignored. Furthermore, the sampling time and frequency of the Type I probe are 20s and 10000Hz respectively when measuring the velocity distribution. And for the measurement of spectrum analysis, the sampling time and frequency are 30min and 10000Hz respectively.

4.3.3 Experimental evaluation

In this chapter, the experiment was set at the the range of Reynolds number around 10^4. It is because, under this condition, the damping coefficient acting on the cylinder and the Strouhal number of the Karman vortex street shows no dependence on the Reynolds number *Re* [41]. Therefore, in the following experiments, the Reynolds number is kept around $Re = 2.7 \times 10^4$ ($U_p \approx 8.3$ m/s). The formula for the Reynolds number is expressed as follows:

$$Re = \frac{U_p D}{V} \tag{1}$$

Here, U_p is the velocity of the primary jet [m/s], D is the diameter of the cylinder [mm] and V is the kinematic viscosity [m^2/s]. In order to study the unsteady characteristics of the flow behind the cylinder, the spectrum analysis of the flow velocity data obtained by the hot-wire anemometer was conducted. And the Strouhal number was obtained from the main frequency component of spectrum of velocity fluctuations, and its expression is as follows .

$$St = \frac{fD}{U_p} \tag{2}$$

Here, f is the Frequency of vortex shedding, D is the diameter of the cylinder [mm], U_p is the velocity of the primary jet [m/s]. Regarding the calculation of pressure coefficient, the static pressure distribution around the cylinder can be measured by 37 static pressure holes on the surface of the circular cylinder. Considering the actual situation, because of the unsteady characteristics of the experimental fluid and the viscosity of the air, it will takes some time for the pressure on the surface of the cylinder to reach balance after the releasing of test fluid and the fluctuation of flow rate will exist consistently. Therefore, in the following experiment, the differential pressure gauge and Matlab were used to measure with sampling time of 50s and sampling frequency of 10000Hz, and take the measured time-averaged pressure as the surface pressure of the cylinder. And we set the pressure of the cylinder surface as P, then the pressure

coefficient can be calculated by subtracting the atmospheric pressure from the surface pressure of the cylinder placed in the primary jet and dividing it by the pressure of primary jet :

$$C_P = \frac{P - P_a}{0.5\rho U_p^2} \quad (3)$$

Here, P is the pressure of the cylinder surface [Pa], P_a is the atmospheric pressure [Pa], ρ is the air density [kg/m^3], U_p is the velocity of primary jet [m/s]. For the lift coefficient C_L, it was obtain by integrating the calculated pressure distribution of the cylinder surface [47-49]. The formula is expressed as follows:

$$C_L = -\frac{1}{2}\int_0^{2\pi} C_P sin\theta d\theta \quad (4)$$

Here,C_P is the pressure coefficient ,θ is the angle from front edge.One of the main evaluation parameters in this chapter is the momentum coefficient C_μ. The adjustment method is to change the jet sheet from the slot of cylinder while the velocity of primary jet is fixed, and the setting range of the momentum coefficient from bottom to top is C_μ = 0 ~ 0.364. The velocity of primary jet and velocity of jet sheet are time-averaged values, and the sampling time and frequency are 50 s and 10000 Hz respectively. The expression of momentum coefficient C_μ is as follows [50]:

$$C_\mu = \frac{V_j^2 b}{U_p^2 W} \quad (5)$$

Here, V_j is the jet sheet velocity [m/s], U_p is the velocity of the primary jet [m/s], b is the slot width of circular cylinder[mm] and W is the jet width(nozzle width) [mm]. Except the momentum coefficient C_μ, there are other three important experimental parameters in this chapter including the angle between the cylinder slot and the front edge of the cylinder θ_j , the width of the primary jet (nozzle width) W and the eccentricity rate of the cylinder ε. The slot

angle from the front edge θ_j can be adjusted by rotating the cylinder ,and the width of the primary jet can be changed by replacing the size of nozzle. The eccentricity rate ε is adjusted by adjusting the relative position of the cylinder and the wind tunnel in the y direction. The formula for the eccentricity rate ε is expressed as following:

$$\varepsilon = \frac{2d}{(W-\mathrm{D})} \tag{6}$$

Here, d is the distance from the cylinder to the centerline of the nozzle [mm], W is the jet widths [mm], and D is the diameter of the circular cylinder [mm]

And about the deflection angle, the calculation method is similar to chapter two, the center of gravity is still be considered as the deflection center of the primary jet to evaluate the deflection ability.And based on the results of the pre-experiments, isometric line was set at 30% of the maximum velocity of velocity distribution as shown in Figure 4-4 below.

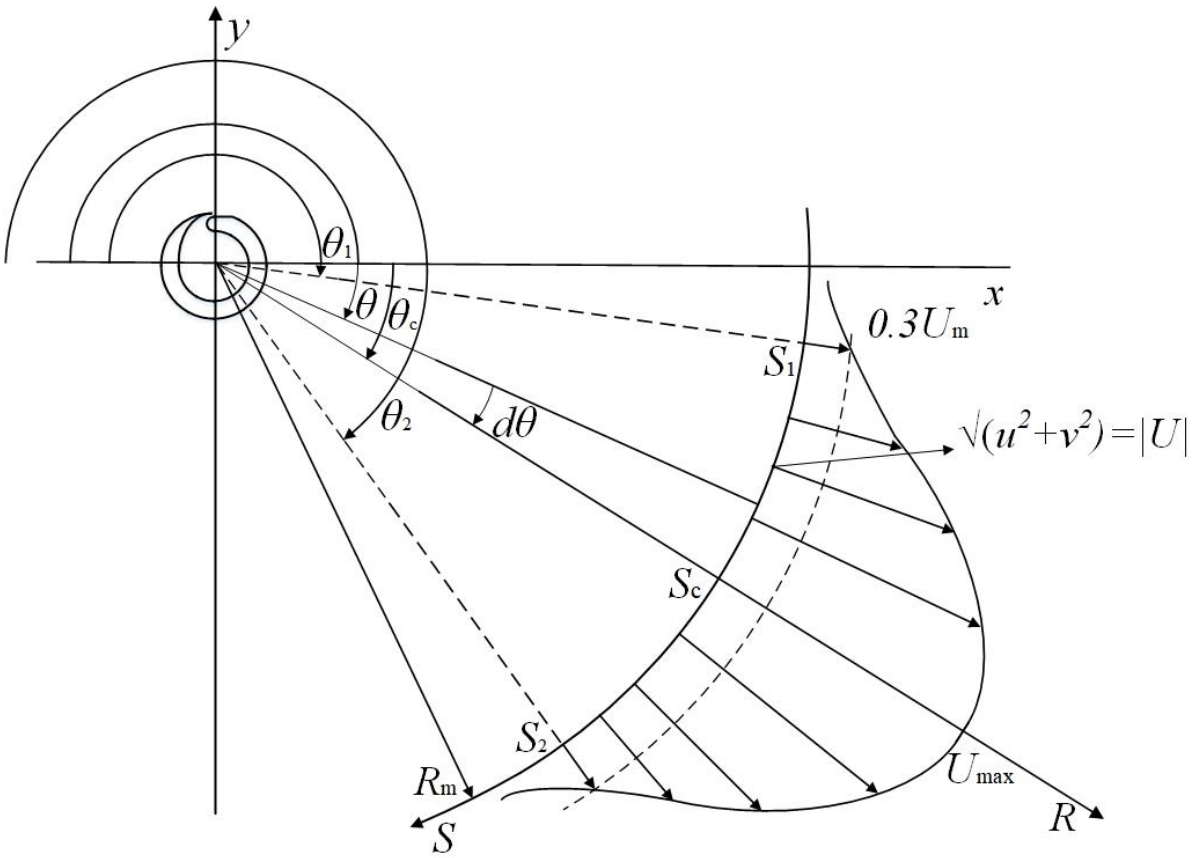

Fig. 4-4 Diagram to calculate velocity distribution centroid.

4.4 Results and Discussion

4.4.1 Influence of momentum coefficient

Before investigating the influence of slot angle of cylinder θ_j, jet widths W and eccentricity rate ε on the characteristics of primary jet, we need to study the deflection angle of primary jet under different momentum coefficient. So in this chapter, the slot angle θ_j was fixed at 90°, and the jet width W, eccentricity rate ε were fixed at 200mm and 0 respectively. Next, the visualization experiments for the condition for only using primary jet $C_\mu = 0$, low momentum coefficient $C_\mu = 0.068$ and high momentum coefficient $C_\mu = 0.364$ were conducted by using smoke wire method.

Figures 4-5(a),(b),(c) respectively show the instantaneous visualization results for $C_\mu = 0$, 0.068 and 0.364 under the condition of $\theta_j = 90°$,W=200mm and ε =0. In Figures 4-5(a), the working fluid only has the primary jet, it is evident that the high concentration of smoke generated from the wire, and vortices are found in the velocity shear layer behind the trailing edge of the cylinder due to the Kelvin-Kemholz instability. And these vortices alternate with opposite vortices at the trailing edge of the cylinder (Karmen vortex street) after passing through the cylinder, is found in the velocity shear layer behind the trailing edge of the cylinder due to the Kelvin-Kemholz instability, and these vortices alternate with opposite rotating direction behind the trailing edge of the cylinder which is the Karman vortex street. However, this instability occurs locally and be considered to have no significant effect on the deflection characteristics of the primary jet. When the momentum coefficient C_μ =0.068 and 0.364, as shown in Figures 4-5(b) and Figures 4-5(c), with the injection of the jet sheet, the jet sheet flows along the cylinder surface due to the Coanda effect. And the the separation of the boundary layer above the slot of cylinder is restrained due to the jet sheet on the surface of the cylinder which is different form Figures 4-5(a). And the primary jet is also dragged to the same side by the jet sheet, which causes the primary jet to deflect to the opposite side of the cylinder slot. Comparing with Figures 4-5(b) and Figures 4-5(c), with the increase of the momentum coefficient C_μ, although the flow field has not changed, the deflection angle of the primary jet obviously increases.

Figure 4-6 shows the pressure distribution on the surface of circular cylinder for different momentum coefficients ($0 \leq C_\mu < 0.4$) under the condition of a slot angle of $\theta_j = 90^\circ$, W=200mm and $\varepsilon = 0$. The horizontal axis is the angle from front edge of cylinder θ, and the vertical axis is the pressure coefficient C_P. Figures 4-7 shows the relationship between the angle of separation point of a jet sheet on the cylinder surface θ_s and the momentum coefficient C_μ. The horizontal axis represents the momentum coefficient C_μ, and the vertical axis represents the separation point angle θ_s. The measurement method of separation point angle θ_s in this chapter is not strict determined from the velocity gradient, but relies on the method from Okamato et al[51], which is estimated by the pressure distribution on cylinder. In Figure4-6, when only using a primary jet as the work fluid (C_μ =0), a typical pressure distribution on the surface of the cylinder with laminar flow separation is obtained (corresponding to the Figure 4-4(a)). As the momentum coefficient C_μ increases, the pressure coefficient C_P gradually decreases from the leading edge of the cylinder to the cylinder slot($0^\circ \leq \theta \leq 90^\circ$). Whereas in the range of $90^\circ \leq \theta \leq 120^\circ$ on the cylinder surface, all the conditions of $C_\mu \geq 0.030$ have a jump of pressure in the pressure distributions which is because of the irregular design near the cylinder slot. And in the range of $\theta \geq 120^\circ$ on the cylinder surface, the pressure coefficient C_P increases gradually in the conditions of momentum coefficients $C_\mu \geq 0.030$ while the separation point also shifts backwards with increasing of momentum coefficient C_μ. Unlike the pressure distribution for the momentum coefficient $C_\mu = 0$ and 0.009, the pressure distribution for the other conditions is not symmetrical. Therefore it can be determined that a lift is generated at the surface of the cylinder.

Figure4-8 show the relationship between the fluid forces on the surface of the cylinder and the momentum coefficients C_μ .The horizontal axes of Figure4.8(a) and4.8(b) are both momentum coefficients C_μ, and the vertical axes represent the lift coefficient C_L and the drag coefficient C_D respectively. Figure4.8(a) reveals that as the momentum coefficient C_μ is accompanied by a corresponding increase in the lift coefficient C_L, indicating that the jet sheet generated high lift forces on the cylinder surface. And in the range of $0 \leq C_L \leq 0.30$, the increase in the lift coefficient is observed to be rapid, while beyond $C_L > 0.30$, the rate of increase of the lift coefficient begins to level off. This finding is consistent with prior

research[52]. And a conventional single blade usually stall at angle of attack $\alpha < 20^{\circ}$ and lift coefficients $C_L < 2$, whereas according to the results in Figure 4-8(a) the lift coefficient C_L reaches a maximum of approximately 8. Therefore, we consider that the primary jet must have undergone a large change in momentum and consequently its traveling direction. And according to Figure 4-8(b), it is apparent that when $C_\mu < 0.05$, the drag coefficient C_D of the cylinder is smaller than that of $C_\mu = 0$. And when $C_\mu > 0.5$, C_D increases monotonically with C_μ increasing due to the generation of high lift [53].

Figure 4-9 shows the flow velocity distribution measured on the arc with radius of R_m=300mm. The horizontal axis is the angle from the leading edge θ, the vertical axis is the dimensionless velocity obtained by dividing the absolute velocity by the velocity of primary jet $|U| / U_p$. When the momentum coefficient $C_\mu = 0$, the shape of the velocity distribution is the same as that of a fluid passing through a cylinder without slot,which has a obvious hollow in the trailing edge area($170^{\circ} < \theta < 190^{\circ}$) and the shape of velocity distribution is approximately symmetrical . This result is consistent with the results of Figure 4-5(a). With the increase of momentum coefficient C_μ , this symmetrical state is gradually destroyed, and the maximum velocity of the velocity distribution and the center of the primary jet are gradually deflected to the right. In this process, the maximum velocity of the velocity distribution also gradually increases. And in the range of $C_\mu \geq 0.068$, the hollow of the velocity distribution gradually disappear, and the shape of the velocity distribution becomes similar to the Gaussian distribution.

Next, the frequency spectrum analysis of the fluid velocity vibration under varies momentum coefficient was conducted. Since it is difficult to find the position of the strongest vibration of velocity, the position of the maximum velocity and the velocity hollow in the velocity distribution shown in Figure 4-9 were selected for spectrum analysis. After comparing the results of several positions, the point with the strongest vibration is selected and shown in Figure 4-10. Figure 4-10(a),(b),(c),(d) shows the spectrum distribution diagram of the trailing edge of the cylinder for $C_\mu = 0$, 0.009 , 0.030 and 0.068 respectively. The horizontal axis is the Strouhal number St and the vertical axis is the spectrum density.It can be seen in Figure4-10(a) and (b), a obvious velocity vibration exist due to the Karman vortex

street generated behind the trailing edge of the cylinder. When C_μ = 0, the Strouhal number St=0.2, and when C_μ = 0.009, the amplitude of velocity vibration decreases while St increases slightly. When C_μ = 0.030, St increases to 0.3, while the amplitude of velocity vibration almost disappears. And for C_μ = 0.068, the velocity vibration totally disappears. It can be confirmed from the results in Figure 4-9 and Figure 4-5 (b) that the hollow of velocity which means the Karman vortex street disappears.

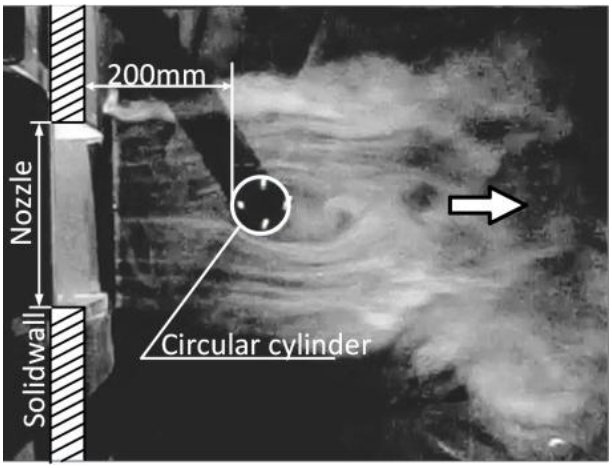

(a) $C_\mu = 0$

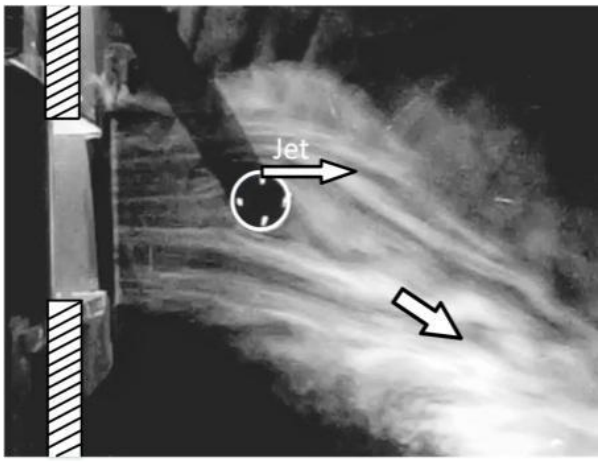

(b) $C_\mu = 0.068$

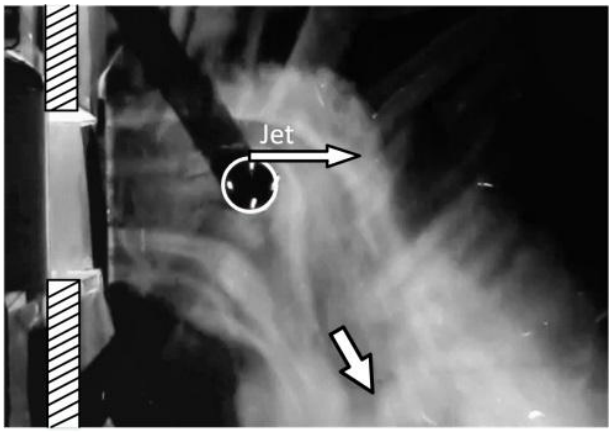

(c) $C_\mu = 0.364$

Fig. 4-5. Flow visualization obtained using smoke-wire method for $\theta_j = 90°$.

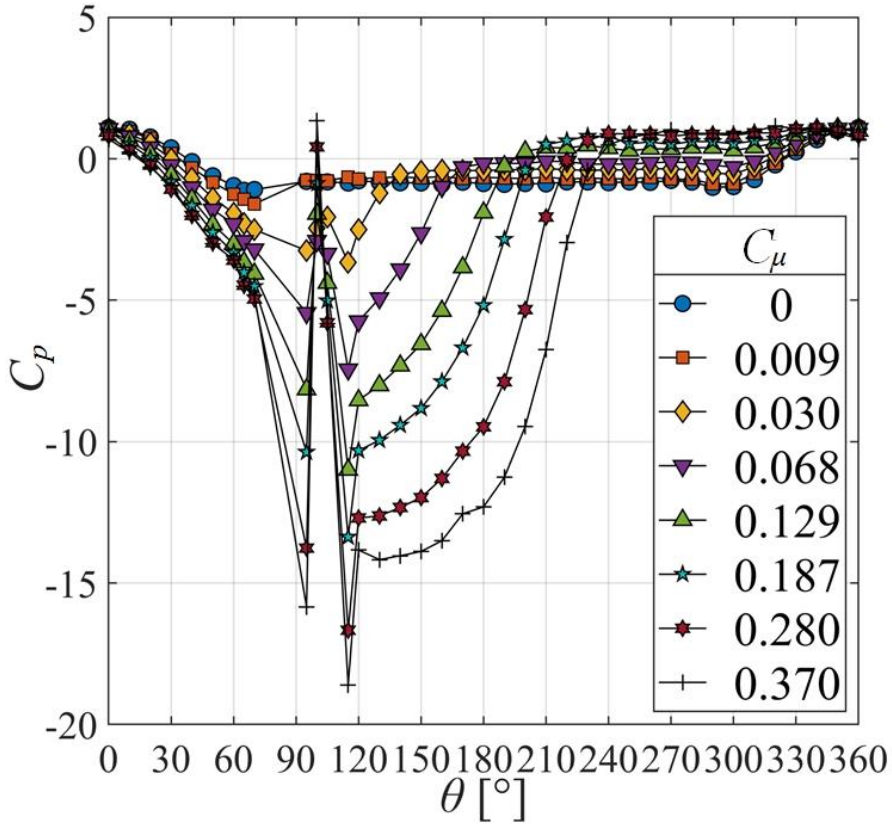

Fig. 4-6. Surface pressure around circular cylinder for $\theta_j = 90°$.

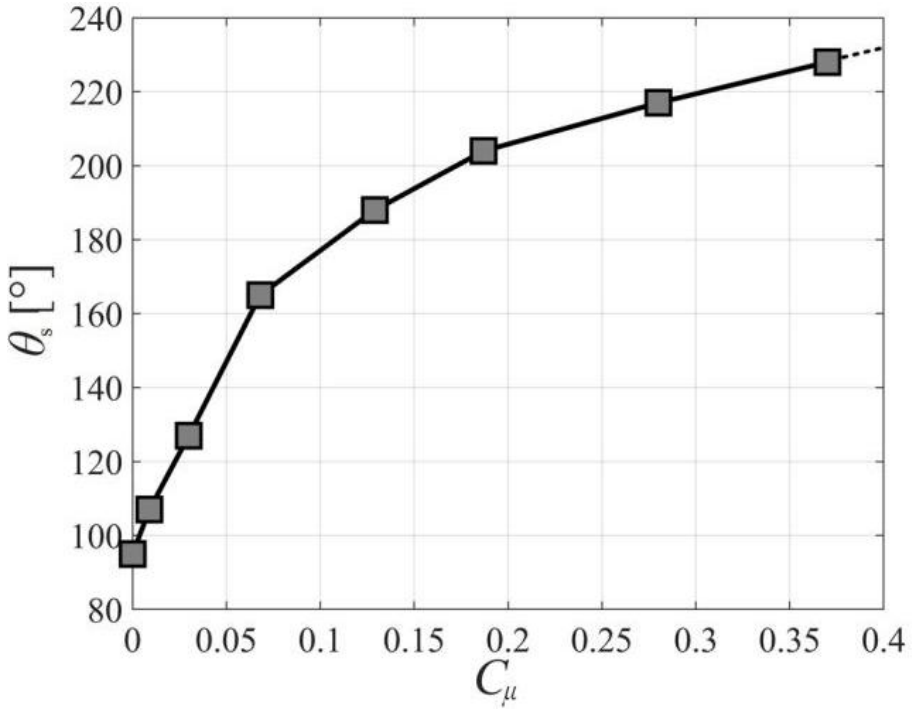

Fig. 4-7. Angle of separation point around circular cylinder for $\theta_j = 90°$.

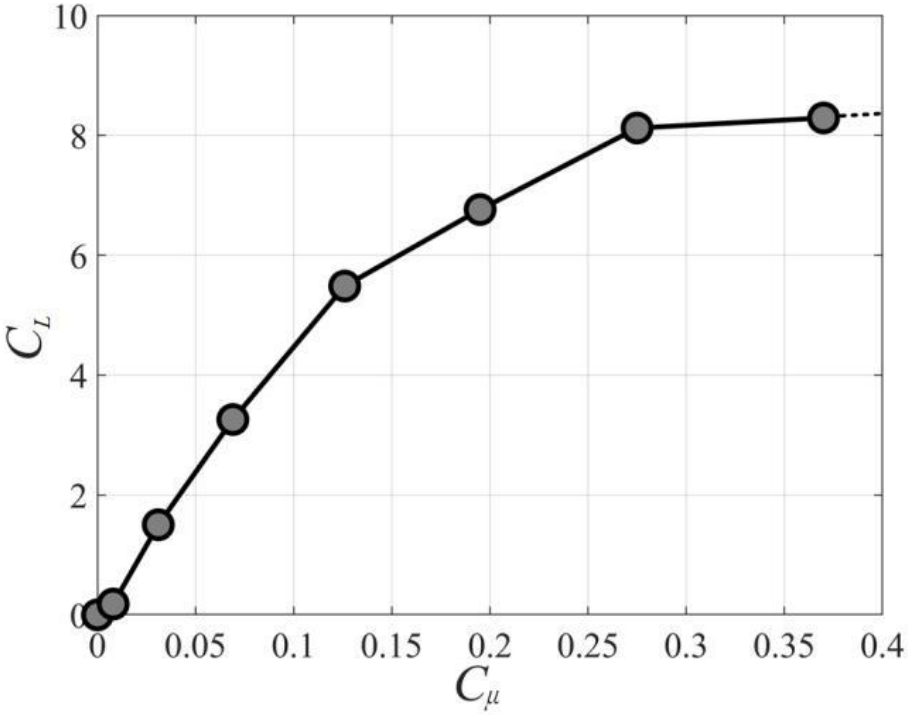

(a) Lift coefficient

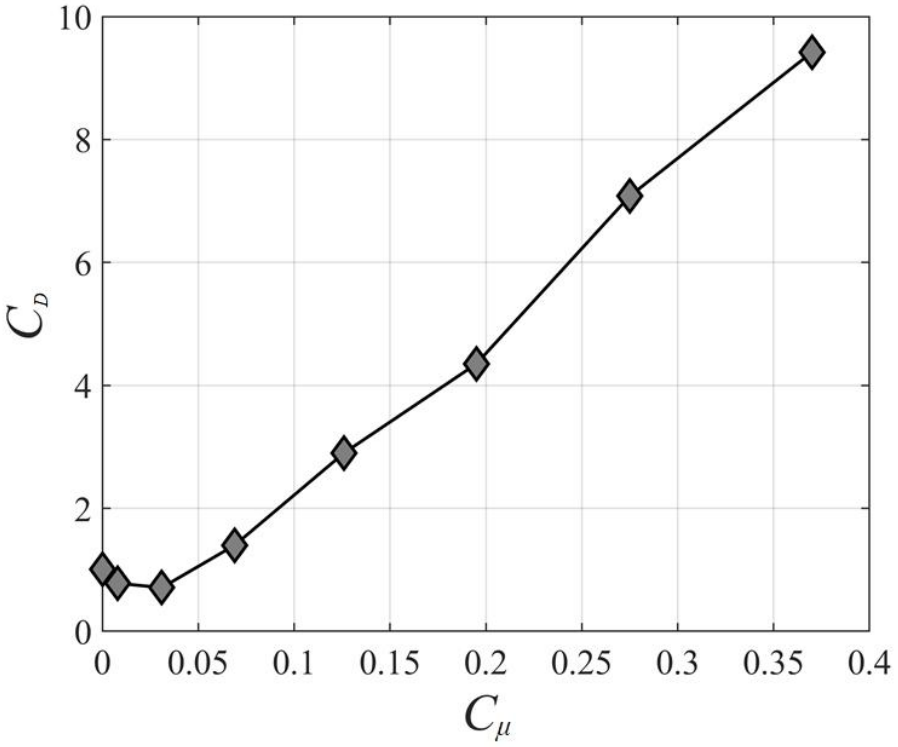

(b) Drag coefficient

Fig. 4-8. Relation between momentum coefficient and lift coefficient and drag coefficient for $\theta_j = 90°$.

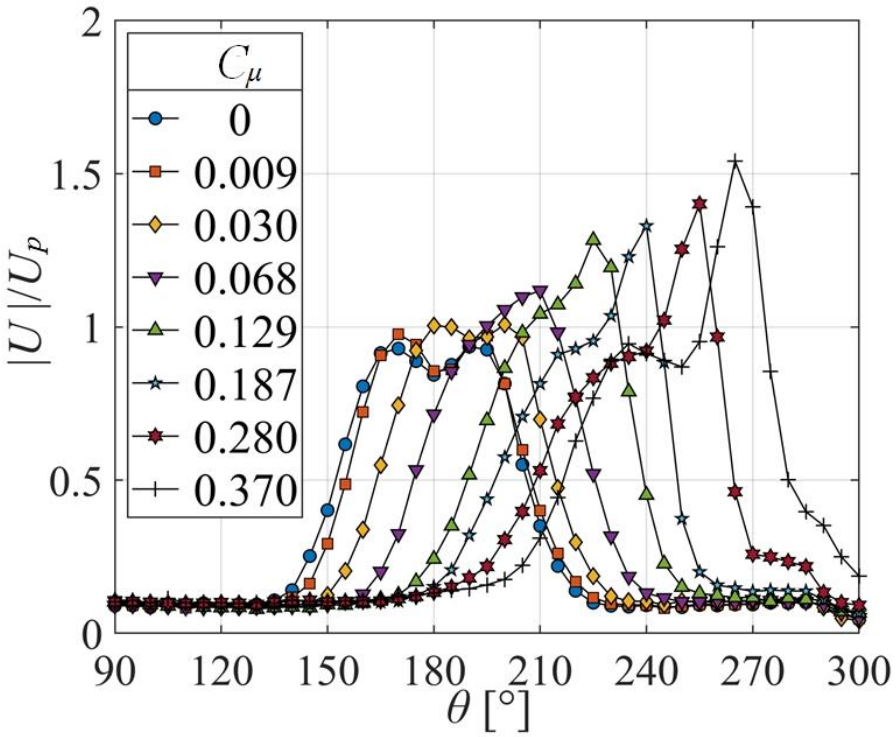

Fig. 4-9 Dimensionless velocity distribution of circular cylinder for $\theta_j = 90^\circ$.

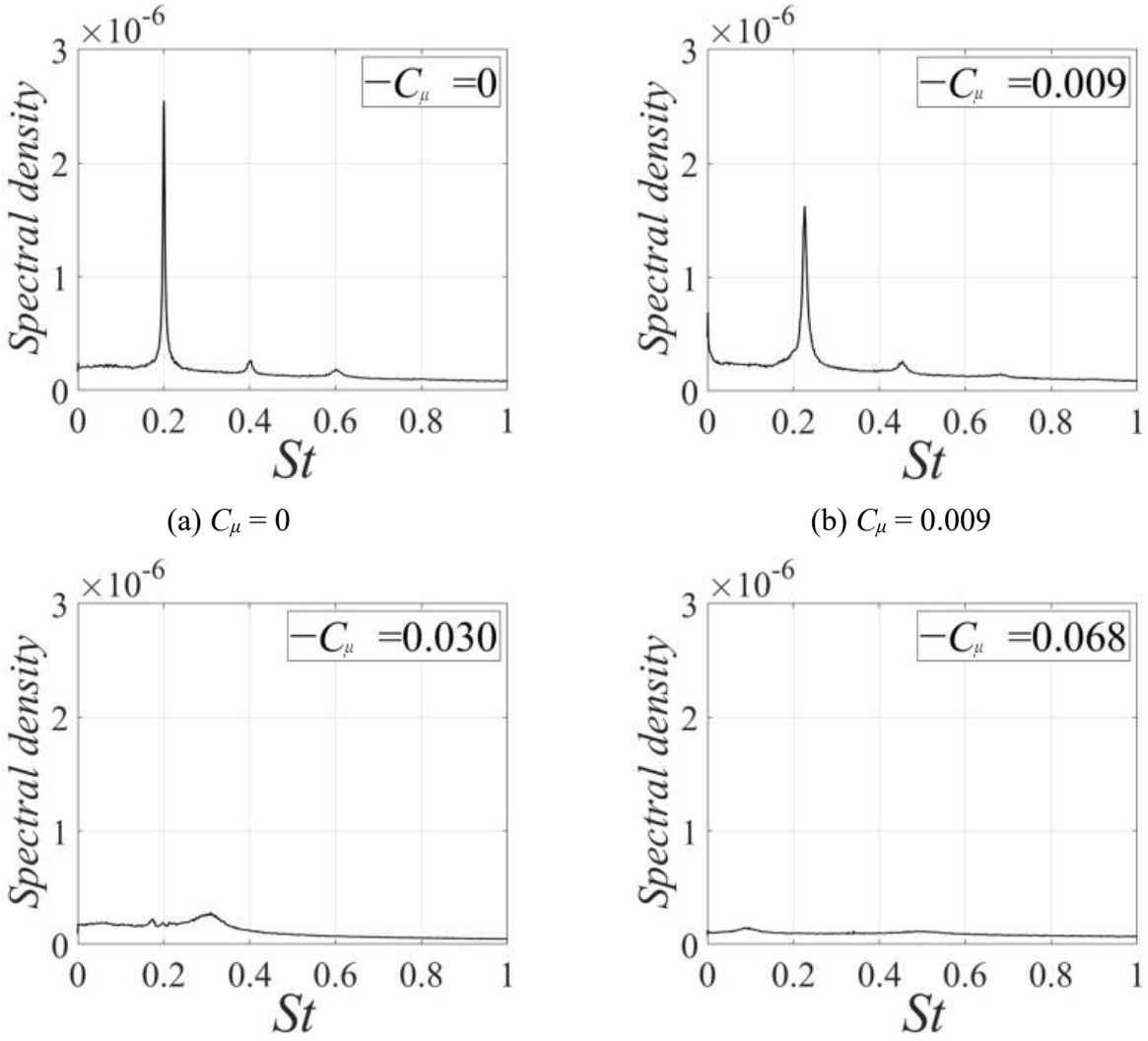

(a) $C_\mu = 0$ (b) $C_\mu = 0.009$

(c) $C_\mu = 0.030$ (d) $C_\mu = 0.068$

Fig. 4-10. Spectrum of fluctuations in wake of circular cylinder for $\theta_j = 90°$.

4.4.2 Influence of injection angle

After investigating the influence of the momentum coefficient on the primary jet, the angle spacing was set at θ_j =90° and study the characteristics of the primary jet for θ_j= 0°, 90°, 180° and 270° respectively. Figure 4-11(a),(b),(c),(d) shows the results of the visualization for slot angles for θ_j= 0°, 90°, 180° and 270°, and the momentum coefficient was fixed at middle value C_μ = 0.187.Comparing the visualization results with Figure 4-11(a) and Figure 4-11(b), although the momentum coefficient and the deflection direction of flow are the same, the deflection angle θ_j of 90° is greater than that of 0°. For θ_j= 180° (Figure 4-11(c)), the flow split into two parts and deflect into the opposite direction. This might attribute to the jet sheet attached to the surface of the cylinder unable to entrain the primary jet above the cylinder, but collided with the fluid below the cylinder instead. For θ_j = 270°, there is only a slight deflection of the primary jet and the deflection direction is opposite from θ_j = 0°and 90°.

Figures 4-12(a), (b) and (c) depict the dimensionless velocity distributions for different momentum coefficients for slot angles θ_j= 0°, 180° and 270°, respectively. The horizontal axis represents the angle from the leading edge θ, the vertical axis represents the dimensionless velocity obtained by dividing the absolute velocity by the velocity of primary jet $|U|/U_p$. Figures 4-12(a) and (c) reveal that as the momentum coefficients C_μ increase, the movement of the velocity distribution are not obvious, and the deflection direction is opposite with each other. For θ_j= 0°, the hollow of velocity distribution behind the cylinder is gradually overcome due to the Coanda effect, and the shape of the velocity distribution is similar to Gaussian attribute to these high momentum coefficients. For θ_j= 270°, this hollow of velocity distribution is always exist which is consistent with the visualization results in Figure 4-11(a) and 4-11(d). For θ_j= 270°, the primary jet split into two parts due to the jet sheet, and this phenomenon become more pronounced as the increase of the momentum coefficient.

In the content above, the velocity distributions for various slot angles θ_j and momentum coefficients were measured in this chapter. However, due to the splitting of the primary jet for θ_j= 180°, using the deflection center of the jet as a evaluation method is considered to be unsuitable. Therefore, the lift coefficient is used to evaluate the deflection ability of

Figure4-12 and Figure4-9, and the calculation method of the lift coefficient is the same as the Figure 4-8(a). Figure 4-13 shows the lift coefficient C_L under various momentum coefficients C_μ for $\theta_j = 0^\circ$, 90°, 180° and 270°. For $\theta_j = 0^\circ$ and 90°, the direction of the lift force is the same and the magnitude of the lift force coefficient depends on the momentum coefficient C_μ. And the lift coefficient for $\theta_j = 90^\circ$ is greater than that for $\theta_j = 0^\circ$ at the same momentum coefficient. For $\theta_j = 180^\circ$, the lift coefficient $C_L > 0$ in the range of $0 < C_\mu < 0.18$. But in the range of $C_\mu > 0.2$, the lift coefficient become negative and monotonically decreases with the increasing of momentum coefficient which is because the jet sheet on the cylinder surface colliding with the primary jet below the cylinder. Based on the results before, $\theta_j = 180^\circ$ is clearly not suitable for jet control. For $\theta_j = 270^\circ$, the trend of the lift coefficient C_L is similar to that for $\theta_j = 180^\circ$, although the lift coefficient C_L starts to decrease monotonically with the increase of momentum coefficient in the range of $C_\mu > 0.05$, the absolute value of the lift coefficient for the same momentum coefficient has no advantage. From the results above, it can be confirmed that $\theta_j = 90^\circ$ has the best deflection performance among these slot angles for $\theta_j = 0^\circ$, 90°,180° and 270°. Based on this conclusion , It can be inferred that there might has a angle of cylinder slot that are close to $\theta_j = 90^\circ$ has better deflection capability. Therefore, in order to find the slot angle of cylinder θ_j with the optimal deflection capacity, the 20° was set as the slot angle interval deflection to study the characteristic of the flow for different momentum coefficients of $\theta_j = 70^\circ$, 110° and 130° and comparing them with the slot angle of $\theta_j = 90^\circ$.

Figure 4-14 shows the relationship between the deflection angle of the primary jet θ_c and the slot angle θ_j for various momentum coefficients C_μ . The horizontal axis represent the momentum coefficient C_μ and the vertical axis represent the deflection angle θ_c of the primary jet. Firstly, for $\theta_j = 90^\circ$, the curve of deflection angle is found to be consistent with its curve of lift coefficient(Fig4-8(a)) and the separation point(Fig4-7). Comparing $\theta_j = 70^\circ$, 90° and 110°, the maximum deflection angle increases as θ_j increases and The curve trend is very smooth and similar with each other. And among these three cases, the maximum deflection angle is about $\theta_c = 77^\circ$ for $\theta_j = 110^\circ$ and $C_\mu = 0.36$. For $\theta_j = 130^\circ$, the deflection angle θ_c increases monotonically with the increase of momentum coefficient C_μ, and the maximum deflection angle reach around 90°. But in the area around $C_\mu = 0.1$, a jump in the deflection angle has

occurred. According to the results of the separation point for $\theta_j = 90^{\circ}$(Fig4-7) calculated from the estimate of pressure distribution, the separation point is around 90° when there is no significant deflection of the primary jet. It is because no pressure drop caused by the jet entrainment of the Coanda effect occurs on the cylinder surface. And as the momentum coefficient C_{μ} increases, the pressure drop caused by the jet entrainment makes the pressure gradient on the pressure surface becomes negative while the separation point gradually moves to downstream. And Figure 4-15 shows the pressure distribution for $\theta_j = 90^{\circ}$. It can be seen that in the region of $C_{\mu} < 0.1$, the pressure distribution is similar to that of Figure 4-7 for $C_{\mu} =$ 0 and 0.009, no significant drop occur in the pressure gradient. Even for $C_{\mu} = 0.030$ and 0.068 in Figure 4-15, only a slight drop in pressure gradient occurs at around $\theta = 150^{\circ}$ due to the increase of velocity of the jet sheet, and no entrainment of the jet occurs. Therefore it can be assumed that the separation point angle of the main jet at this point is approximately $90 < \theta_s <$ 130°. However, for $C_{\mu} = 0.1$, once the angle of separation point θ_s exceeds 130°, the separation point suddenly moves downstream due to the inertia of the jet sheet. This causes the deflection angle to show a sharp increase around $C_{\mu} = 0.1$. Therefore, to smooth control of the primary jet direction, it is appropriate to set a tangential blowing slot at the separation point for $C_{\mu} = 0$ (at around $\theta = 90^{\circ}$). Based on the aforementioned findings, it is feasible to use a tangential blowing cylinder downstream of the two-dimensional plane jet for the purpose of manipulating the deflection angle θ_c from 0 to approximately 90° solely through adjusting the momentum coefficient without necessitating changing to the structural design.

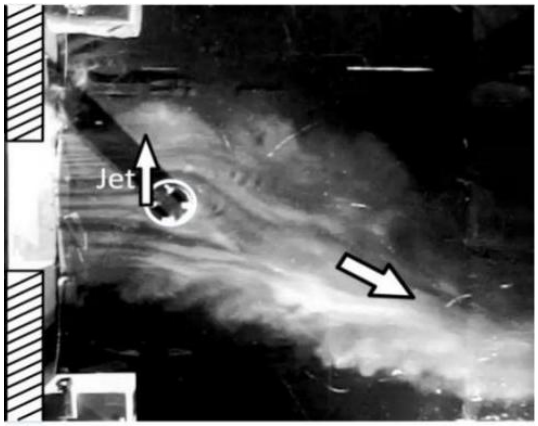

(a) $\theta_j = 0^\circ$

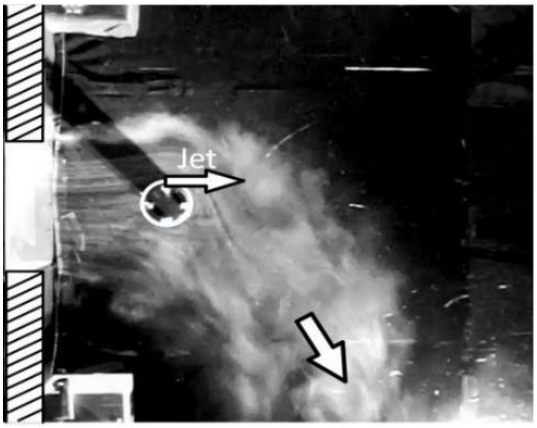

(b) $\theta_j = 90^\circ$

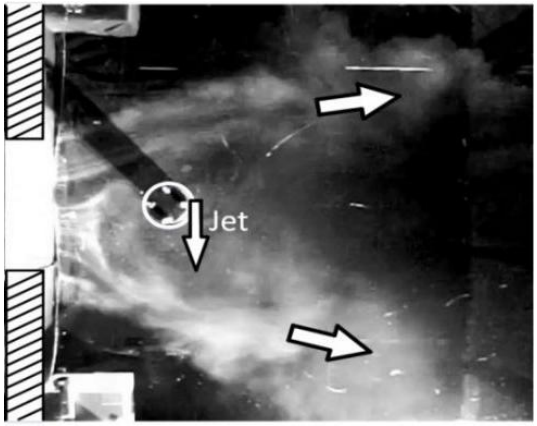

(c) $\theta_j = 180^\circ$

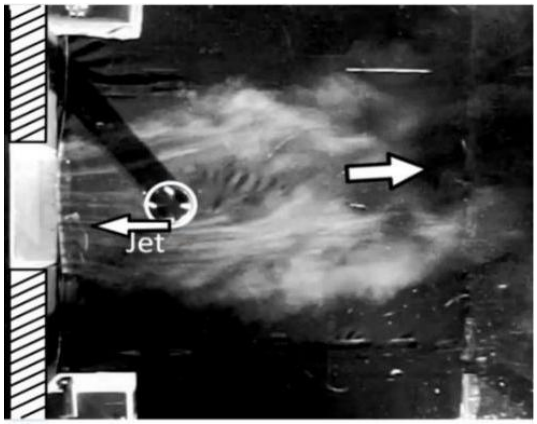

(d) $\theta_j = 270^\circ$

Fig. 4-11. Flow visualization obtained using smoke-wire method for $C_\mu = 0.187$.

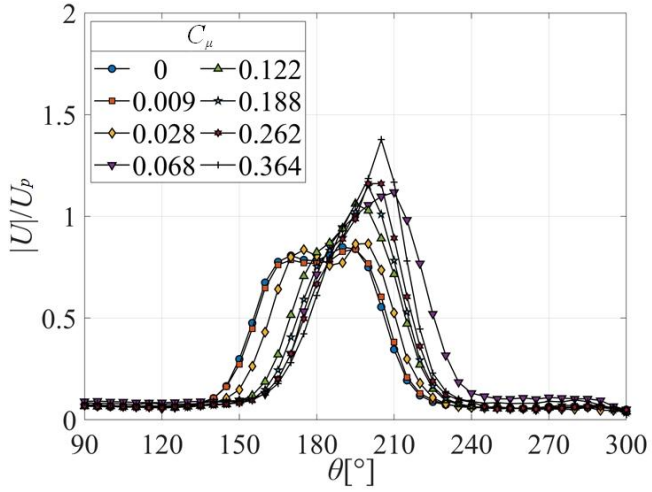

(a) $\theta_j = 0^\circ$

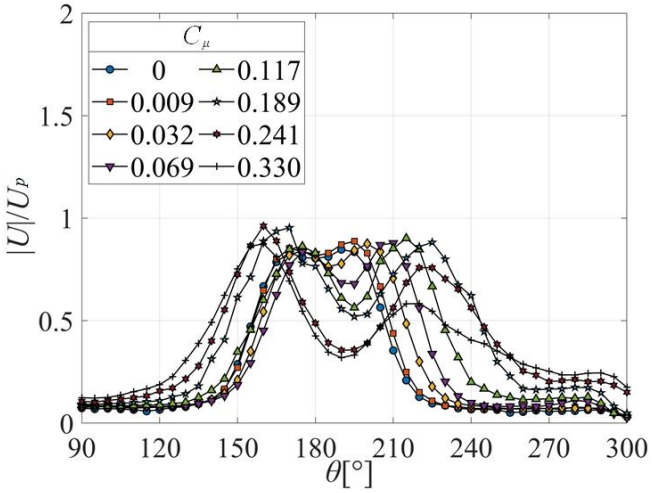

(b) $\theta_j = 180^\circ$

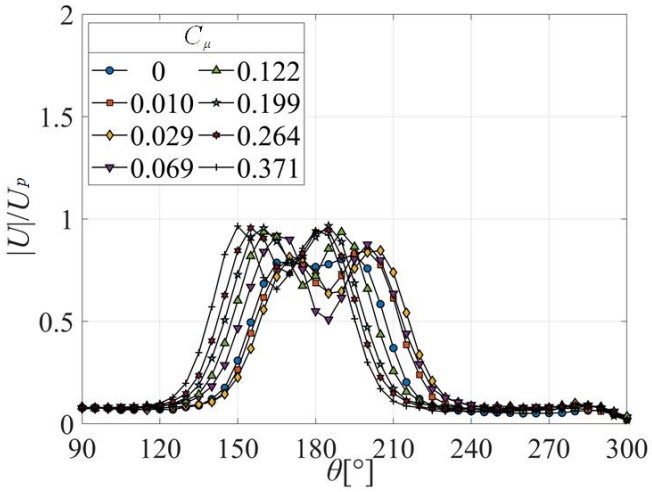

(c)$\theta_j = 270^\circ$

Fig. 4-12. Dimensionless velocity distribution of circular cylinder for $\theta_j = 0^\circ, 180^\circ, 270^\circ$.

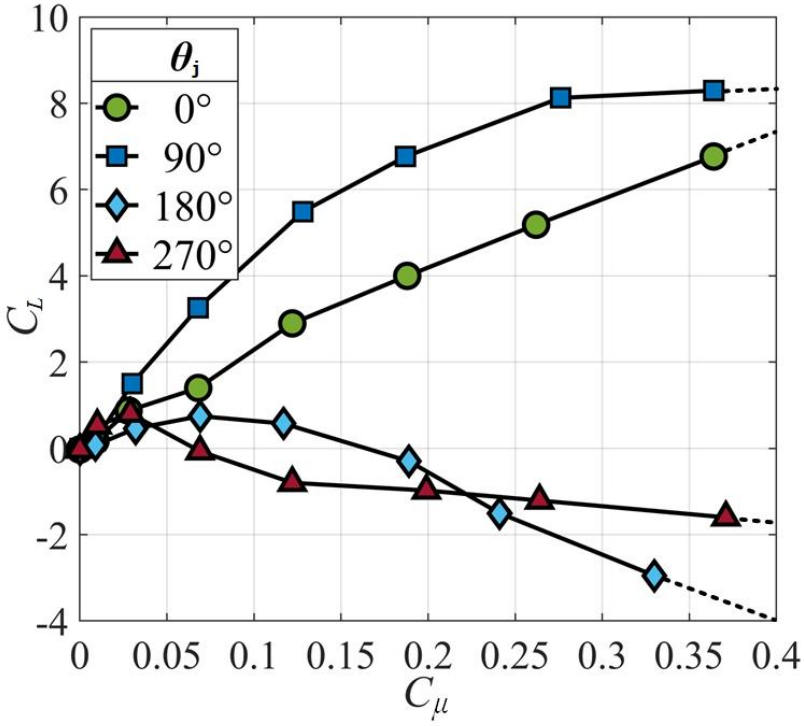

Fig. 4-13. Relation between momentum coefficient and lift coefficient for slot angles of 0°, 90°, 180°, and 270°.

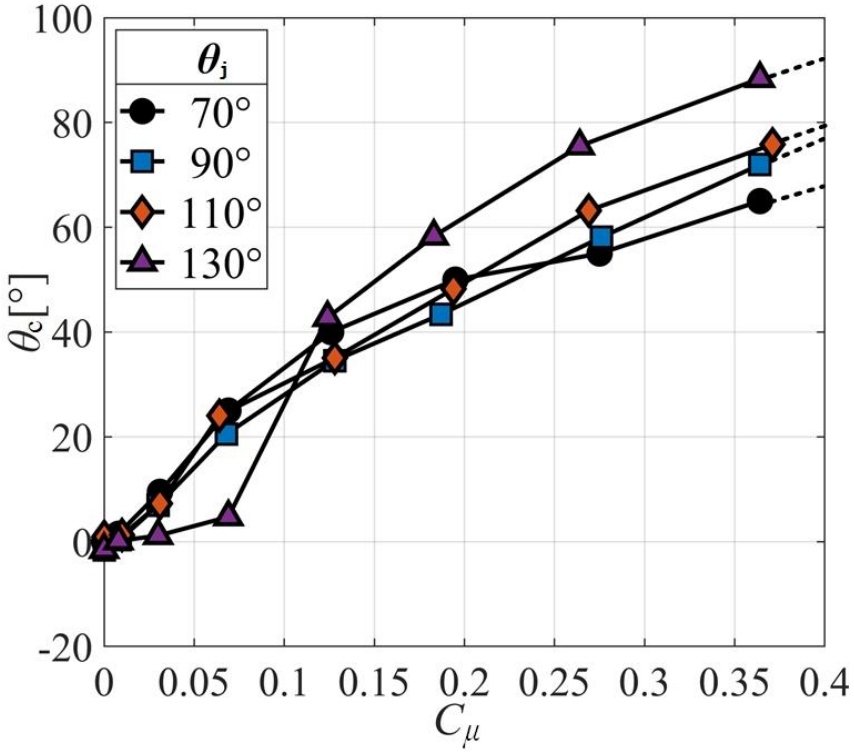

Fig. 4-14. Relation between momentum coefficient and deflection angle of jets for slot angles of 70°, 90°, 110°, and 130°.

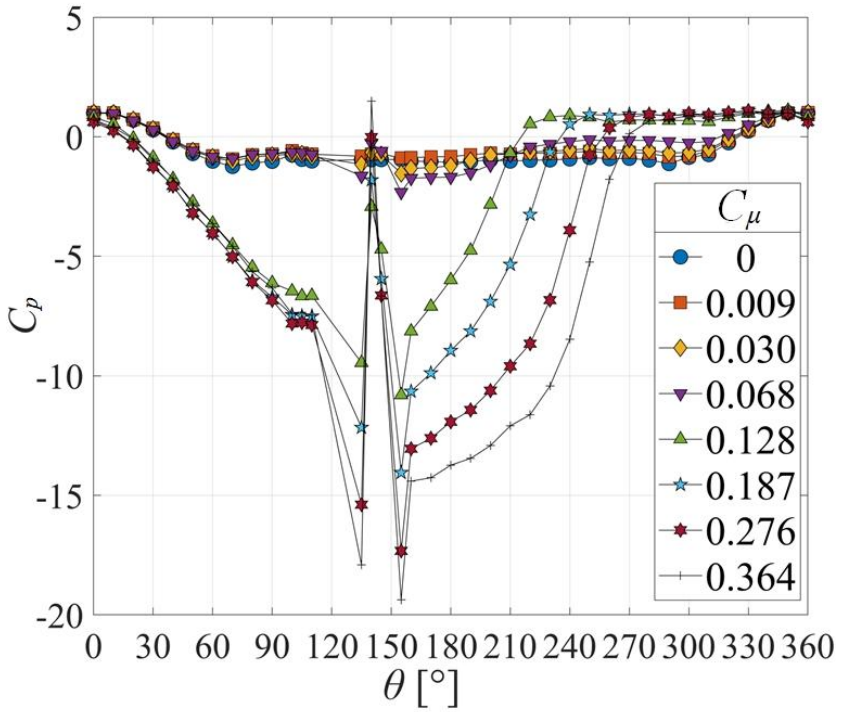

Fig. 4-15. Surface pressure around circular cylinder for $\theta_j = 130^\circ$.

4.4.3 Jet widths and eccentricity of cylinder

Within this chapter, the influence of jet widths on the deflection angle of the primary jet was investigated by varying the nozzles used as a wind tunnel to set different jet widths. Three different nozzles were used for comparison and the widths of nozzles are W = 100, 150 and 200 mm (ratio of jet width to cylinder diameter W/D = 2, 3 and 4), and the slot angle was fixed at 90°. It is noteworthy that momentum coefficient C_μ is a parameter that includes three variables: primary jet velocity U_p , jet sheet velocity V_j and jet width. For the experimental simplicity, the same primary jet velocity and jet sheet velocity are used for different jet widths. Although this method will lend to different values of momentum coefficients under different jet widths, the momentum coefficients is kept in the range of $0 \leq C_\mu < 0.4$. Therefore, this method will not affect the analysis for experiment results.

Figure 4-16(a), (b) and Figure 4-9 show the velocity distribution for W/D = 2, 3 and 4, respectively, under various momentum coefficients. By comparing these Figs, it can be seen that the maximum velocity of the velocity distribution U_{max} decreases with the decrease of W/D. This is because the reduction of jet width will cause the free jet to reach the mixing area faster under the effect of the shear layer. And the velocity distribution shape for C_μ = 0 is different from that in Figure 4-9. In the former results, there is no depression in the velocity distribution,despite the Reynolds number being the same. The is attributed to the narrowing of the vortex trailing generated at the wake of the circular cylinder caused by the reduction of jet width W. The measurement coordinates employed in this chapter are fixed, and hence the velocity depression vanished for W/D=2 and 3. Regardless of W/D, an increase in momentum coefficient C_μ causes a gradual shift of the velocity distribution shape (including the maximum velocity position and the deflection center) towards the right.

Figure 4-17 depict the relationship between the momentum coefficient C_μ and the deflection angle θ_c for W/D = 2, 3 and 4. It can be determined from this figure that there is no obvious difference in the deflection angle of the main jet under the conditions of different ratio of jet width to cylinder diameter W/D. Therefore, it can be concluded that under the condition of ratio of jet width to cylinder diameter W/D using in this chapter, the deflection

characteristics of main jet are depend by the momentum coefficient C_μ and are independent of the ratio of jet width to cylinder diameter W/D.

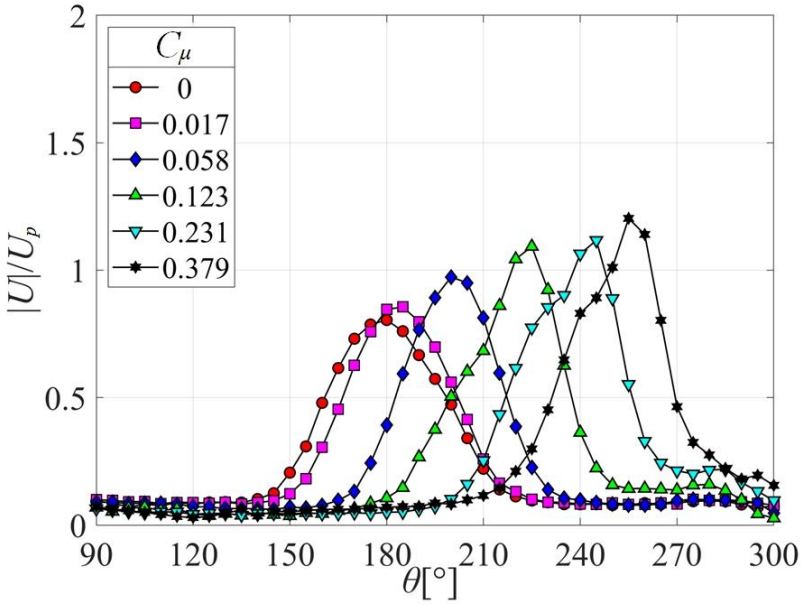

(a) $D/W = 0.5$

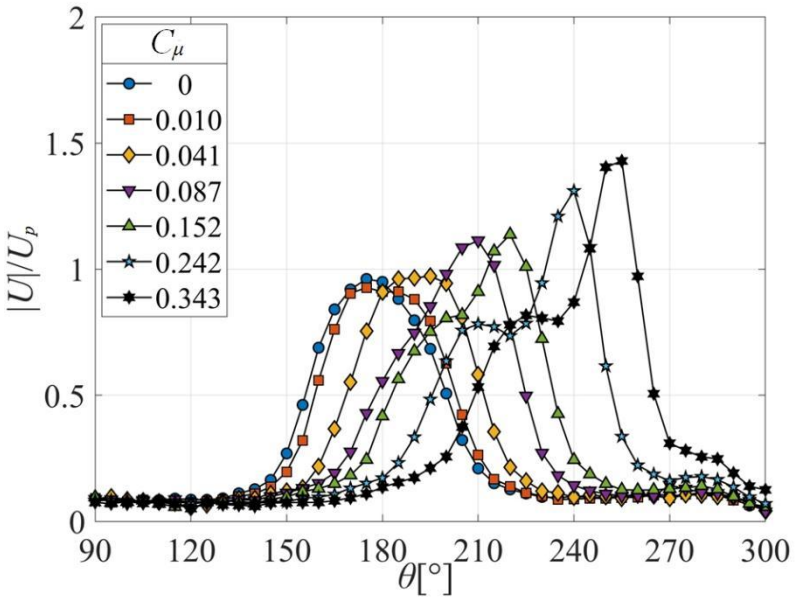

(b) $D/W = 0.33$

Fig. 4-16. Dimensionless velocity distribution of circular cylinder for D/W = 0.5, 0.33, θ_j = 90°, ε = 0.

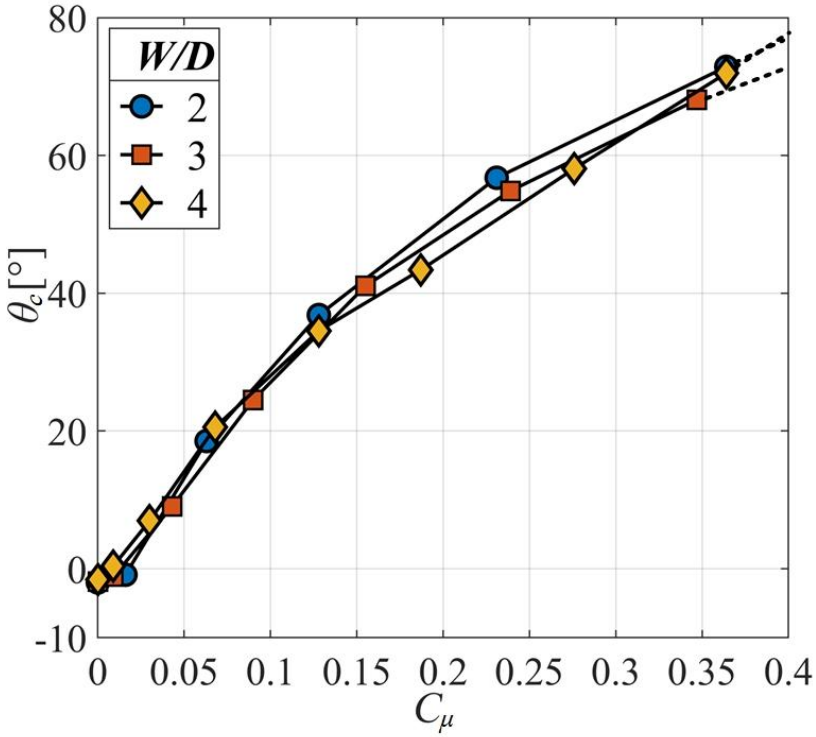

Fig. 4-17 Relation between momentum coefficient and deflection angle for various dimensionless primary jet widths for $\theta_j = 90^\circ$, $\varepsilon = 0$.

The next section focus on studying the influence of eccentricity of circular cylinder on flow deflection characteristics. For this purpose, three different eccentricities of cylinder include ε of -1.3, 0 and 1.3 were set as comparison. To avoid interference from other parameters, the jet width and slot angle were fixed at W = 200 mm and θ_j=90° respectively, while the momentum coefficient was fixed at C_μ = 0.364. Figure 4-18 presents the dimensionless velocity distributions and pressure distributions for ε=-1.3 (refer to Figure 4-18(a)), 0 (refer to Figure 4-5(c)) and 1.3 (refer to Figure 4-18(b)), respectively. And Figure4-19(a) and (b) show the flow visualization observations of ε=-1.3 and 1.3. The dimensionless velocity distribution in Figure 4-18(a) shows that as the eccentricity of cylinder ε decreases, the maximum velocity of jet and the angle of the maximum velocity both increases slightly. And from the pressure distribution in Figure 4-18(b), although the momentum coefficients are the same, it can be found that the pressure distribution of ε = -1.3 has a greater drop in pressure behind the slot of cylinder than ε = 1.3. This is because the amount of fluid that can be able to entrained above the slot of cylinder is different while the eccentricities is different. On the other hand,there is no significant difference in the location of the separation point with different eccentricity ratios.

Next, based on the observation of Figure4.19(a), it can be found that the centre of the cylinder is facing the lower baffle of the nozzle. Due to the low pressure generated at the slot of cylinder, the primary jet is entrained to the cylinder surface resulting in a Coanda effect. Then a significant deflection of the primary jet happened. And because of the high momentum coefficient , no vortice is generated at the trailing edge of the cylinder. From the visualization result in Figure4.19(b), the center of the cylinder is facing the upper baffle of the nozzle,and only a small part of the upper primary jet ejected from the nozzle collides with the leading edge of the cylinder, then this part of the fluid is carried along the cylinder surface by the jet sheet ejected from the cylinder slot, and finally collides with the primary jet below the cylinder which might caused the velocity decreased as shown in Figure4-18(a).

Figure 4-20 depicts the relationship between the eccentricity rate ε and the lift coefficient C_L. Figure 4-21 shows the relationship between the eccentricity rate ε and the deflection angle θ_c. It can be seen that the value of lift coefficient and deflection angle between ε = -1.3 and 0

are similar, and the value of lift coefficient and deflection angles of ε = 1.3 is significantly smaller than ε =-1.3 and 0. Comparing ε = -1.3 and ε = 0, it can be seen that the deflection angle at ε = -1.3 is approximately 8˚ greater than that of ε = 0.

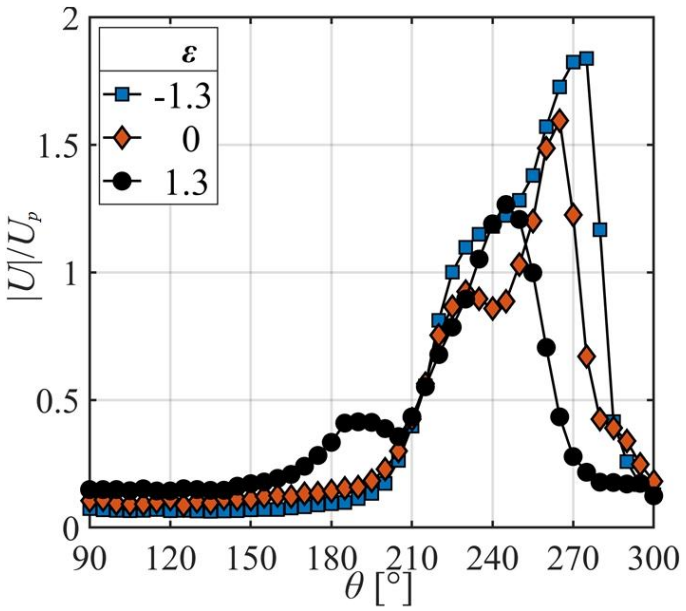

(a) Dimensionless velocity distribution

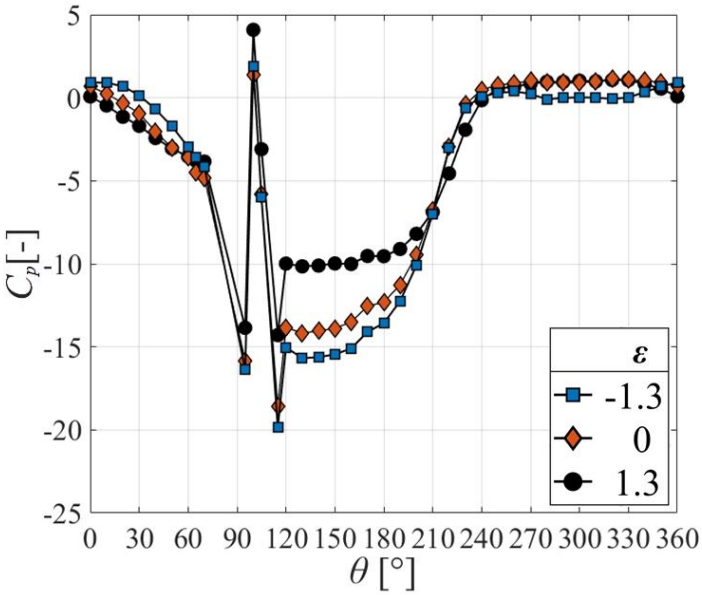

(b) Pressure distribution

Fig. 4-18. Dimensionless velocity distribution and pressure distribution of circular cylinder for ε = 0, ±1.3 and C_μ = 0.364.

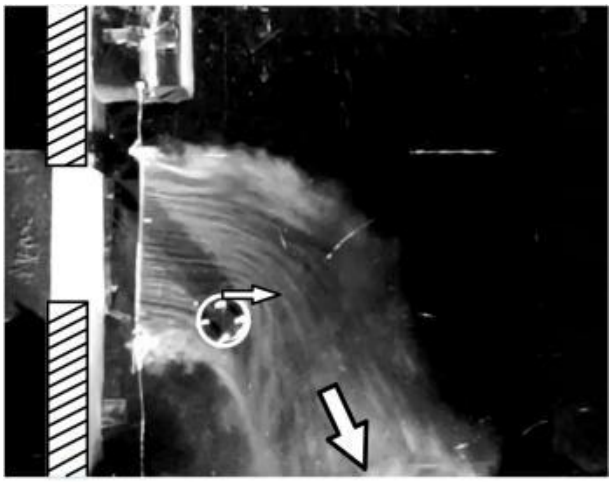

(a) $\varepsilon = -1.3$

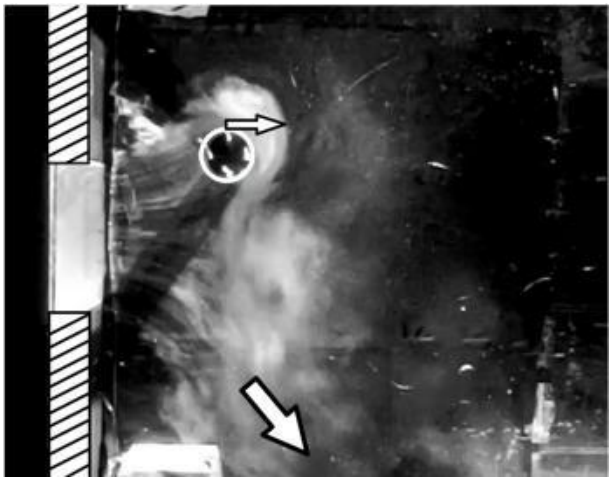

(c) $\varepsilon = 1.3$

Fig. 4-19 Flow visualization obtained using smoke-wire method for $C_\mu = 0.364$.

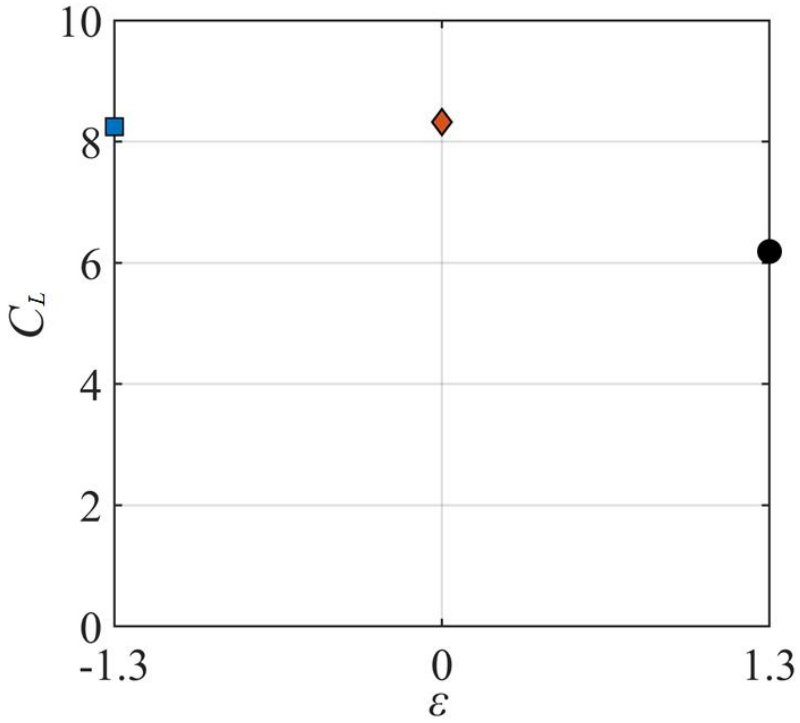

Fig. 4-20 Relation between eccentricity rate ε and lift coefficient C_L for $C_\mu = 0.364$, $D/W = 0.25$.

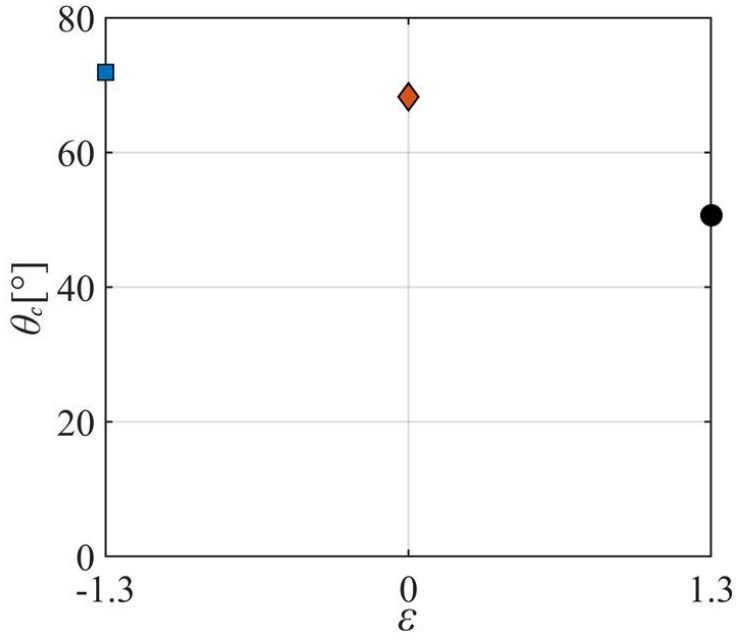

Fig. 4-21 Relation between eccentricity rate ε and deflection angle θ_c for $C_\mu = 0.364$, $D/W = 0.25$.

4.5 Summary

In this chapter, in order to control the direction of two-dimensional jet, we installed a tangential blowing cylinder at the downstream of the main jet, and studied the flow characteristics around the circular cylinder by conducting experiments under various parameters including the momentum ratio between primary jet and jet sheet, slot angles , jet widths(nozzle widths) and the eccentricity of the circular cylinder relative to the position of nozzle. The specific conclusions are as follows:

1) The flow direction of the primary jet depends on momentum coefficient C_μ The deflection angle θ_c can be controlled from 0 to approximately 90° in the parameter range considered in this study.

2) At slot angle $\theta_j = 90$, the curves of lift coefficient, separation point, and deflection angle according to the momentum coefficient are consistent. To smoothly control the deflection angle, it is necessary to precisely control the position of the separation point.

3) The slot angle evaluation shows that the deflection characteristics depend not only on coefficient C_μ but also on slot angle θ_j. For stepless control, it seems appropriate to set a blowing slot at the separation point for $C_\mu = 0$, that is, around $\theta = 90°$.

4) The deflection characteristics of the primary jet can be summarized by C_μ, which is a function of the nozzle width W of the primary jet.

5) The effect of the eccentricity rate ε on the deflection characteristics is mostly negligible, but a larger deflection can be expected for $\varepsilon = -1.3$ at a given C_μ.

6) As a cylinder with tangential blowing in a uniform flow, the cylinder downstream of the primary jet can suppress Karman vortices by adjusting the momentum of the jet sheet.

-Chapter 5-

Comparison between two jet direction control methods

In this study, two jet direction control methods are proposed for application in two different scenarios. For instance, the first method, which is shown in Chapters 2 and 3, adjusts the direction of the continuous primary jet by using a secondary flow with a Coanda surface. The second method aims to control the direction of the existing jet by setting a tangential blowing cylinder downstream of the primary jet. Based on the experiments presented in the preceding chapters, it is clear that both methods have a good control effect on the deflection angle of the jet in their respective application scenarios. In addition, the two method can complement each other in terms of deflection ability. Figure 5-1 shows the relation between momentum coefficient ξ and deflection angle θ_c for different ratios of the velocity of continuous flow and the amplitude of velocity oscillation ζ. The horizontal axis is the momentum ratio $\xi(C_\mu)$ and the vertical axis is the deflection angle θ_c and the parameter is the ζ. For the first method, the ratio of cylindrical radius to jet width R/h_1=1.5, the frequency of the excited flow f=80Hz. And for the second method, R/W=0.25, θ_j=90°, ε =0. For the first method, different angular changing curves can be obtained by varying the ζ. And as the momentum coefficient ξ increases, the first method of using a secondary flow with a Coanda surface below the jet is response faster compared to the second method of placing a tangential blowing cylinder in the downstream of the jet. However, it is also obvious that the deflection ability is inadequate for the condition of positive steady velocity ($\zeta > 0$). For the secondary method, although experiments were only conducted with $\zeta = \infty$, a great deflection angle can be achieve when the steady velocity is positive.

Figure 5-2 illustrates the relation between momentum coefficient ξ and deflection angle θ_c for the two control methods under various ratio of cylindrical radius to jet width $R/h_1(R/W)$. The secondary flow is a continuous suction flow ($\zeta = -\infty$) for the first control method in Figure 5-2(b) , and the secondary flow is a synthetic jet ($\zeta = 0$) with the frequency of 80Hz in Figure 5-2 (c). Both of the conditions show a good deflection ability in the experiments of Chapter 2 and 3. The slot angle θ_j for the second control method used in Figure 5-2(b),(c) is fixed at 90° and the eccentricity rate is fixed at $\varepsilon = 0$. The horizontal axis is the momentum ratio $\xi(C_\mu)$ and the vertical axis is the deflection angle θ_c and the parameter is the R/h_1. It can be seen in Figure 5-2(a) that the jet can not be deflected by by changing R/h_1 when the steady

velocity is above 0 for the first method. By Observing Figure 5-2(b) and Figure 5-2(c), it can be seen that the deflection angle of using the first method can be influenced by R/h_1 in addition to the ratio of the velocity of continuous flow and the amplitude of velocity oscillation ζ and the momentum ratio ξ. And the smaller the R/h_1 the weaker the deflection capability. For example,when the R/h_1 is 0.75 or 0.375 in the first control method, the maximum deflection angle of the fluid can only be around 20°. On the other hand, for the second method, although it has a small R/h_1 of 0.125, the deflection angle can be bigger than 55° by adjusting the momentum coefficient C_μ. It compensates for the lack of deflection angle of the jet in scenarios for the first method with a smaller ratio of R/h_1.

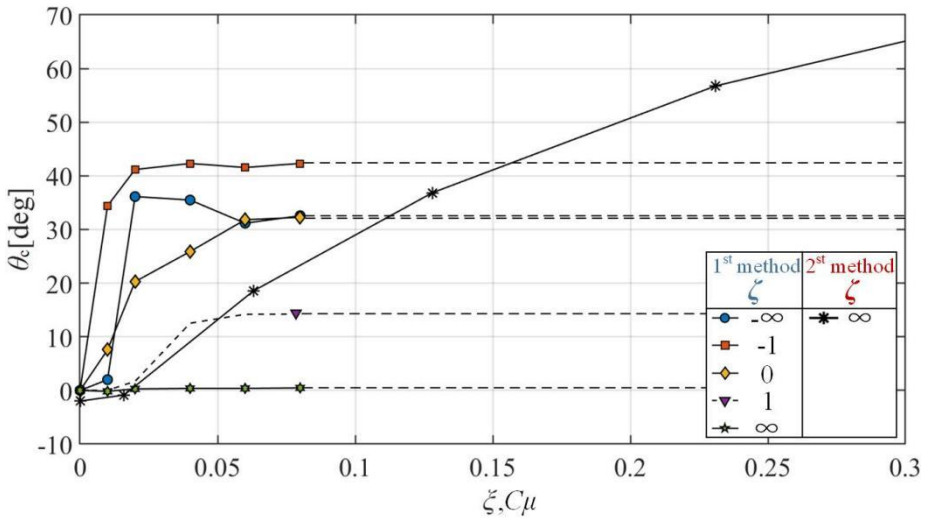

Fig. 5-1. Comparison of deflection angle between two methods for different ratios of the velocity of continuous flow and the amplitude of velocity oscillation ζ. The frequency for exited flow f and the R/h_1 in the first method is 80Hz and 1.5, respectively. The condition for the second method is $R/W = 0.25$, $\theta_j = 90^\circ$,$\varepsilon = 0$.

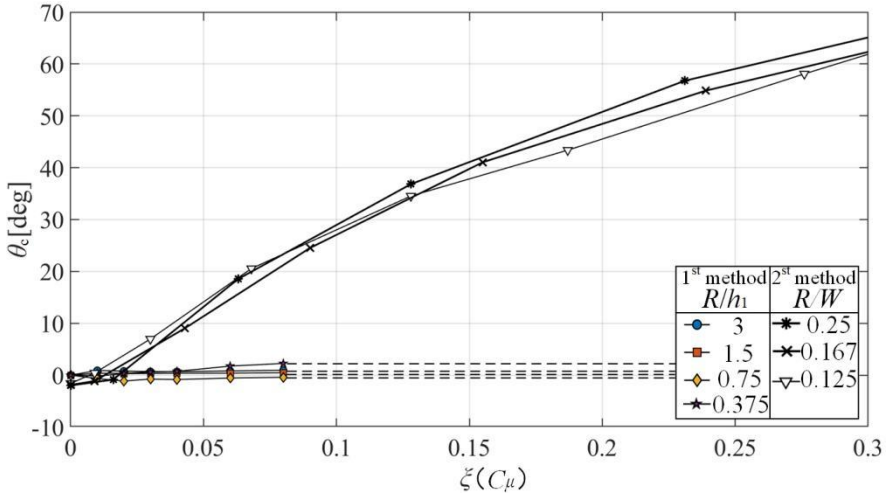

(a) Using secondary suction flow for the first method while the $\zeta = \infty$

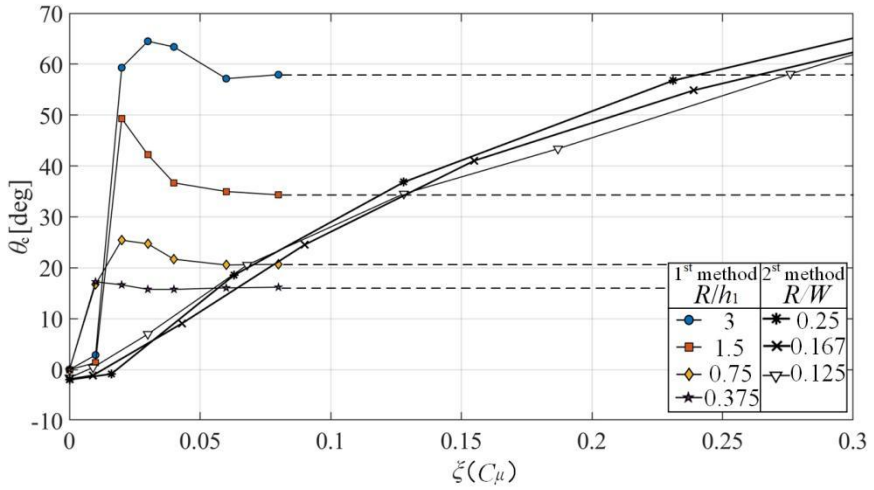

(b) Using secondary suction flow for the first method while the $\zeta = -\infty$

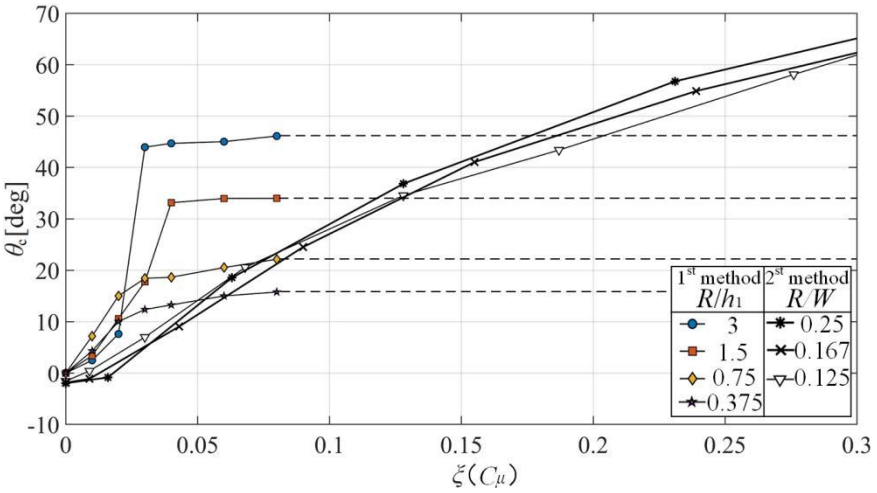

(c) Using secondary synthetic jet for the first method while the f=80Hz, ζ=0

Fig. 5-2. Comparison of deflection angle between two methods under different R/h_1 (R/W).

The condition for the second method is ζ =∞, W/D = 4, θ_j = 90˚.

-Chapter 6-

Conclusion

Based on the concept of eliminating moving parts, this study proposes two control methods suitable for different scenarios. The first method utilizes the secondary flow near the Coanda surface to control the direction of a steady primary jet with high momentum. The second method employs a cylinder with tangential blowing (CCW) to manipulate the direction of an existing jet. The experimental results reveal the deflection characteristics, flow patterns, and unsteady characteristics of the jet, leading to a comprehensive discussion. The conclusions of this thesis are presented as follows:

Chapter 2 introduces a new method of controlling the direction of the primary jet without altering the geometry. This method involves applying the excitation flow as a secondary flow near the surface of the Coanda surface. In addition to momentum ratio ξ, dimensionless frequency f^*, the ratio of steady velocity to velocity fluctuation amplitude ζ is set as a new control parameter to study the influence of different combinations of parameters on flow deflection characteristics. The data obtained from the experiments, which encompass flow visualization, velocity distribution, and computational fluid dynamics (CFD), are employed to analyze the effects of various parameters on the flow deflection characteristics. The following conclusion can be drawn:

1) The deflection angle of the jet was found to depend not only on the momentum ratio ξ and the dimensionless frequency f^*, but also on the ratio of the time-averaged velocity of the continuous flow to the time-varying velocity amplitude ζ.

2) By introducing a new parameter called ζ in addition to ξ and f^*, we succeeded in increasing the number of combinations of setting conditions for the realization of a controllable jet deflection angle. For example, it was found that even under constant conditions of ξ and f^*, a controllable deflection angle can be realized in the range of 0 to 40° by simply adjusting ζ. Furthermore, by introducing ζ, we were able to realize a larger jet deflection angle that could not be obtained by adjusting ξ and f^*.

3) It was suggested that this method can control not only the jet direction but also the jet half width and unsteady characteristics by combining the three parameters ξ, f^*, and ζ.

4) When the oscillating flow is applied to the secondary flow, a large-scale vortex similar to the reverse Karman vortex street is regularly emitted under oscillating secondary jet

conditions.

5) RMS^*_{max} of the oscillating secondary flow is larger than that of the steady secondary flow; especially, as the dimensionless frequency decreases, the value of RMS^*_{max} slightly increases.

In Chapter 3, the investigation focuses on the impact of a dimensionless shape parameter, R/h_1, which represent the ratio of cylinder radius and the width of primary slot, on the deflection characteristics. In addition, the fluid parameter that include the dimensionless frequency of the synthetic jet f^*, the frequency f and the momentum ratio of primary flow to secondary flow ξ were utilized for analysis and comparison. Moreover, the study explores the effect of dimensionless frequency and frequency of the synthetic jets on the unsteady characteristics of the primary flow by velocity distribution and spectrum of fluctuations. The conclusions drawn from the study are as follows:

1)Besides the momentum ratio between primary jet and secondary flow ξ, and the dimensionless frequency f^*, the deflection angle of jet also depends on the ratio of cylinder radius to the width of the primary slot R/h_1.

2) For the secondary synthetic jet, choosing a suitable R/h_1 is able to ensure a good deflection capability while achieving fine adjust of the deflection angle. A large R/h_1 can hardly control the deflection angle by adjusting the momentum ratio ξ, while a small R/h_1 has a poor deflection capability. And for secondary suction flow, a larger R/h_1 means a larger deflection angle.

3) Although the deflection angle is different for different R/h_1 under the condition of the same dimensionless frequency f^*, the structure of the jet is similar.

4) The synthetic jet frequency has a effect on the flow pattern of the jet including the distance interval of the inverse Karman vortice pair and the size of the vortice pair.

5) The half width of the jet and the value of maximum velocity depend on the frequency of the secondary synthetic jet f. The lower the frequency f, the faster the velocity attenuation and the wider the half width.

Chapter 4 uses a cylinder with tangential blow(CCW) to attempt to control the direction of an existing jet by adjusting the momentum of jet sheet from the cylinder slot. A tangential blowing cylinder was installed downstream of the main jet in order to control the direction of the two-dimensional jet. Experiments were conducted under various parameters, including the momentum ratio between the primary jet and jet sheet, slot angles, jet widths (nozzle widths), and the eccentricity of the circular cylinder relative to the position of the nozzle. The specific conclusions are as follows:

1) The flow direction of the primary jet depends on momentum coefficient C_μ. The deflection angle $\Delta\theta_c$ can be controlled from 0 to approximately 90° in the parameter range considered in this study.

2) At slot angle $\theta_j = 90$, the curves of lift coefficient, separation point, and deflection angle according to the momentum coefficient are consistent. To smoothly control the deflection angle, it is necessary to precisely control the position of the separation point.

3) The slot angle evaluation shows that the deflection characteristics depend not only on coefficient C_μ but also on slot angle θ_j. For stepless control, it seems appropriate to set a blowing slot at the separation point for $C_\mu = 0$, that is, around $\theta = 90°$.

4) The deflection characteristics of the primary jet can be summarized by C_μ, which is a function of the nozzle width W of the primary jet.

5) The effect of the eccentricity rate ε on the deflection characteristics is mostly negligible, but a larger deflection can be expected for $\varepsilon = -1.3$ at a given C_μ.

6) As a cylinder with tangential blowing in a uniform flow, the cylinder downstream of the primary jet can suppress Karman vortices by adjusting the momentum of the jet sheet.

In Chapter 5, a detailed comparison is provided regarding the deflection characteristics and applicable scenarios of the two jet control methods.

In conclusion, the two jet direction control methods proposed in this paper both possess decent deflection capability. However, their applicable scenarios, deflection characteristics, and unsteady characteristics are not identical. Moreover, for specific cases, the two control

methods can be interchangeably utilized to achieve complementary deflection characteristics in different scenarios.The first method studied in Chapter 2 and 3 demonstrates a rapid response to changes in momentum ratio ξ, allowing for a large deflection angle to be achieved even at lower momentum ratios. Furthermore, it can adjust the deflection angle by combining three parameters, including momentum ratio ξ, dimensionless frequency f^*, and the ratio of steady velocity to velocity fluctuation amplitude ζ, while considering the unsteady characteristics of the jet. However, due to its reliance on exciting the secondary flow to control the primary flow, it still faces challenges when applied in high Reynolds number scenarios. Additionally, there are limitations to adjusting the deflection angle using momentum ratio ξ, as it becomes difficult to increase the deflection angle once the saturation region is reached. As for the second method, it can compensate for the deficiency in deflection angle caused by the use of a secondary injection jet in the first method. Although it can only control the deflection angle through the fluid parameter of the momentum ratio ξ, and its response speed is relatively slow, it is difficult to reach the saturation region, and can achieve a larger deflection angle than the first method by increasing the momentum ratio ξ. Moreover, it is also suitable for high Reynolds number scenarios.

Acknowledgement

I am deeply grateful to have this opportunity to express my sincerest thanks to all the people who have supported me throughout my journey of completing this thesis.

Firstly, I would like to extend my heartfelt gratitude to my supervisor, Prof. Kotaro Sato, who has been a constant source of encouragement and guidance. His expertise, patience, and unwavering support have been instrumental in the successful completion of this thesis.

I would also like to thank Dr Koichi Nishibe from Tokyo City University, for his valuable insights and support throughout the paper and research. His enthusiastic guidance was a great help to me, and I am grateful for his expertise in the field

I am also grateful to Dr Donghyuk Kang from Saitama University, for his constructive advise, and support for the paper and research. His guidance has been invaluable and gave me a lot of inspiration.

I would like to thank Dr Wakana Tsuru, for her advise for experiment and help in paper writing and reviewing.

I acknowledge the associate reviewers of the thesis, Prof. Shinichiro Ito, Prof. Shigehiro Hashimoto, Prof. Suzuki Kenji and Prof. Kazuhiko Yokota for their advice and unique perspectives on my research and thesis, which further improved my thesis.

Additionally, I benefited from the help of Yu Tamanoi, Fumiya Takahashi, Hiroki Tezuka and Kaito Suzuki in experiment of this research, for which i am grateful.

I would like to express my gratitude to my friends and family for their unwavering support and encouragement during the challenging times. Their love and support have been my source of inspiration and motivation to keep going.

Finally, I would like to acknowledge the contribution of all the participants in this study for their time and effort in providing the valuable data that has made this research possible.

I hope that this thesis will make a valuable contribution to the field, and I am grateful to all who have supported me in this endeavor.

Reference

[1] Royce R. The jet engine[M]. John Wiley & Sons, 2015.

[2] Callender B, Gutmark E, Martens S. Far-field acoustic investigation into chevron nozzle mechanisms and trends[J]. AIAA journal, 2005, 43(1), pp. 87-95.

[3] Snow, B. H.: Thrust vectoring control concepts and issues, *SAE Transactions*, (1990), pp. 1488-1499.

[4] Kowal, H J.: Advances in Thrust Vectoring and the Application of Flow-Control Technology, *Canadian Aeronautics & Space Journal*, 48(2) (2002), pp. 145-151.

[5] Xiao Zhongyun, Jiang Xiong. Advances in fluidic thrust vectoring technique research, Journal of Experiments in Fluid Mechanics, 31(4), pp. 8-15.

[6] Wing D J. Static investigation of two fluidic, thrust-vectoring concepts on a two-dimensional convergent-divergent nozzle[R]. NASA Technical Memorandum 4574, 1995.

[7] Wing D J, Giuliano V J. Fluidic Thrust Vectoring of an Axisymmetric Exhaust Nozzle at Static Conditions[R]. AIAA-1997-3149, 1997.

[8] Deere K. Computational investigation of the aerodynamic effects on fluidic thrust vectoring[C].36th AIAA/ASME/SAE/ASEE Joint Propulsion Conference and Exhibit. 2000-3598.

[9] Trancossi, M., Dumas, A. A.C.H.E.O.N.: Aerial coanda high efficiency orienting-jet nozzle. SAE Technical Papers, 2011-01-2737, 2011.

[10] Deere K, Berrier B, Flamm J, et al. Computational study of fluidic thrust vectoring using separation control in a nozzle[C]. 21st AIAA applied aerodynamics conference. 2003-3803.

[11] Mason, M. S., Crowther, W. J. Fluidic thrust vectoring of low observable aircraft, *CEAS Aerospace Aerodynamic Research Conference*, (2002) pp. 1-7.

[12] Al-Asady A A A, Abdullah A M. Fluidics thrust vectoring using co-flow method[J]. Al-Nahrain Journal for Engineering Sciences, 2017, 20(1): pp. 5-18.

[13] Bettridge M W, Smith B L, Spall R E. Aerodynamic jet steering using steady blowing and suction[J]. Experiments in fluids, 2006, 40(5), pp. 776-785.

[14] Dores D, Madruga Santos M, Krothapalli A, et al. Characterization of a counterflow thrust vectoring scheme on a gas turbine engine exhaust jet[C]. 3rd AIAA Flow Control Conference. 2006-3516.

[15] Song M J, Park S H, Lee Y. Application of backstep Coanda flap for supersonic coflowing fluidic thrust-vector control[J]. AIAA Journal, 2014, 52(10): 2355-2359.

[16] Strykowski P J, Krothapalli A, Forliti D J. Counterflow thrust vectoring of supersonic jets[J]. AIAA journal, 1996, 34(11): 2306-2314.

[17] Smith B L, Glezer A. The formation and evolution of synthetic jets[J]. Physics of fluids, 1998, 10(9): 2281-2297.

[18] Smith B L, Glezer A. Jet vectoring using synthetic jets[J]. Journal of Fluid Mechanics, 2002, 458: 1-34.

[19] Smith B L, Swift G W. A comparison between synthetic jets and continuous jets[J]. Experiments in fluids, 2003, 34(4): 467-472.

[20] Nishibe K, Fujita Y, Sato K, et al. Experimental and numerical study on the flow characteristics of synthetic jets[J]. Journal of Fluid Science and Technology, 2011, 6(4): 425-436.

[21] Guo D, Cary A W, Agarwal R K. Numerical simulation of vectoring of a primary jet with a synthetic jet[J]. Aiaa Journal, 2003, 41(12): 2364-2370.

[22] Koso, T. and Morita, M., 2014, Effects of stroke and Reynolds number on characteristics of circular synthetic jets. Journal of Fluid Science and Technology, 9(2), pp. 1-15.

[23] Zhang, P. F. and Wang, J. J., 2007, Novel signal pattern for efficient synthetic jet generation. AIAA Journal, 45(5), pp. 1058-1065.

[24] Kobayashi, R., Watanabe, Y., Tamanoi, Y., Nishibe, K., Kang, D., and Sato, K.: Jet vectoring using secondary Coanda synthetic jets, Mech. Eng. J. **7**(5) (2020), pp. 20-00215.

[25] Veer, M., and Strykowski, P. J.: Counterflow Thrust Vector Control of Subsonic Jets: Continuous and Bistable Regimes, J. Propuls Power, **13** (1997) pp. 412-420.

[26] De la Montanya, J. B. and Marshall, D.: Circulation Control and its Application to Extreme Short Take-off and Landing Vehicles, 45th AIAA Aerospace Sciences Meeting and Exhibit, 2007.

[27] Waka, R., Yoshino, F., Hayashi, T., and Iwasa, T.: The Aerodynamic Characteristics at the Mid-Span of a Circular Cylinder with Tangential Blowing, Bull. JSME, 26 (1983), pp. 755–762.

[28] Okayasu, S., Sato, K., Shakouchi, T., and Furuya, O.: Flow Around a Circular Cylinder with Tangential Blowing near a Plane Boundary (1st Report, A Study on Fluid Force), Trans. Jpn. Soc. Mech. Eng. B, 73 (2007), pp. 1790-1797.

[29] Okayasu, S., Sato, K., Shakouchi, T., and Furuya, O.: Flow Around a Circular Cylinder with Tangential Blowing near a Plane Boundary (2nd Report, A Study on Unsteady Characteristics), Trans. Jpn. Soc. Mech. Eng. B, 74 (2008), pp. 1725－1734.

[30] Okayasu, S., Arakawa, Y., Sato, K., Shakouchi, T., and Furuya, O.: Influence of Ground and Ceiling Effect on High-Lift Device Using a Circular Cylinder with Tangential Blowing, J. Jpn. Soc. Aeronaut. Space Sci., 56 (2008), pp. 425-432.

[31] Sato M, Matsuoka K, On Separation Control of Flow along Curved Wall: Controlling Characteristics and Comparison of Effects in Various Control Methods, Transactions of the Japan Society of Mechanical Engineers, Vol.36, No.289 (1970), pp.1493-1502.

[32] Ueda, S. and Tanaka, H. , Boundary Layer and Flow Control by Slot-Blowing Applied to a Flow Around a Circular Cylinder : 1st Report, An Experimental Study of Lift, Drag and Wake Control, Transactions of the Japan Society of Mechanical Engineers, Vol.41, No.350 (1975), pp.2853-2865.

[33] Ueda S, and Tanaka H, Boundary Layer and Flow Control by Slot-Blowing Applied to a Flow Around a Circular Cylinder : 3rd Report, Transactions of the Japan Society of Mechanical Engineers, Vol.43, No.366 (1977), pp.570-581.

[34] Yoshida, Y., Sato, K. and Ono, Y. , Wake Oscillation of Column Wall Jet in Uniform Flow, Journal of the Japan Society for Aeronautical and Space Sciences, Vol.54, No.630 (2006), pp.288-294

[35] Panitz, T., Wasan, D. T. Flow attachment to solid surfaces: the Coanda effect, *AIChE Journal*, **18**(1) (1972), pp. 51-57.

[36] Holman, R., and Utturkar, Y., 2005, “Formation Criterion for Synthetic Jets,” AIAA J., 43(10), pp. 2110-2116.

[37] Akiyoshi IIDA.Turbulent Flow Measurement with Hot-wire Anemometer, *Journal of jet flow engineering*(2002), pp.24-33.

[38] Thuji, T. and Nagano, Y. Recent advances in hot-wire measurements, Journal of Japan Society of Fluid Mechanics, 18-4 (1999), pp.191-198.

[39] Willson, D. J. and Goldstein, R. J., Turbulent Wall Jets with Cylindrical Streamwise Surface Curvature, Transactions of the ASME Journal of Fluids Engineering, Vol.98 (1976), pp.550-557

[40] Neuendorf, R. and Wygnanski, I., On a Turbulent Wall Jet Flowing over a Circular Cylinder, Journal of Fluid Mechanics, Vol.381 (1999), pp.1-25

[41] Shakouchi, T.: *Jet Flow Engineering: Fundamentals and Application*, Morikita Publishing, 2004.

[42] W.H. Melbourne, Wind tunnel blockage effects and corrections, Proc. Int. Workshop Wind Tunnel Modeling, Gaithersburg, MD, 1982, pp. 197-216.

[43] Courchense, J. and Laneville, A., A Comparison of Correction Methods Used in the Evaluation of Drag Coefficient Measurements for Two Dimensional Rectangular Cylinder, Transactions of the ASME Journal of Fluids Engineering, Vol.101 (1979), pp.506-510.

[44] Ota, T., Okamoto, Y. and Yoshikawa, H., Correction Formula of Wall Effects on Unsteady Separated Flow around Bluff Bodies, Transactions of the Japan Society of Mechanical Engineers, Series B, Vol.60, No.571 (1994), pp.744-749.

[45] Yamada, H., Effects of End Plates on Spanwise Characteristics of Flow around a Circular Cylinder, Transactions of the Japan Society of Mechanical Engineers, Series B, Vol.58, No.552 (1992), pp.2368-2373.

[46] Yoshino, F., Waka, R., Iwasa, T and Hayashi, T., The Effect of a Side-Wall on Wing Characteristics of a Circular Cylinder with Tangential Blowing, Transactions of the Japan Society of Mechanical Engineers , Series B, Vol.46, No.410 (1980), pp.1890-1898.

[47] Waka, R., Yoshino, F., Hayashi, T. and Iwasa, T., The Aerodynamic Characteristics at the Mid-Span of a Circular Cylinder with Tangential Blowing, Transactions of the Japan Society of Mechanical Engineers, Series B, Vol.48, No.433 (1982), pp.1650-1658

[48] Okayasu, S., Sato, K., Shakouchi, T., and Furuya, O.: Flow Around a Circular Cylinder

with Tangential Blowing near a Plane Boundary (1st Report, A Study on Fluid Force), *Trans. Jpn. Soc. Mech. Eng. B*, 73 (2007), pp. 1790-1797.

[49] Okayasu, S., Sato, K., Shakouchi, T., and Furuya, O.: Flow Around a Circular Cylinder with Tangential Blowing near a Plane Boundary (2nd Report, A Study on Unsteady Characteristics), *Trans. Jpn. Soc. Mech. Eng. B*, 74 (2008), pp. 1725–1734.

[50] Furuya, Y. and Yoshino, F. , Aerodynamic Force Acting on a Circular Cylinder with Tangential Injection of Air , Transactions of the Japan Society of Mechanical Engineers, Vol.41, No.341 (1975), pp.170-180.

[51] Okamoto, Tetsushi, and Miki Yagita.: The experimental investigation on the flow past a circular cylinder of finite length placed normal to the plane surface in a uniform stream, Bulletin of JSME 16.95 (1973), pp.805–814.

[52] Ohkura, N., Hayafuji, H. and Okude, M., Pressure Distribution around a Rotating Cylinder near the Critical Reynolds Number, Transactions of the Japan Society of for Aeronautical and Space sciences, Vol.45 No.526 (1997), pp.669-678.

[53] Ueda, S. and Tanaka, H. , Boundary Layer and Flow Control by Slot-Blowing Applied to a Flow Around a Circular Cylinder : 1st Report, An Experimental Study of Lift, Drag and Wake Control, Transactions of the Japan Society of Mechanical Engineers, Vol.41, No.350 (1975), pp.2853-2865.